CFD modelling of breakwaters embedding wave energy converters

Original Citation:
CFD modelling of breakwaters embedding wave energy converters / Scarpetta, Filippo. - ELETTRONICO. - (2018). [10.60576/poliba/iris/scarpetta-filippo_phd2018]

Published version
Politecnico di Bari
DOI:10.60576/poliba/iris/scarpetta-filippo_phd2018

Department of Mechanics, Mathematics and Management
MECHANICAL AND MANAGEMENT ENGINEERING
Ph.D. Program
SSD: ING-IND/08–MACCHINE A FLUIDO

Final Dissertation

CFD modelling of breakwaters embedding wave energy converters

---

by
Filippo Scarpetta

<u>Supervisors:</u>

Prof. S.M. Camporeale

Prof. M. Torresi

Coordinator of Ph.D Program:

Prof. G.P. Demelio

XXX cycle, 2015-2017

Department of Mechanics, Mathematics and Management
MECHANICAL AND MANAGEMENT ENGINEERING
Ph.D. Program
SSD: ING-IND/08–MACCHINE A FLUIDO

Final Dissertation

CFD modelling of breakwaters embedding wave energy converters

by
Filippo Scarpetta :

____
Firma leggibile e per esteso

Referees:

Prof. Ing. Alberto Traverso

Dr. Ing. Domenico Borello

Supervisors:

Prof. S.M. Camporeale

______________ *firma*

Prof. M. Torresi

______________ *firma*

Coordinator of Ph.D Program:
Prof. G.P Demelio
______________ *firma*

XXX cycle, 2015-2017

Table of Contents

Sommario

Negli ultimi anni i crescenti problemi di disponibilità e inquinamento, legati allo sfruttamento delle fonti fossili tradizionali per la produzione energetica, hanno spinto la ricerca sulle fonti rinnovabili. Tra queste, le onde marine sono una fonte ad alto potenziale, ma ancora scarsamente utilizzata. Diverse tecnologie sono state sviluppate per sfruttare l'energia delle onde e i dispositivi Oscillating Water Column (OWC) sono i più accreditati per una diffusione effettiva. Questo lavoro è focalizzato sull'analisi delle prestazioni di particolari dispositivi di tipo OWC, i REWEC (REsonant sea Wave Energy Converter). Sono state considerate due diverse versioni, REWEC1 e REWEC3, che sono integrati rispettivamente in frangiflutti sommersi ed emersi.

L'aspetto più interessante dei REWEC è che è possibile farli operare in condizioni di risonanza in corrispondenza di quello stato di mare che dà il massimo contributo energetico annuale. Il comportamento dinamico dei REWEC può essere approssimato a quello di un sistema massa-molla-smorzatore. Partendo da questa considerazione, è stato derivato un criterio per valutare la frequenza naturale dei REWEC. Un modello CFD è stato sviluppato per verificare il comportamento di risonanza di un dispositivo REWEC1 in scala. L'interazione acqua-aria è stata tenuta in considerazione per mezzo del modello Volume Of Fluid (VOF) implementato nel codice commerciale Ansys Fluent. Entrambi i campi di flusso di aria e acqua sono stati considerati non stazionari. I risultati delle simulazioni hanno mostrato un buon accordo con quelli analitici e sperimentali, in particolare il modello di turbolenza k-ω Standard è stato implementato all'interno del REWEC.

Il modello CFD è stato applicato anche alla simulazione di frangiflutti sommersi convenzionali e REWEC1 immessi in un canale bidimensionale, ottenendo un nuovo metodo per la valutazione del coefficiente di assorbimento del REWEC1. Infatti, quando si considera l'interazione delle onde con frangiflutti sommersi convenzionali, l'energia dell'onda incidente viene suddivisa in: una frazione riflessa; una frazione dissipata, a causa dell'impatto dell'onda e delle perdite di attrito; e una frazione trasmessa alla riva. Se il frangiflutti sommerso incorpora un REWEC1, è possibile ottenere un'ulteriore riduzione dell'energia trasmessa a causa dell'assorbimento del dispositivo, migliorando le prestazioni di protezione della costa. Per le simulazioni è stato preso in considerazione un frangiflutti REWEC1 in scala senza sistema PTO (Power Take-Off). Quindi, i risultati della simulazione hanno mostrato solo una piccola differenza tra i coefficienti di trasmissione dei due frangiflutti, consentendo tuttavia di calcolare il coefficiente di assorbimento del REWEC1 dovuto alle perdite d'attrito dell'acqua all'interno del dispositivo.

Infine, è stato simulato un frangiflutti REWEC3 in scala reale, tenendo conto delle caratteristiche della turbina ad aria adottata come dispositivo PTO. Il frangiflutti replica quello installato nel porto di Civitavecchia (Italia). Un tipico stato di mare è stato riprodotto

per mezzo di onde regolari generate da un generatore di onde a pistone. Come nel caso del REWEC1 scalato, le simulazioni CFD sono state eseguite in un dominio di calcolo bidimensionale (2D), riducendo la quantità di risorse computazionali richieste. Per simulare il flusso oscillatorio attraverso la turbina ad aria, è stato proposto un nuovo metodo. La zona del dominio corrispondente al condotto in cui è incorporata la turbina ad aria è stata modellata come una zona porosa. Sono state implementate equazioni analitiche in grado di modellare lo scambio di massa ed energia attraverso il condotto dell'aria e la turbina. I risultati della simulazione si sono mostrati in buon accordo con quelli registrati durante il funzionamento dell'impianto di Civitavecchia. Un ulteriore risultato del lavoro è stato un approfondimento del comportamento fluidodinamico del flusso d'acqua all'interno del REWEC3, evidenziando i miglioramenti di progettazione necessari per ridurre le perdite.

Abstract

In recent years the raising supply and environmental problems related to traditional fossil fuel exploitation for energy production have pushed the research on renewable sources. Among these, sea waves have a high potential, but still poorly used. Different technologies have been developed in order to harness wave energy, and the Oscillating Water Column (OWC) devices are the most accredited for an actual diffusion. This work is focused on the performance analysis of particular OWC-type devices, namely the REWECs (REsonant sea Wave Energy Converter). Two different versions have been considered, the REWEC1 and the REWEC3; constituting a submerged and an emerged breakwater, respectively.

The most interesting aspect of REWECs is the possibility to operate them under resonant conditions with that sea state which is the one that gives the highest yearly energy contribution. Both REWEC1 and REWEC3 dynamic behavior can be approximated by means of a mass-spring-damper system. According to this approximation, a criterion for evaluating the oscillating natural frequency of the REWECs has been derived. A CFD model has been developed in order to verify the resonance behaviour of a scaled REWEC1 device. The water-air interaction has been taken into account by means of the Volume Of Fluid (VOF) model implemented in the commercial code Ansys Fluent. Both air and water flow fields have been assumed to be unsteady. The CFD model has been validated against both analytical and experimental results. Simulation results showed a good agreement with both measurements and predictions, particularly when the Standard k-ω turbulence model is implemented inside the REWEC.

The CFD model has been applied also to the simulation of both conventional and REWEC1 submerged breakwater placed into a two-dimensional wave flume, obtaining a novel method for the valuation of the REWEC1 absorption coefficient. In fact, when considering the interaction of waves with a conventional submerged breakwater, the incident wave energy is shared into: a reflected fraction; a dissipated fraction, due to the wave breaking and the friction losses on it; and a transmitted fraction to the shore. If the submerged breakwater embeds a REWEC1, a further reduction of the transmitted energy can be achieved due to device absorption, improving the coast protection performance of the structure. Actually, a scaled REWEC1 breakwater without PTO-system (Power Take-Off) has been considered. Then, the simulation results showed only a small difference between the transmission coefficients of the two breakwaters, allowing however to calculate the absorption coefficient of the REWEC1 due to the water losses inside the device.

Finally, a full-scale REWEC3 breakwater has been simulated by means of CFD, taking into account the characteristics of the air turbine adopted as power take-off device. The breakwater replicated the one installed in the Civitavecchia harbour (Italy). A typical sea state has been reproduced by means of regular waves generated by a piston-type wave-

maker. As in the case of the scaled REWEC1, CFD unsteady simulation have been carried out in a two dimensional (2D) reference frame, reducing the huge need of computational resources. In order to simulate the oscillating flow across the air turbine, a new method has been also proposed here. The zone of the domain corresponding to the duct where the air turbine is embedded has been modelled as a porous zone. Analytical equations able to model the exchange of mass and energy across the air duct and the turbine have been implemented. The simulation results are in good agreement with the ones registered during the operation of the Civitavecchia plant. A further outcome of the work has been a deep insight into the fluid-dynamic behaviour of the water flow inside the REWEC3, highlighting the design improvements needed to reduce friction losses.

1. Introduction

1.1 Overview, motivations and objectives of the thesis

In recent years, research in the field of renewable energy sources for energy production has undergone a considerable boost, favoured by the supply and environmental pollution problems of traditional fossil sources. Together with the most widely exploited renewable sources, ocean energy is also a source with very high potential but still poorly exploited. In particular, the wave source is abundant and widespread all over the world. Although in the last 50 years many prototypes and patents have been proposed for wave energy conversion, problems of costs and resistance of structures in the marine environment have limited the development of large-scale projects. Among the various types of developed Wave Energy Converters (WECs), the Oscillating Water Column devices (OWC) have led to promising results, evidenced by the operation of full-scale plants.

The present thesis work is based on the CFD analysis of the performance of particular OWC devices, the REWECs (Resonant Wave Energy Convertes). A REWEC plant essentially consists of a series of modularly built caissons. The caissons can be submerged, as in the case of REWEC1 or emerged, as in the case of REWEC3. In the first case, the Power Take-Off (PTO) system will be a self-rectifying water turbine, whilst in the second case it will be an air turbine. One of the main features of the REWEC plants is the fact that they can be designed to operate in resonance conditions with a sea state. For example, one can think of designing the plant in such a way as to ensure a resonant operation with the sea state that leads to the greatest amount of energy produced during the year. The natural frequency of a REWEC device can be derived analytically from the analogy with a mass-spring-damper system.

Computational fluid dynamics (CFD) is a very useful tool, widely used to verify the energy performance of plants and to analyse in detail the flow dynamics within energy systems. The development of CFD simulations allows to replace the execution of experimental tests, leading to a reduction of costs and design time. The aim of this thesis work was to develop a CFD model for the simulation of the dynamic behaviour of both REWEC1 and REWEC3 plants. The CFD model has been validated by comparison with the results of experimental tests previously carried out at Dipartimento di Ingegneria Civile ed Ambientale (DICEAM) of the University of Reggio Calabria by Professor Fabio Filianoti.

The experimental apparatus was a scaled REWEC1 device, subject to free damping oscillations in order to measure its natural frequency. Based on a two-dimensional schematization of the experimental system, several CFD simulations have been conducted by varying the starting conditions of the free damped oscillations. The results of the simulations were in good agreement with the analytical and experimental ones, validating the CFD model. In particular, optimal results have been achieved when turbulence has been reproduced with the Standard k-ω model.

Subsequently, the CFD model has been applied to the simulation of a submerged REWEC1 breakwater under waves developed in a two-dimensional channel. The two-dimensional channel reproduced the one present at Laboratorio di Ingegneria delle Coste (LIC) of the Polytechnic University of Bari, for the purpose of a future installation of an experimental model. As an initial work, the CFD simulation involved a PTO-free device. However, an original calculation of the fraction of the incident wave energy absorbed by the plant has been developed. The absorption was mainly due to the water flow losses inside the REWEC1. The procedure is based on the method proposed by Goda & Kittitanasuan, starting from the analysis of the positions of the free surface inside the channel recorded during the simulation.

The transmission coefficient of the REWEC1 barrier, i.e. the fraction of incident energy transmitted to the shore, has also been calculated. In order to verify the effectiveness of a REWEC system as a means of shore protection, the simulation of a breakwater having the same dimensions but impermeable has been also carried out. The comparison showed only a slight reduction in the transmission coefficient in the case of REWEC1, in fact no PTO device was considered and therefore the absorption capacity of the plant was reduced. As another result of the simulations, a deep insight of the fluid-dynamics inside the system highlighted the sections that require design improvements in order to facilitate the flow of water into the system.

Finally, the potential of the CFD model has been analyzed in the simulation of a full-scale REWEC3 breakwater, in this case equipped with a PTO-system. The REWEC3 plant installed in the port of Civitavecchia (Italy) was considered. The calculation domain consisted of a 2D section of the full-scale plant located inside a channel where a wave motion is generated. The PTO-system, represented by a Wells turbine in the real plant, has been modelled by setting a porous medium in the area of the computational domain corresponding to the duct that houses the turbine. The simulation results have shown that the 2D model leads to a correct analysis of the energy performance of the plant. In fact, a good agreement has been found between the pressure drop values recorded at the ends of the porous medium and those recorded at the turbine heads during the full-scale plant operation.

Furthermore, it was possible to calculate the value of the power dissipated by the water flow inside the plant, to be reduced if the power available for the conversion of the turbine is to be increased. The analysis of the streamlines recorded during the simulation has highlighted the critical areas of the plant that increase the value of water losses, which can be improved during the design phase.

1.2 Structure of the thesis

The thesis starts with an analysis of the global energetic scenario, characterised by the increase of the use of renewable energy sources over the years to the detriment of traditional fossil sources. In particular, the European regulations that define the objectives of the member states in terms of energy production from renewable sources are highlighted. Subsequently, as an high potential renewable source, ocean energy is described in all the forms in which it can be used for energy production: wave, tidal and thermal energy.

Focusing on wave energy conversion, the main aspects of WECs are treated, showing the methods by which they can be classified. These are mainly two: the installation distance from the coast and the operating principle. According to the operating principle we will have: floating devices, wave surge converters, over-topping devices and pressure difference devices. To the last mentioned category belong Oscillating Water Column (OWC) devices, of which REWECs are an evolution. For each of these categories the state of the art is defined. Since REWEC plants constitute breakwater barriers, a section is dedicated to the experimental and numerical works carried out over the years in the analysis of the performance of breakwaters of different sizes and characteristics. Finally, the REWEC1 and REWEC3 devices are described, obtaining for each one the equations that allow to calculate the natural frequency of the water flow inside the device.

Then, the CFD model used to simulate the REWEC plants behavior is illustrated. First of all, we will focus on the methods for simulating a multiphase flow, such as the one present in a REWEC. Following the types of solver, the main settings, the dynamic mesh model used to generate a wave motion within the computational domain and the setting of a porous medium to simulate the PTO within a REWEC3 are analyzed.

The analysis of the three considered cases follows: the simulation of the REWEC1 scaled device, reproducing an experimental plant in order to validate the CFD model; the simulation of a scaled REWEC1 breakwater placed in a two-dimensional channel; and the simulation of a full-scale REWEC3 breakwater, equipped with PTO system. For all three cases the characteristics of the numerical domains are described and the simulation results are analyzed, highlighting the potentials, limits and possible future developments of the CFD modelling of REWEC devices.

Moreover, suggestions for future works are proposed. In particular, it is reported a preliminary work carried out in collaboration with Professors Maurizio Collu and Taka Nishino at the School of Water, Energy and Environment (SWEE) of the Cranfield University. In the aim of integrate REWEC devices into off-shore turbines floating platforms, a CFD model for the simulation of a floating box under waves has been setted-up. The model has been validated comparing the simulation results with analytical, experimental and numerical results.

Finally, the main achievements of the thesis are summarized as a conclusion.

2. State of the art of renewables and ocean energy

2.1 The global energetic sources scenario and the role of renewables

An analysis of the global primary energy consumption, considering the several sources exploitation, is useful to outline both the importance and the potential of renewable power in the global energetic scenario. Global primary energy consumption increased by 1% in 2016, following growth of 0.9% in 2015 and 1% in 2014 [BP, 2017]. In the past three years growth has been below the 10-year average, equal to 1.8% a year. The trend of the world energy consumption in the past 15 years is reported in Fig. 2.1-1. Considering the most important energy markets, energy consumption in China grew by just 1.3% in 2016, and its growth during 2015 and 2016 was the lowest over a two-year period since 1997-98. Despite this, China remained the world's largest growth market for energy for a 16th consecutive year.

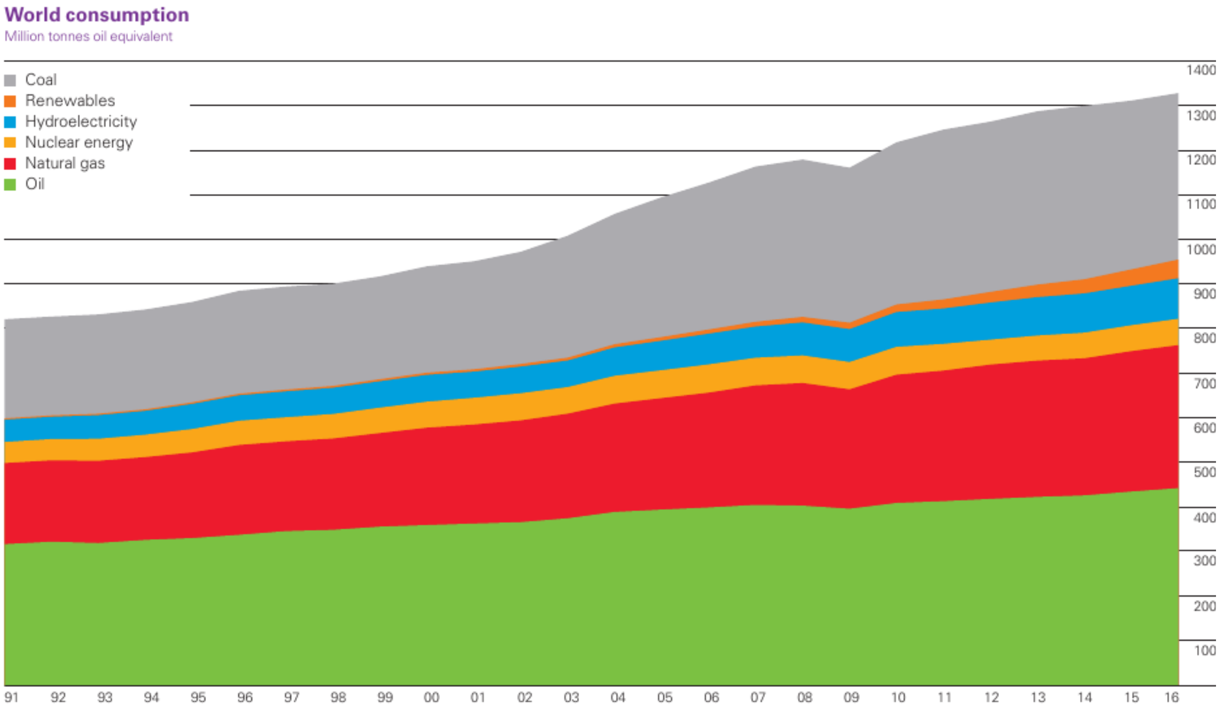

Fig. 2.1-1. Word primary energy consumption: million tonnes oil equivalent, from 1991 to 2016

The energy sources can be classified into traditional fossil (oil, natural gas and coal), nuclear and renewable ones. The graph reported in Fig. 2.1-2 shows the shares of global energy consumption relative to each source, from 1966 to 2016. The traditional fossil sources, considered as a whole, still constitute the more exploited ones; even if their consumption is lower in respect to the past. Oil remained the world's leading fuel, accounting for a third of global energy consumption (see Fig 2.1-2). It gained global market share for the second year in a row, following 15 years of declines from 1999 to 2014. In 2016, global oil consumption growth averaged 1.6 million barrels per day (Mb/d), or 1.6%, above its 10-year average (1.2%) for the second successive year [BP, 2017]. China (400,000 b/d) and India (330,000 b/d) provided the largest increments. The regrowth of oil consumption is related to the progressive lowering of its price. In fact, the Dated Brent price averaged $43.73 per barrel in 2016, down from $52.39 per barrel in 2015 and its lowest (nominal) annual level since 2004 [BP, 2017].

Global oil production in contrast, rose by only 0.4 Mb/d in 2016, the slowest growth since 2013. Production in the Middle East rose by 1.7 Mb/d, driven by growth in Iran (700,000 b/d) Iraq(400,000 b/d) and Saudi Arabia (400,000 b/d). Production outside the Middle East fell by 1.3 Mb/d, with the largest declines in the US (-400,000 b/d), China (-310,000 b/d) and Nigeria (-280,000 b/d) [BP, 2017].

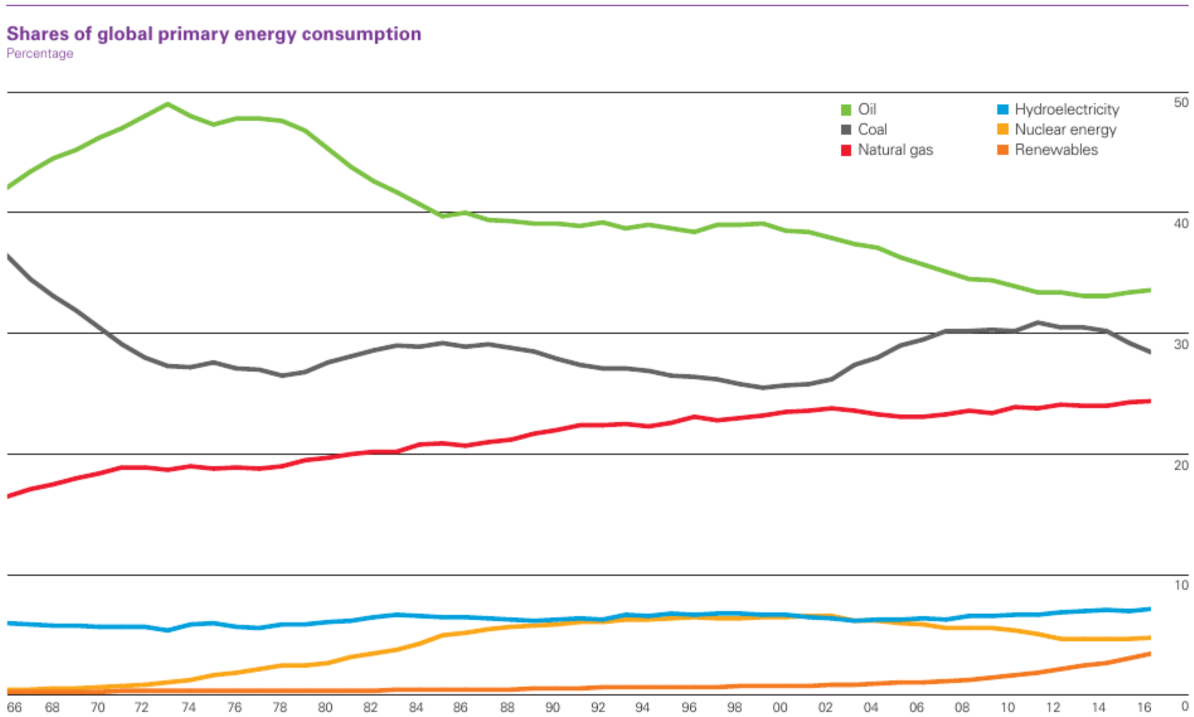

Fig 2.1-2 Shares of global primary energy consumption: percentage per year, from 1966 to 2016

Instead, natural gas consumption share experienced an almost constant growth in the last 50 years, as we can see in Fig. 2.1-2. World natural gas consumption grew by 63 billion cubic metres (bcm) or 1.5% in 2016, slower than the 10-year average of 2.3%. Contrariwise, EU gas consumption rose sharply by 30 bcm, or 7.1%, that is the fastest growth since 2010. Russia saw the largest drop in consumption of any country (-12 bcm). Global natural gas production increased by only 21 bcm, or 0.3%. Declining production in North America (-21 bcm) partially offset strong growth from Australia (19 bcm) and Iran (13 bcm). Gas trade grew by 4.8%, helped by 6.2% growth in liquefied natural gas (LNG) imports/exports. Most of the net growth in LNG exports came from Australia (19 bcm out of 21). US LNG exports rose from 0.7 bcm in 2015 to 4.4 bcm in 2016 [BP, 2017].

Considering the latter traditional fossil source, global coal consumption fell by 53 million tonnes of oil equivalent (mtoe) in 2016, or 1.7%, the second successive annual decline. The largest declines in coal consumption were seen in the US (-33 mtoe, an 8.8% fall) and China (-26 mtoe, -1.6%). Coal consumption in the UK more than halved (down 52.5%, or 12 mtoe) to its lowest level in our records. Coal's share of global primary energy consumption fell to 28.1%, the lowest share since 2004 (see Fig 2.1-2). World coal production fell by 6.2%, or 231 mtoe, the largest decline on record. China's production fell by 7.9% or 140 mtoe, also a record decline. US production fell by 19% or 85 mtoe [BP, 2017].

Nuclear source is widely considered non-renewable as the traditional fossil ones, even if a debate on it is still opened. In respect to the traditional fossil sources, nuclear is cleaner if pollutants emissions are considered. As shown in the graph in Fig. 2.1-2, the share of nuclear energy consumption had a decrease in the past 15 years. Actually, global nuclear power generation increased by 1.3% in 2016, or 9.3 mtoe, driven by emerging economies. In fact, China accounted for all of the net growth, expanding by 24.5%. China's increment (9.6 mtoe) was the largest of any country since 2004 [BP, 2017].

Renewables consumption share experienced the bigger growth in the last years, as shown in Fig. 2.1-2. In 2016, the renewable power (excluding hydro) grew by 14.1%, below the 10-year average, but the largest increment on record (53 mtoe). Wind provided more than half of renewables growth, while solar energy contributed almost a third, despite accounting for only 18% of the total. Asia Pacific overtook Europe & Eurasia as the largest producing region of renewable power. China overtook the US to be the largest single renewables producer [BP 2017]. Hydroelectric power generation rose by 2.8% in 2016, (27.1 mtoe). China (10.9 mtoe) and the US (3.5 mtoe) provided the largest increments. Venezuela experienced the largest decline (-3.2 mtoe) [BP, 2017].

One of the most important point related to renewable energy production growth is the greenhouse gas, in particular CO2, emissions reduction. CO2 is one of the most abundant greenhouse gas in the earth atmosphere; others are water vapour, methane, nitrous oxide and ozone. The growth of greenhouse gases concentration in the atmosphere, is strongly related with the greenhouse effect, that is at the basis of global warming [Deaton and Winebrake, 2000]. Starting from the First Industrial revolution, CO2 emissions related to human activities strongly increased. For the most part they come from the combustion of fossil fuels (principally coal, oil and natural gas); with comparatively modest additional contributions coming from deforestation, changes in land use, soil erosion, and agriculture (including animal agriculture). In accordance with the growth of renewables and with the fell of coal used for energy production, the emissions of CO2 related to energy production increased by only 0.1% in 2016. Moreover, during 2014-16, average emissions growth has been the lowest over any three-year period since 1981-83 [BP, 2017].

Then, because of the environmental problems related to fossil source consumption for energy production, a significant increase in the amount of renewable sources use is expected in the next years. For example, the IEA's World Energy Outlook 2016 predicted that the amount of world power generation from renewables will reach 37% in 2040 (IEA, 2016). Moreover, international agreements have been reached in the aim of reduce the greenhouse gas emissions and slow down global warming, fostering the development on renewable power.

The most recent has been the “Paris climate agreement”, within the United Nations Framework Convention on Climate Change (UNFCCC) [United Nations, 2016]. This agreement deals with greenhouse gas emissions mitigation, adaptation and finance starting in the year 2020. The language of the agreement was negotiated by representatives of 196 parties and adopted by consensus on 12 December 2015. As of November 2017, 195 UNFCCC members have signed the agreement, and 170 have become party to it.

The Agreement aims to respond to the global climate change threat by keeping a global temperature rise this century well below 2 degrees Celsius above pre-industrial levels and to pursue efforts to limit the temperature increase even further to 1.5 degrees Celsius. In the Paris Agreement, each country determines, plans and regularly reports its own contribution it should make in order to mitigate global warming. There is no mechanism to force a country to set a specific target by a specific date, but each target should go beyond previously set targets.

EU directives are among the most ambitious in terms of growth in the share of energy produced from renewable sources. In fact, the EU's Renewable energy directive set a binding target of 20% final energy consumption from renewable sources by 2020 [European Union, 2009]. To achieve this, EU countries have committed to reaching their own national renewables targets ranging from 10% in Malta to 49% in Sweden (see Table 2.1-1). They are also each required to have at least 10% of their transport fuels come from renewable sources by 2020.

All EU countries have adopted national renewable energy action plans showing what actions they intend to take to meet their renewables targets. These plans include sectorial targets for electricity, heating and cooling, and transport; planned policy measures; the different mix of renewables technologies they expect to employ; and the planned use of cooperation mechanisms. Renewables will continue to play a key role in helping the EU meet its energy needs beyond 2020. EU countries have already agreed on a new renewable energy target of at least 27% of final energy consumption in the EU as a whole by 2030 as part of the EU's energy and climate goals for 2030. On 30 November 2016, the Commission published a proposal for a revised Renewable Energy Directive [European

Union, 2016] to make the EU a global leader in renewable energy and ensure that the 2030 target is met.

Public interventions such as support schemes remain necessary to make certain renewable energy technologies competitive. To avoid distorting energy prices and the market however, these schemes should be time-limited and carefully designed. The EU has issued guidance on support schemes to help governments when they design or revise support schemes.

Table 2.1-1: Share of Renewable energy (RE) of each EU member, and its 2020 target

Member State	RE Share 2013	RE Share 2014	RE Share 2015	RE Target 2020
EU-28	**15,0%**	**16,0%**	**16,4%**	**20%**
Austria	32,3%	33,1%	33,6%	34%
Belgium	7,5%	8,0%	7,3%	13%
Bulgaria	19,0%	18,0%	18,4%	16%
Croatia	28,1%	27,9%	27,5%	20%
Cyprus	8,1%	9,0%	9,1%	13%
Czech Republic	12,4%	13,4%	13,6%	13%
Denmark	27,3%	29,2%	30,6%	30%
Estonia	25,6%	26,5%	27,9%	25%
Finland	36,7%	38,7%	39,5%	38%
France	14,0%	14,3%	14,5%	23%
Germany	12,4%	13,8%	14,5%	18%
Greece	15,0%	15,3%	15,5%	18%
Hungary	9,5%	9,5%	9,4%	13%
Ireland	7,7%	8,6%	9,0%	16%
Italy	16,7%	17,1%	17,1%	17%
Latvia	37,1%	38,7%	39,2%	40%
Lithuania	23,0%	23,9%	24,3%	23%
Luxembourg	3,6%	4,5%	5,0%	11%
Malta	3,7%	4,7%	5,3%	10%
Netherlands	4,8%	5,5%	6,0%	14%
Poland	11,3%	11,4%	11,8%	15%

Portugal	25,7%	27,0%	27,8%	31%
Romania	23,9%	24,9%	24,7%	24%
Slovakia	10,1%	11,6%	11,9%	14%
Slovenia	22,5%	21,9%	21,8%	25%
Spain	15,3%	16,2%	15,6%	20%
Sweden	52,0%	52,6%	54,1%	49%
United Kingdom	5,6%	7,0%	8,2%	15%

Every two years, the EU publishes a renewable energy progress report. The 2017 report states that the EU as a whole achieved a 16% share of renewable energy in 2014 and an estimated 16.4% share in 2015 (see Table 2.1-1). The vast majority of EU countries are well on track to reach their 2020 binding targets for renewable energy, as shown in Table 2.1-1. The EU's initial efforts in promoting the use of renewables facilitated this continued growth which resulted in lowered renewable costs: the prices of photovoltaic modules fell by 80% between the end of 2009 and the end of 2015. Renewables have now become cost-competitive, and sometimes even cheaper than fossil fuels.

Finally, the renewable energy sector plays a key role for the EU economy with a turnover of around €144bn in 2014 and more than one million people employed. Considering the maturity of the sector, European investments have dropped by more than half since 2011 to €44bn last year, while global investments in renewable energy continue to increase to above €260bn. The Renewable Energy Directive has been and will continue to be a central element of the Energy Union policy and a key driver for providing clean energy for all Europeans.

2.2 The ocean energy source

The exploitation of ocean sources to electricity production could play an important role in the growth of the renewable energy share. Ocean energy sources can be classified into four categories: wave, tidal stream, tidal range and ocean thermal energy conversion [Boehlert and Andrew, 2010].

Waves are generated when the wind blows over the ocean’s surface, which itself is a function of temperature and pressure differences across the globe caused by the distribution of solar energy. Wave energy carries both kinetic and gravitational potential energy, the level of which is a function of both the height and period of the wave [Barstow et al., 2007]. Harnessing this energy using a Wave Energy Converters (WEC) can in turn generate electricity. Among ocean energy sources, waves represent a promising area thanks to its abundance. As reported in Table 2.2-1, the mean wave power experienced by the oceanic coastline is estimated to be about 2.11 TW all over the world and about 270 GW for the only Europe [Gunn and Stock-Williams, 2012]. It has been calculated at a buffer line running 30 nautical miles offshore, considering a distance that was compatible with WECs installation.

Table 2.2-1. Mean annual wave power, P, experienced by the oceanic coastline

Continent	P (GW)
North America	427 ± 18
Oceania	400 ± 15
South America	374 ± 16
Africa	324 ± 12
Asia	318 ± 14
Europe	270 ± 20

Fig. 2.2-1 [Cornett, 2008] shows in detail the mean wave power distribution in the world seas. Pacific and Indian Ocean receive the largest quantity of wave energy, with South parts receiving impressive amounts. Atlantic Ocean performs moderately well in its parts close to Western Europe and South Africa, respectively. Finally, Central America and the Mediterranean Sea and Atlantic Archipelagos perform poorly given their mid-latitude position.

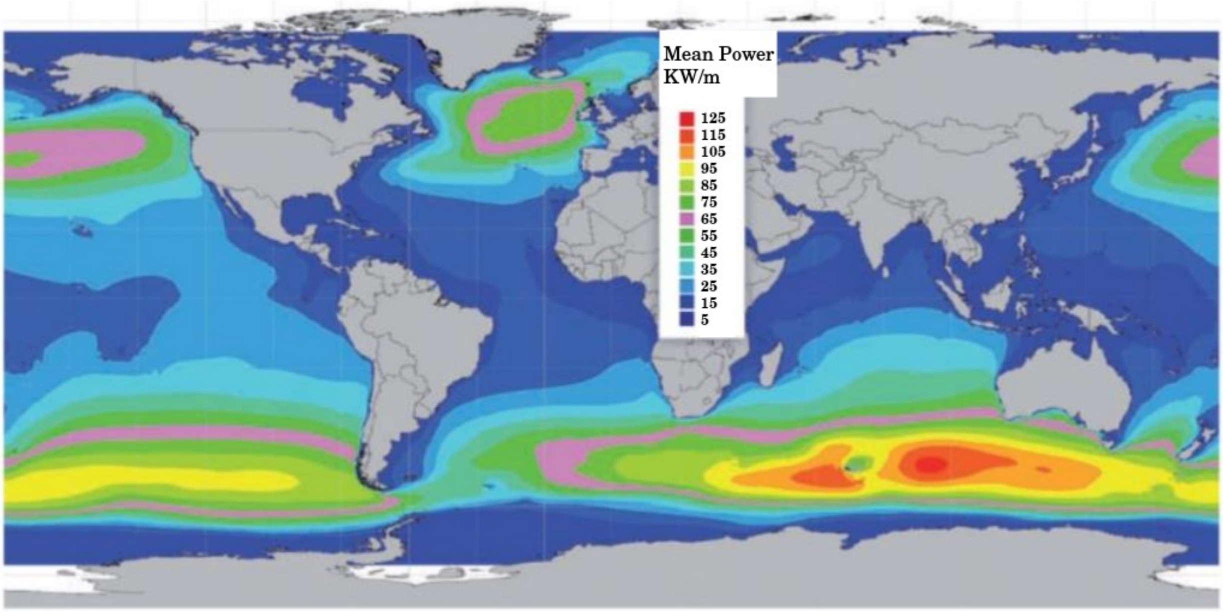

Fig. 2.2-1 Global annual wave power distribution

Focusing attention on the Italian coastline, Fig. 2.2-2 shows the map of the average annual wave energy calculated in the period 2001-2010. Sardinia and Sicily are the regions characterized by the highest values, in particular the whole west coast of Sardinia is affected by values above 12 kW/m. Along with this abundance, waves have some other favourable points in comparison with other more exploited renewable energy sources, such as solar and wind. First of all, their high power density (2-3 kW/m^2), which is greater than that of wind (0.4-0.6 kW/m^2) and solar (0.1-0.2 kW/m^2) [Lopez et al., 2013]. Moreover, wave energy devices can generate power up to the 90% of the time, in comparison to 20-30% for wind and solar devices [Lopez I. et al., 2013].

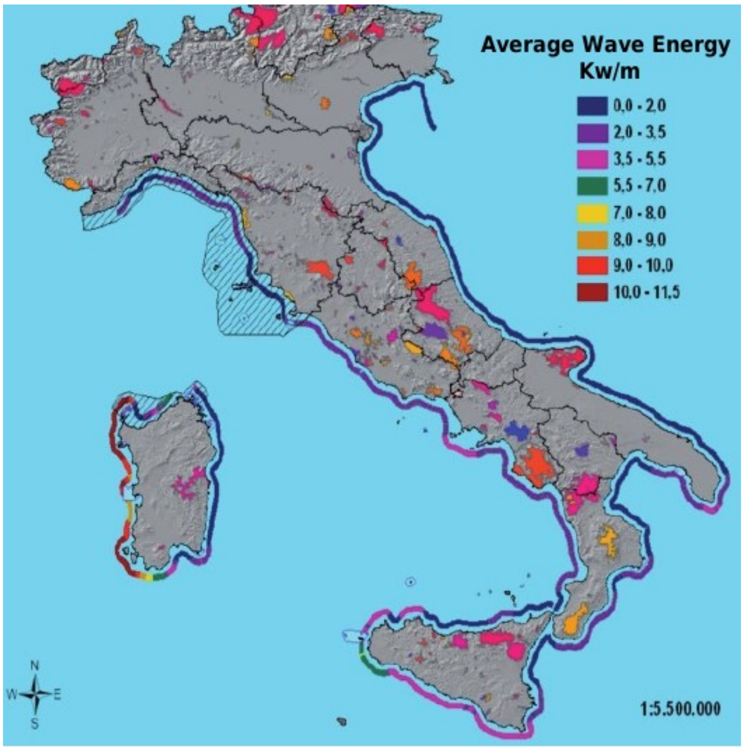

Fig. 2.2-2 Average wave energy distribution along the Italian coastline

Oceanic tides are the function of the motion of the moon and sun relative to the earth. These gravitational forces in combination with the rotation of the earth on its axis cause periodic movements of the oceans and seas. The vertical rise and fall of water, known as tides is accompanied by an incoming (flood) or outgoing (ebb) horizontal flow of water in bays, harbours, estuaries and straits. It is this flow that is known as tidal current or tidal stream. Tidal stream devices working in a similar fashion to wind turbines using water currents instead of wind to convert kinetic energy into electricity [Uihlein and Magagna, 2016]. The energy potential of tidal currents is typically located in areas with the greatest tidal range. Fig 2.2-3 shows the distribution of the tidal stream source in Europe.

As we can see, the potential increases in areas where the flow of water is constrained or funnelled by local topography such as narrow straits and headlands, and where the water depth is relatively shallow. In particular, large marine current flows exist where there is a significant phase difference between the tides that flow on either side of large islands [Aqua-RET, 2017]. In Italy, Strait of Messina is the only place suitable for tidal stream energy exploitation.

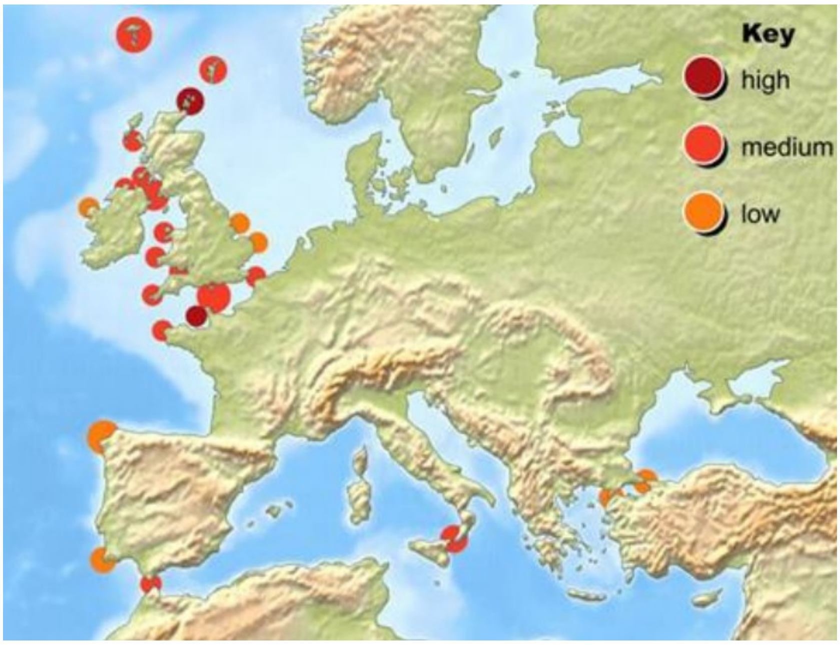

Fig. 2.2-3 European tidal stream resource distribution

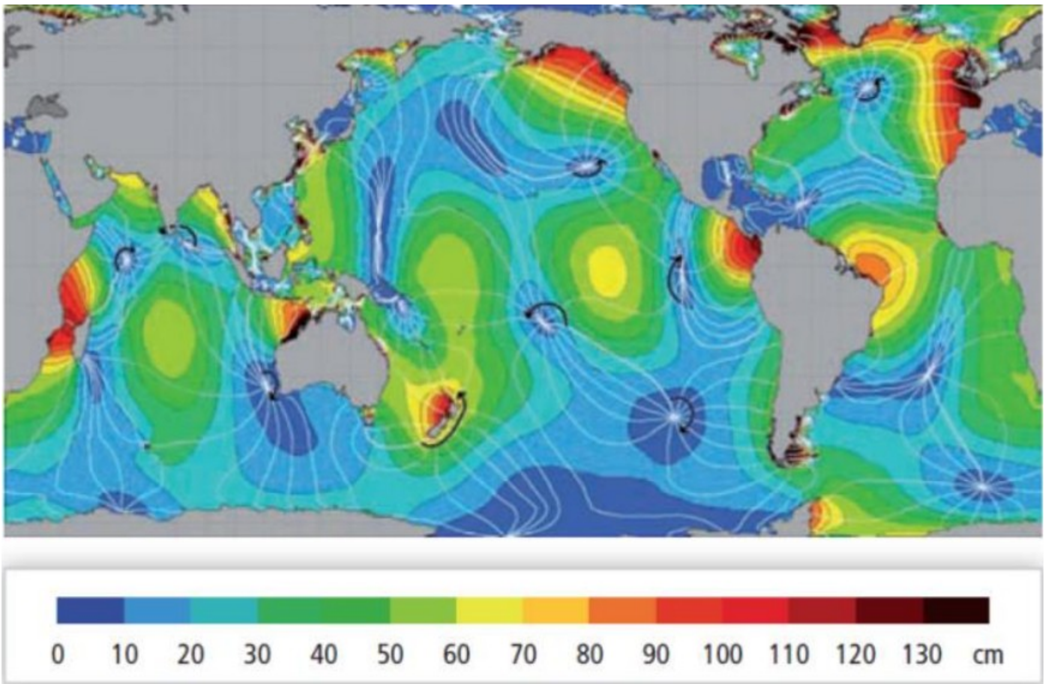

Fig. 2.2-4 Global semi-diurnal tidal amplitude (cm)

It is difficult to identify reliable estimates for global tidal stream energy potential but Charlier & Justus [Charlier and Justus, 1993] estimate total tidal energy potential (i.e. tidal range and tidal stream) at 3 TW, with 1 TW located in relatively shallow waters. However, due to geographical, technical and environmental constraints only a fraction of this could be captured in practical terms. In practice, suitable locations need mean spring peak tidal currents that are faster than 2-2.5 m/s to offer an energy density that allows for an economically viable project [Charlier and Justus, 1993], accounting for the fact that as the tide changes there will be little or no horizontal flow of water [Mofor et al., 2014]. Importantly, major tidal streams have been identified along the coastlines of every continent, making it a global, albeit site specific, resource [Mofor et al., 2014]. For example, at the European level 106 locations with a strong tidal stream potential were identified, together offering 48 TWh/yr (0.17 EJ/yr) of potential resource [CEC, 1996]. A similar study examined Europe's tidal stream potential identifying that it was predominantly concentrated around the British Isles and English Channel, (see Fig. 2.2-3).

The difference in sea level between high and low tide is known as the tidal range. At most coastal sites high and low tides occur twice a day (semi-diurnal tides), however in some places just one high and low tide takes place per day (diurnal tides) whilst others experience a combination of diurnal and semi-diurnal oscillations (mixed tides) [Mofor et al., 2014].

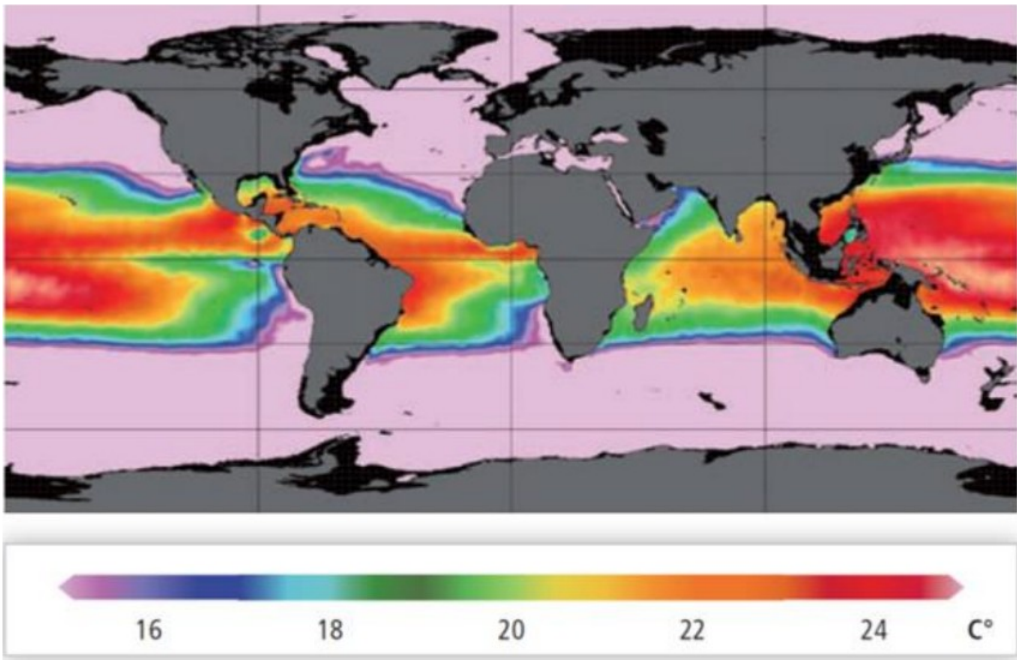

Fig. 2.2-5 Worldwide average ocean temperature differences (°C) between 20 and 1000 m water depth

Even so these tides have been studied for centuries and can be easily forecast meaning that tidal range energy offers both a consistent and predictable form of energy. Figure 2.2-4 demonstrates how the tidal range resource potential varies considerably across the globe and is amplified by basin resonances and coastline bathymetry to create large surface elevation changes at specific geographic locations [Mofor et al., 2014]. Consequently, some areas exhibit huge tidal ranges, like the Bay of Fundy in Canada (17 m tidal range), Severn Estuary in the UK (15 m) and Baie du Mont Saint Michel in France (13.5 m) [Kerr, 2007].

In contrast other locations such the Mediterranean see a tidal range of less than 1 m [Kerr, 2007].

Approximately 15% of the total solar energy falling incident on the oceans is retained as thermal energy and stored as heat in the upper layers of the ocean [Lewis et al., 2011]. This energy is concentrated in the top layers and falls exponentially with depth as the thermal conductivity of sea water is low [Lewis et al., 2011]. As illustrated by Figure 2.2-5, the temperature differential in the tropics can exceed 25°C between 20 m and 1 km in depth [Nihous, 2010]. The temperature gradient between the relatively warm sea surface water and the colder, deep seawater can be harnessed using different ocean thermal energy conversion (OTEC).

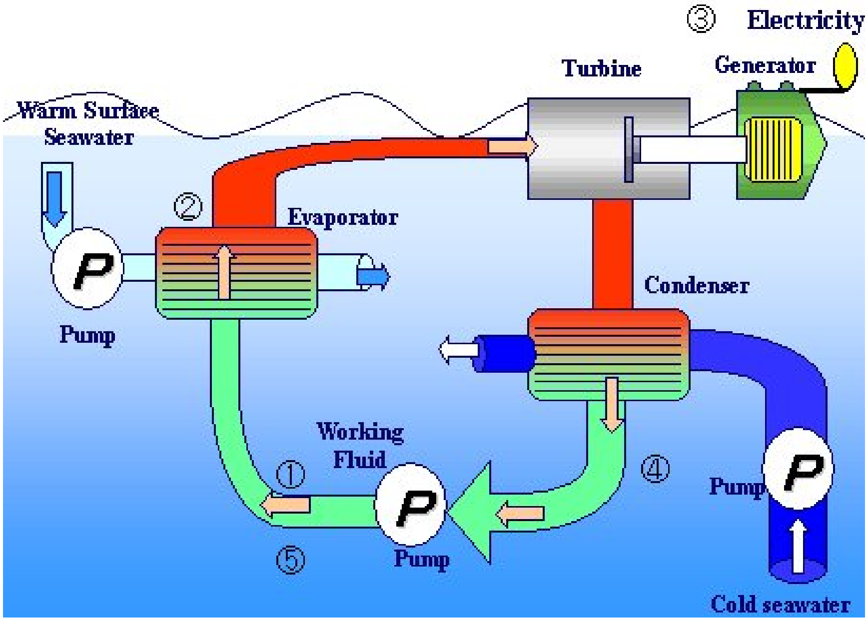

Fig. 2.2-6 Schematics of a OTEC plant operating principle

The schematics of the operating principle of a OTEC device are shown in Fig. 2.2-6. OTEC typically requires a differential of about 20°C to work effectively meaning where cool water (~5°C) is drawn from depths of around 800–1000 m and surface water temperatures sit at a constant 25°C [CRRC, 2010]. Consequently, its potential application is limited to between 35° latitude north and south of the equators. Whilst small seasonal variations do occur this energy potential is available all-year round, although its power density is considered relatively low [Mofor et al., 2014] and [Lewis et al., 2011]. Estimates of the total potential global OTEC energy resource that could be extracted without having a major impact on the thermal characteristics of the world’s oceans range between 30 and 90 Pwh [Pelc and Fujita, 2002]. On this basis there is a much larger potential resource versus the other forms of ocean energy. However, the resource that could practically and economically be captured is significantly limited by economic and technical constraints.

It is difficult to draw a meaningful comparison of the theoretical global energy resource for each of these technologies but, in general, wave energy and OTEC have a more abundant and spatially distributed resource versus tidal stream and range [World Energy Council, 2016]. Taken together, ocean energy presents a huge untapped resource available to most coastal countries in one form or another. However, at to date only a handful of commercial ocean energy projects have been delivered, reflecting the current immaturity and high costs of these technologies, as well as the challenging market environment in which they operate. In fact, only 0.5 GW of commercial ocean energy generation capacity is in operation and another 1.7 GW under construction, with 99% of this accounted for by tidal range.

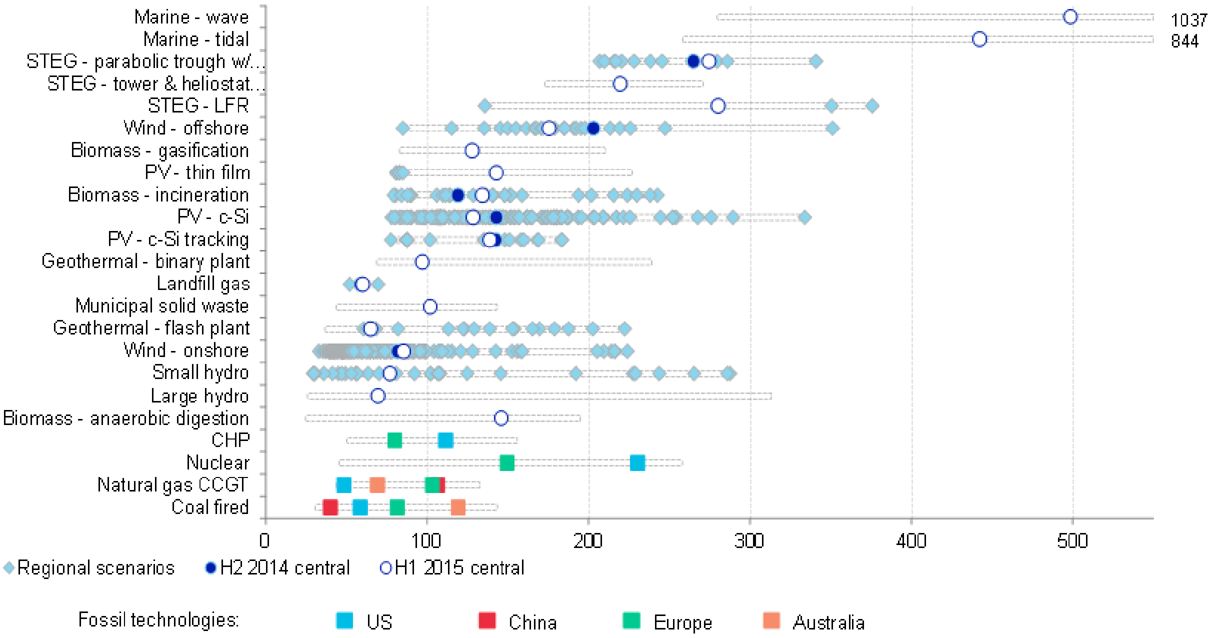

Fig. 2.2-7 Levelised cost of electricity technologies ($/Mwh) for 2015

While relatively few commercial scale wave, tidal stream or OTEC projects are operational we find three tidal stream commercial projects accounting for 17 MW of capacity (two in Scotland and one in France) and a 1 MW commercial wave energy array in Sweden are to be commissioned shortly. A host of OTEC projects are also gathering momentum, with two 10 MW schemes being developed, one by DCNS in Martinique and the other by Lockheed Martin in China. If all planned commercial projects reach fruition then an additional 15 GW of ocean energy capacity will come online over the coming years, however in reality a fraction of this is likely to be delivered.

Whilst the traditional leaders of this sector, namely the UK and US, continue to develop flagship projects we find other countries such as South Korea, Ireland, the Netherlands and China are now challenging their dominance. Despite these positive developments a large number of projects have been suspended largely as a result of public and private funds having been withdrawn due to slow economic growth, falling oil prices and a failure by marine energy technology developers to deliver on initial expectations about their technologies' potential cost-effectiveness. The wave energy sector has been hit particularly hard by leading companies such as Pelamis and Aquamarine falling into administration. Looking forward we find that the respective costs of these different ocean energy technologies remain a significant barrier to deployment.

For example, Bloomberg New Energy Finance's (BNEF) analysis of energy technologies levelised cost of electricity (LCOE) identifies the major disparity between the cost of ocean energy versus other forms of generation (Figure 2.2-7) [BNEF, 2015]. The central scenario for 2015 (H2) estimates the LCOE of wave energy at approximately US$500/MWh whilst tidal sits at approximately US$440/MWh. It could be argued that there is a stronger degree of certainty over the costs of tidal versus wave energy given the stronger technological convergence and greater installed capacity. More broadly, Figure 1.2-7 illustrates the extremely high cost of ocean energy versus other renewables, for example offshore wind (US$174/MWh), crystalline silicon solar PV (US$122/MWh), onshore wind (US$83/MWh) and large hydro (US$70/Mwh) [BNEF, 2015].

BNEF's analysis does not cover OTEC and so in order to offer a more complete picture we consider a review conducted by Kempener and Neumann [Kempener and Neumann, 2014a]. They identified that the LCOE for small-scale OTEC plants (1-10MW) ranges somewhere between US$190/Mwh and US$940/MWh, however if the facility were to be scaled up to between 50-400 MW the cost would fall dramatically and likely range between US$70/MWh and US$320/Mwh. These high costs illustrate the immaturity of these technologies and the relatively short gestation period that ocean energy technologies, with the exception of tidal range, have undergone.

Consequently, many of the cost issues could be addressed through ongoing RD&D efforts. Tidal range is slightly different in the sense that the technology was first installed on a commercial basis in mid-20th century in countries like Canada, France and China. Consequently, the underpinning technological principles are well understood and many of the installations have operated without significant issues suggesting that further RD&D is unlikely to dramatically reduce its costs [Kempener and Neumann, 2014b]. Even so, it is possible to improve the relatively poor load factor (25%) of tidal range technology due to tidal cycles and turbine efficiency and in turn improve its LCOE by using multi-basin designs and/or turbines for ebb and flood generation [Kempener and Neumann, 2014b].

Whilst not always the case, energy technology costs typically fall as deployment increases due to a combination of learning by doing and learning by using, as well as other factors such as supply chain maturity and increased investor confidence. In this context we find that ocean energy costs are expected to fall with increased deployment and that the LCOE of wave, tidal stream and OTEC could fall in line with today's cost of competing renewable and fossil fuel technologies [BNEF, 2015].

3. Wave energy converters (WECs)

3.1 WECs main aspects and classifications

Wave energy converters (WECs) can be traced back to 1799, when Pierre Girard and his son filed the first converter patent in France. Since then, more than one thousand prototypes of WECs have been developed over the years in the aim of wave power exploitation [Drew et al., 2016]. Currently, 838 MW of wave energy projects are at different stages of development, however only 20 MW of this has received authorised consent, as reported in Fig. 3.1-1. In addition, there is 94 MW at the early planning and 725 MW at the early concept stage.

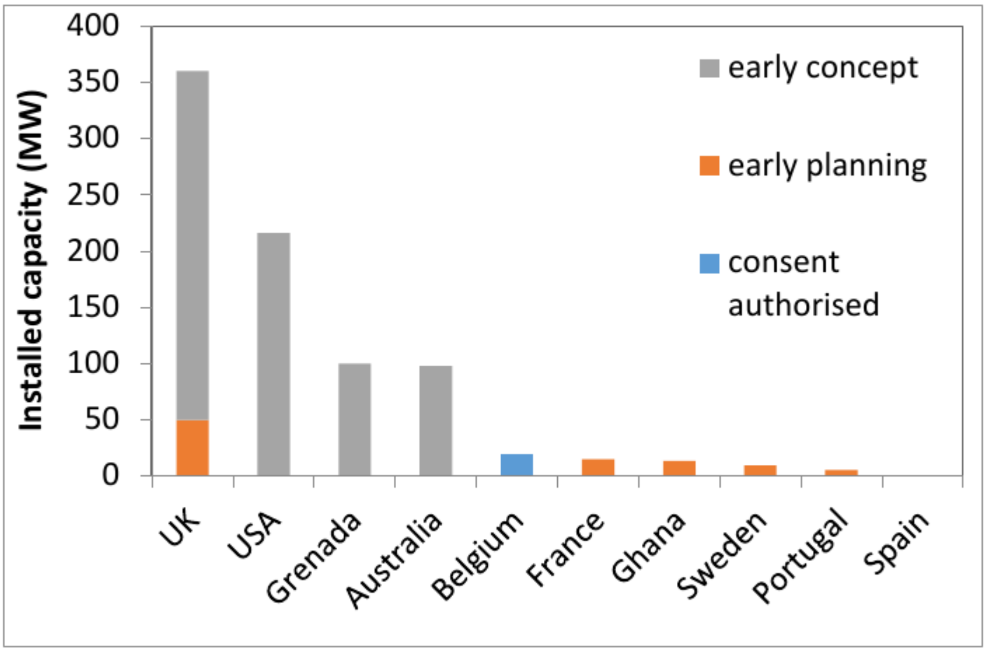

Fig. 3.1-1 Wave energy installed capacity in development

A WEC is generally composed by six mean components:

1. Structure and Prime Mover: The physical structure of the device which captures energy and the main interface between the resource and the power take off equipment within the ocean energy converter. The predominant structural material is steel, although certain concepts are exploring alternatives. Prime movers such as turbine blades are made of composite materials.

2. Foundations and Moorings: The method used to secure the device to the sea bed. This includes permanent foundation constructions such as gravity bases or pile-pinned foundations, or could consist of moorings such as tight or slack moored systems.

3. Power Take Off: The means by which the mechanical energy extracted from the waves is converted into electrical energy. Several types of Power Take Off (PTO) exist including mechanical, hydraulic, or electrical direct drive using permanent magnet generators.

4. Control: Systems and software to safeguard the device and optimise the performance under a range of operating conditions. Control systems may adjust certain parameters of the device autonomously in order to ensure favourable operation.

5. Installation: The method of placing the structure and device at its power generating location. This includes all vessels and ancillary equipment needed to fully deploy an ocean energy device.

6. Connection: The cables and electrical infrastructure for connecting the power output from the device to the electricity network. Alternatively, water is pumped ashore for conversion to electricity and/or desalinated water. Subsequently, power conditioning systems and transformers are needed to provide a grid code compliant electrical output.

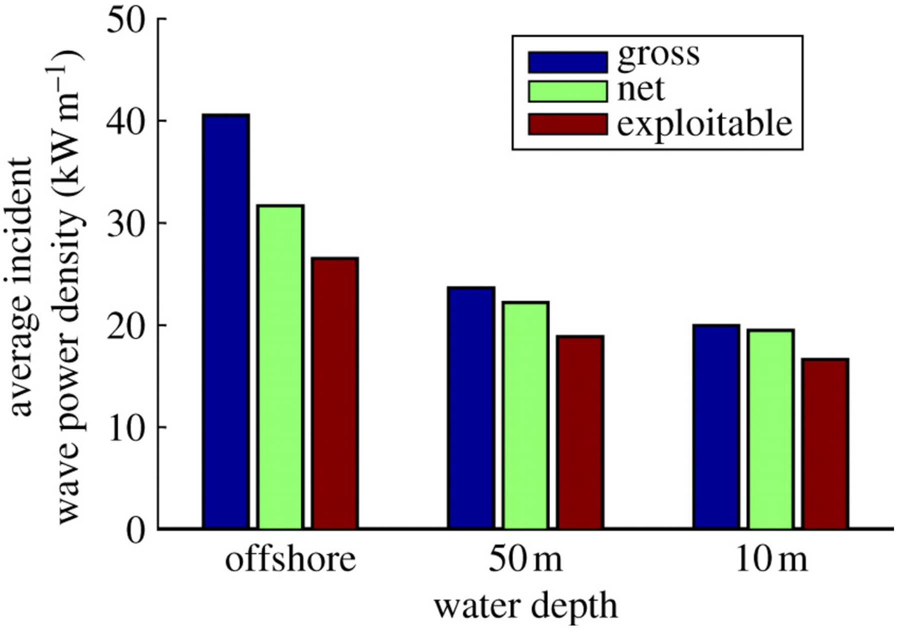

Fig. 3.1-2 Typical values of the exploitable wave energy as a function of the water depth

A first important classification of the different types of WECs can be carried out considering the the distance between the coast and the place where the device is installed. There are three possibility of installation: onshore, nearshore and offshore. The onshore converters are located at the shore and can be placed above the sea, in shallow water (water depth less than 10m). They can be integrated in breakwaters, in dams, or fixed to cliffs. The main advantage of these converters is their easier maintenance and installation, in respect to nearshore and offshore devices. Moreover, they do not need neither mooring systems nor a long lengths of sea cable to connect the WEC to the grid. However, at the shoreline waves contain less energy because their interaction with the seabed, and environmental problems could also arise due to shore reshaping. The nearshore converters are installed a few hundred of meters from the shore in moderate water depths (10 – 25 m). They usually rest on the seabed (avoiding moorings) but the structure must bear the stress that arises when the waves pass over it. In other cases, they are floating structures too. Finally, the offshore devices are located in deep waters (more than 40 m), far from the shore, and built in floating or submerged structures moored to the seabed. Due to their location, they might exploit the vast wave power of the open sea. In fact, as we can see in the graph in Fig, 3.1-2, the average water density increases with the water depth.

In the graph, gross power is the one of waves coming from all direction; whilst exploitable refers to the power of waves that only comes perpendicularly to the WEC, and that are exploitable for energy conversion. The values refers to an analysis of the wave resource at EMEC on the west coast of Orkney (UK) [Whittaker and Folley, 2001]. Together with the possibility of exploit a larger amount of wave power, offshore e installation presents some challenges. In fact, because of the open sea, the reliability and survivability of the devices is a big problem, and their structure has to bear very high loads. Moreover, their maintenance is a complicated and expensive process, and long length expensive sea cables are needed to carry the energy to the grid.

Finally, WECs can be also classified considering their working principle. There are four mean types: floating, oscillating wave surge, over-topping and pressure differential devices. In the next sections each type of WECs will be explained, analysing the most important achievements and the further developments.

3.2 Floating devices

Floating devices are essentially constituted by one or more floating bodies that are moved by the waves. The usable oscillatory movement may be vertical, horizontal, pitch one or a combination of them. Moreover, this movement can be induced either by an absolute motion between the floating body and an external fixed reference or by a relative motion between two or more bodies.

Actually, floating devices can be divided into two main groups in accordance with the size and direction of the device regarding the incoming wave. The first are the attenuator-type devices, that are long structures compared with the wavelength and are placed in parallel with respect to the wave direction. Their name derive to the fact that they work like “attenuate” the amplitude of waves. Generally, these type of WECs are composed by a series of floating platforms linked together by flexible hinged joints, that allow the platforms to rotate relative to each other. Actually, into each platform there are rems, each of one is connected with the adjacent ones by joints at the ends.

The rotational relative motion between the floating platforms pressurize the oil present into the rems, pumping it to the oleodynamic rotor that moves the electric generator. The most significant achievement, of this type, has been the UK's Pelamis device (Fig. 3.2-1) [Carcas, 2003]. Pelamis (formerly known as Ocean Power Delivery) entered the market in 1990s, committing significant resources towards developing its devices during the 2000s. The context was characterized by growing concerns about climate change, energy security and increasing oil prices. In 2003, the European Marine Energy Centre (EMEC) Ltd was established, a centre offering 'at-sea' testing capabilities for both wave and tidal energy devices in both challenging and less challenging (nursery) conditions.

This enabled Pelamis to become the first company in the world to generate electricity into a grid system from an offshore WEC in 2004 and the first to deliver a wave energy array, installing 3 Pelamis devices (2.25 MW total nominal rating) off the coast of Portugal at Aguacadora in 2008. Unfortunately, this was decommissioned shortly after due to technical faults [Cleveland, 2014].

Fig. 3.2-1. The Pelamis WEC

We are considering point absorbers devices if the WEC main dimension is significantly smaller then wavelength, instead. The name is due to the fact that, unlike the previous ones, point absorbers harvest ocean energy from all directions generating the movement of a floating structure in one point. To this category of devices belonged Stephen Salter's 'the Salter Duck', developed in the UK during the 1970s [Salter, 1993] and which gathered pace at wave energy innovation.

The IPS buoy [Falcão et al., 2012] adopted the solution of convert the relative (essentially heaving) motion between two bodies oscillating differently in electricity. The device consists of a floater rigidly connected to a fully submerged vertical tube open at both ends (Fig. 3.2-2). The tube contains a piston that moves relative to the floater-tube system, due to the wave action on the floater and to the inertia of the water enclosed in the tube. The relative motion between the piston and the tube is converted by a linear generator into electricity.

Currently, several projects on point absorbers device are under development. Sweden's Seabased has begun construction the world's largest commercial wave energy array at Sotenas (Sweden) [Chatzigiannakou et al., 2017]. It will incorporate 42 devices and deliver 1.05 MW of capacity. They have also recently installed a second project in Ghana consisting of 6 devices, together providing 400 kW of capacity. Importantly a second phase of both Seabased's projects in Sweden and Ghana are at an early planning stage and will be contingent of the performance of the first phase. The former delivering a further 378 devices and 9.5 MW of capacity, with the second delivering a further 560 devices and 14 MW of capacity.

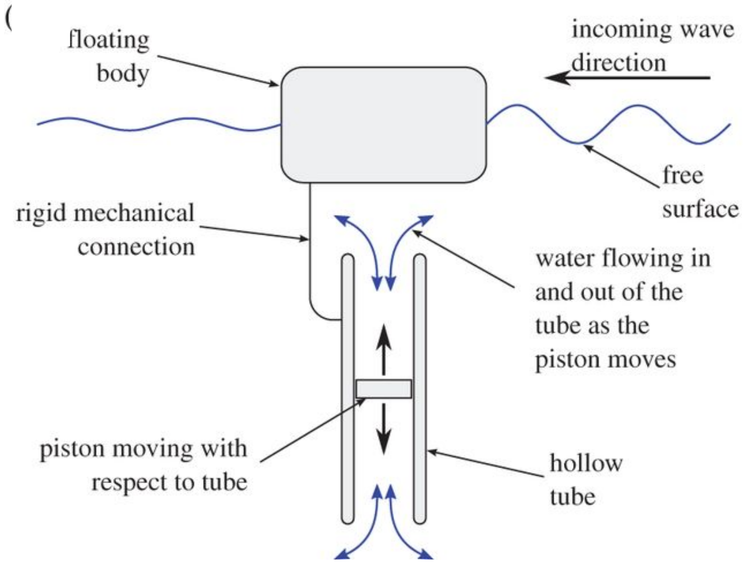

Fig. 3.2-2. Schematics of the IPS point absorber device

A host of pre-commercial demonstration projects are also underway and one of the highest profile has been in Australia where Carnegie has demonstrated 3 of its CETO 5 devices rated at 240 kW off Garden Island. The name is inspired by the Greek ocean goddess, Ceto, and the devices are actually submerged buoys that are moved by the ocean swell. The floating motion drives pumps that pressurize seawater delivered ashore by a sub-sea pipeline. Once onshore, the high-pressure seawater is used to drive hydro-electric turbines, generating electricity. The high-pressure seawater can also be used to supply a reverse osmosis desalination plant, producing freshwater. Some historic conventional seawater desalination plants are large emitters of greenhouse gases; this is due to the amount of energy required to drive the grid-connected pumps that deliver the high-pressure seawater to reverse osmosis membranes for the removal of the salt [McCallum P. et al., 2014].

At the early concept stage is Ocean Power Technologies, three major commercial projects in Australia equating to almost 100 MW and developing the Power buoy device [Harries et al., 2006].

Finally, considering the innovathive concepts, University of Genoa (Italy) developed a wave energy converter for off-shore applications named the Seaspoon. It is a wave energy converter (WEC) that catches the energy content of oceans waves exploiting the circular motion of the water particles perturbed at the free surface by the action of the wind. The performances of the Seaspoon device have been analyzed both experimentally [DiFresco and Traverso, 2014] and by means of CFD simulations [Reboli et al., 2017].

3.3 Wave surge converters

The operating principle of the oscillating wave surge converters is similar to the floating devices one. In this case, the surge motion of articulated or flexible floating structures, positioned perpendicular to the waves direction, is converted into electricity. In fact, as shown in the schematics in Fig. 3.3-1, a paddle hinged to the seabed moves back and forth due to waves. Hydraulic rumps are linked to the paddle by and end and to the platform fixed on the seabed by the other. The oscillating surge movement of the paddle, due to waves, pumps the rumps oil to the hydraulic motor that drives the generator. An example of such devices is the Aquamarine Power Oyster [Whittaker and Folley, 2012].

The Portugal's 5.6 MW SWELL project north of Peniche Peninsula is at the early planning stage and will consist of sixteen 350 kW oscillating Wave Surge Converters, named WaveRoller.

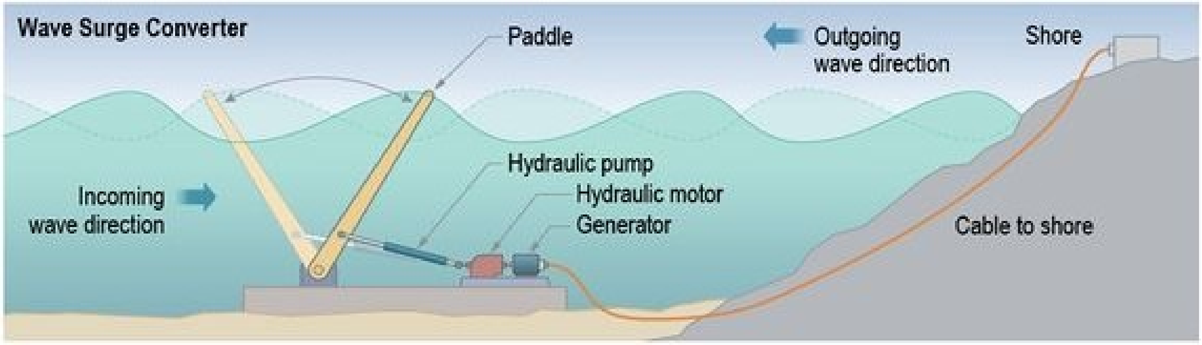

Fig. 3.3-1. Schematics of an oscillating wave surge converter

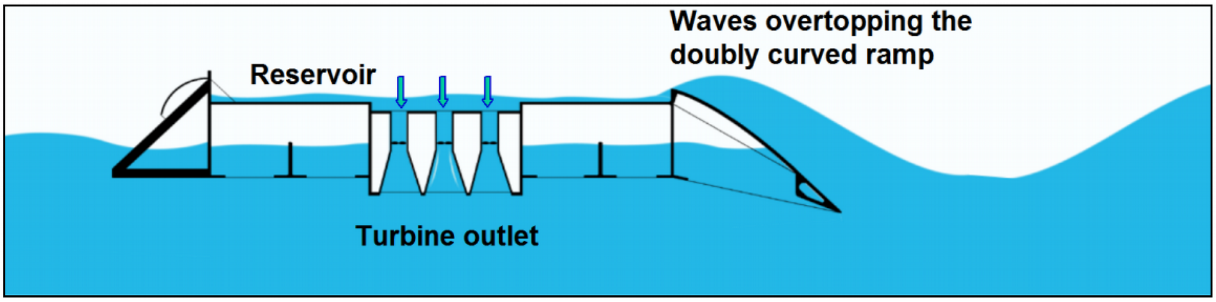

Fig. 3.4-1. Operating principle of an over-topping WEC

3.4 Over-topping devices

Unlike the previous two types of WECs, over-topping devices operating principle is not based on the conversion of the motion imposed by waves to a floating object into electricity. In this case, waves affect a structure which increases its potential energy, kinetic, or both. Then, the over-topping converters work like hydroelectric dams, with waves rolling into collectors which funnel the water into hydro turbines, as shown in Fig. 3.4-1. Significant realization of such converters have been the Wave Dragon, 4 –10 MW [Kofoed et al., 2006] depending on how energetic the wave climate is at the deployment site, and the TAPCHAN [Tjugen, 1993].

3.5 Pressure differential devices and OWCs

Finally, the pressure differential devices exploit the variation of the geodetic load, due to the passage of a wave crest or trough respectively, to generate power. They can be subdivided in two subcategories: Archimedes effect converters and Oscillating Water Columns (OWCs) devices. The former are submerged point absorbers typically located near shore and fixed to the seabed. As shown in Fig. 3.5-1, they are constituted by a floater that is connected by a linear generator to a fixed basement. When the crest of the wave is over the device, the water pressure increases and compresses the air that is inside the floater, moving it down. In the other case, when it is the through over the device, the water pressure will be reduced and the floater rises. Then the floater moves alternately up and down, allowing power generation by the linear generator. A significant example of this type of converter is the Archimides Wave Swing (AWS) [de Sousa Prado et al., 2006]. AWS Ocean Energy have proposed a two phase project in the north of Scotland, the first phase would be for 4 devices (10 MW) and the second for 76 devices (190 MW). However, given the early stage of these projects very little capacity is expected to come online in the near future.

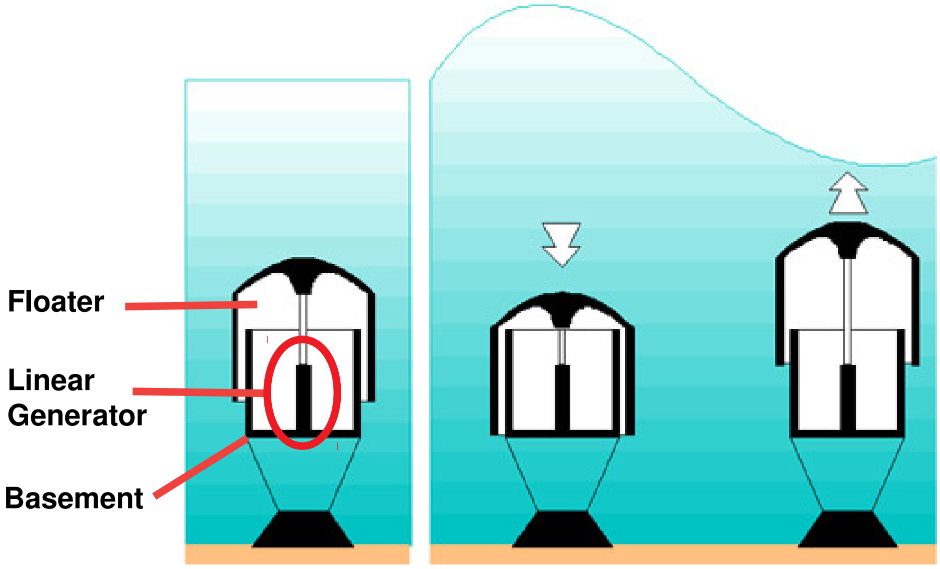

Fig. 3.5-1. Operating principle of an Archimedes Converter

Otherwise, the OWCs converters, based on the Yoshio Masuda's invention [Masuda et al., 1981], are essentially composed by a partially submerged plenum chamber where an air pocket is trapped. This chamber has an opening to the sea and an upper duct connects the air pocket to the atmosphere. Under the action of the incident sea waves, the free water surface oscillates vertically in the plenum chamber. In fact, when a wave crest is over the chamber opening, the water level inside the chamber rises, due to the increase of the geodetic load. This generates a compression of the air inside the chamber, that is pushed to the atmosphere through the air duct. When a wave trough is over the chamber opening, instead, water level inside the chamber drops, decompressing the air pocket and sucking air from the atmosphere into the chamber. As a result, an oscillating air flow is generated through the air duct, which moves the PTO-system (Power Take Off) spliced into this, as shown in the schematics in Fig. 3.5-2.Most commonly, self-rectyfing air turbines are used in OWC plants, as Wells turbine (Fig. 3.5-3) and impulse ones (Fig. 3.5-3).

In comparison to the others WECs, in OWCs there are not parts which are moved by waves or in relative motion between them. Then, maintenance of OWCs is simpler and the failure risk is lower in respect to the others WECs. For these reasons, OWC converters have been ones of the most tested WECs, both experimentally and numerically.

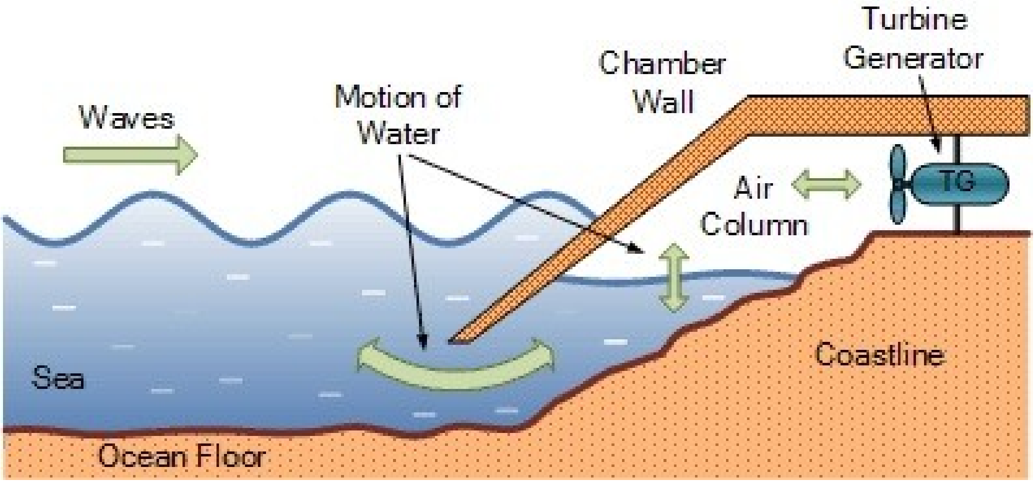

Fig. 3.5-2 Operating principle of OWCs

OWCs were the first devices to reach the development phase. Norway in 1985 launched the world’s first wave power station: two full-sized (350 and 500 kW rated power) shoreline OWC prototypes at a site near Bergen [Falcão and Henriques, 2016]. UK followed in 1991 by installing its own 75 kW prototype Limpet OWC [Whittaker et al., 1997] on Islay, Scotland, officially the UK’s first commercial wave energy plant. Despite the encouraging first developments, confidence in OWCs was soon shaken following the high-profile sinking of a 2 MW OWC ‘OSPREY’ device on its UK launch in 1995 following damage from a storm while still undertaking installation. Despite this setback the UK delivered the world’s first commercial grid connected wave energy device when it commissioned its upgraded 500 kW Limpet device on Islay in 2001 [Boake et al., 2002].

In the years, several analysis have been carried out in order to improve the OWC design. The hydrodynamic performance of inclined bend-free [Ram et al., 2016], fixed [Ning et al., 2016] or floating [Gomes et al., 2015] OWCs under various wave conditions and geometric parameters has been experimentally tested in wave flumes.

The air chamber performance has been analysed both experimentally and numerically including the damping effect of the PTO-system. In fact, the relationship between the PTO damping and the OWC hydrodynamics can be used to improve the efficiency of the OWC. Numerical modelling is useful for carry out an evaluation of the performance of OWC operating under different values of PTO damping for different incident wavelengths. Didier et al. [Didier et al., 2011] explored the use of porous media theory to develop a numerical model of the PTO damping effect by means of a linear pressure drop law on a simplified representation of the OWC device as a thin cylinder.

The numerical results have been validated comparing them with the experimental results collected from a physical model. In that physical model, the turbine damping effect was simulated by a piece of porous membrane (textile) placed on the top of the cylinder. López et al. [Lopez et al., 2014] studied the optimization of turbine induced damping on an OWC device using a CFD model, after validating the model with data from physical model tests. In both the physical and CFD model, the effect of the turbine damping has been modelled by opportunely dimensioning the area of the orifice at the top of the OWC chamber. Kamath et al. [Kamath et al., 2015] analysed the performance of an OWC device under a range of wavelengths for different wave steepness by means of CFD simulations.

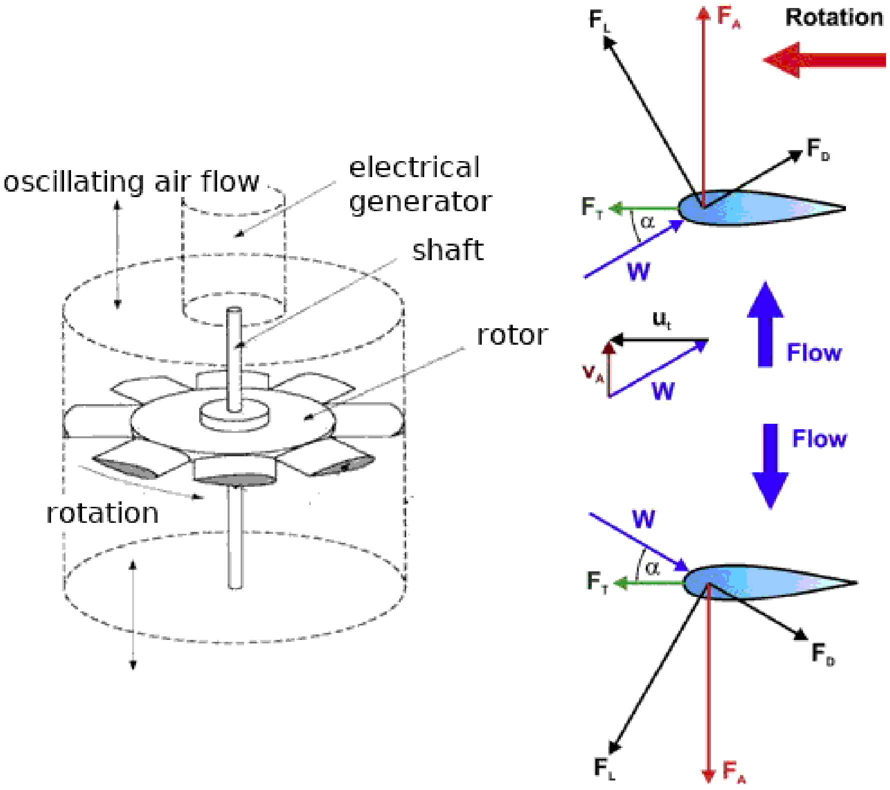

Fig. 3.5-3 A Wells turbine, with the aerodynamic forces on the profile during its operation

Moreover, in the aim of their utilization as PTO-systems for wave energy conversion, both Wells and impulse turbines have been examined in various configurations. In particular, the

Wells turbine [Raghunathan, 1995] is a kind of self-rectifying axial flow turbine suitable for the conversion of the kinetic energy of an oscillating air flow to mechanical energy to the turbine shaft. In order to improve the energy conversion process, the turbine should have good efficiency for a wide range of flow-rates [Raghunathan, 1995],[Curran et al., 1997]. To this purpose, several experimental analyses have been carried out in order to investigate the performance of Wells turbines. For instance, wind tunnel tests have been considered under both constant or reciprocating flow conditions [Torresi et al., 2007], using scaled devices [Filianoti and Camporeale, 2009], or in operative plants, such as the LIMPET [Heath, 2009] and the PICO ones [Falcão, 2001]. More detailed investigations of the fluid dynamics of Wells turbines have been carried out by means of CFD analysis, regarding either low solidity hydraulic Wells turbines [Camporeale et al., 2003], or high solidity Wells turbines [Dhanasekaran and Govardhan, 2005], [Torresi et al., 2008], [Shehata et al., 2014].

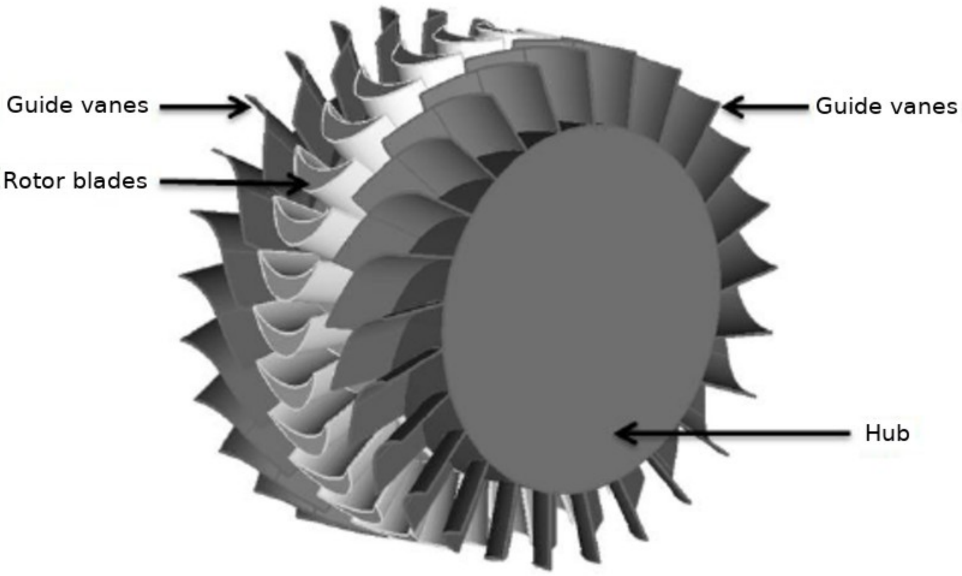

Fig. 3.5-4 An impulse turbine with guide vanes

Despite the large research effort, the largest obstacle to the commercial development of in OWCs consists in the high installation costs. In fact, considering the on-shore installation, it is required the construction of a reinforced concrete structure which constitutes up to 66% of the total costs. As a solution, it has been proposed to embed on-shore OWCs into breakwaters, in order to obtain a simple modular structure making use of the well-proven prefabrication technique of caissons. An example of this type of installation is the one operating in the port of Sakata [Takahashi et al., 1992] since 1989. In this way, the incidence of the cost due to the structure is drastically reduced, and the plant fulfil a dual purpose: to defend the stretch of water behind it and to produce electrical energy by means of generators connected to one or more turbines.

3.6 Breakwaters modelling and testing

In the aim of understand the performances of breakwaters which integrate OWC devices inside, it is necessary to explain the main characteristics of breakwaters themselves. Breakwaters are artificial constructs which reduce the intensity of the waves in the stretch of water where they are installed. These constructs allow to dissipate and to reflect seaward part of the energy owned by the waves. This leads to a lower fraction of energy transmitted to the shore, reducing the erosion of coastal areas or protecting harbours and other human installations. Breakwaters can be classified in emerged or submerged ones. The section of both generally assume simple geometries, for example rectangular and trapezoidal.

The first are not over-topping structures because waves rarely exceed them, depending on weather conditions. Therefore, the emerged breakwaters provide almost a total protection to the shoreline. However, the use of the emerged breakwaters is limited because of an important reason: the environmental impact. In fact, the emerged breakwaters reduce the recirculation of water toward the coast; as a result, the quality of water is worse. This problem is partially solved making breakwaters of a porous material, that ensure the transmission of water.

Instead, submerged breakwaters are over-topping structures, so the recirculation of water is always allowed. When waves impact a submerged structure, the energy is divided into three components: the reflected, the dissipated and the transmitted ones. The degree of protection of the structure is related to the amount of transmitted energy. If the submerged breakwater incorporates an absorption device, a further reduction of the amount of transmitted energy is ensured, increasing the protection performance of the breakwater.

Numerous experimental studies have analysed the protection properties of submerged breakwaters. Christou [Christou et al., 2008] studied the interaction between surface waves and a rectangular submerged barrier, asserting that the phenomenon of reflection of the non-linear incident waves is strictly linear. Losada [Losada et al., 1996] analysed the relationship between regular and irregular waves and the reflection coefficient in the case of submerged structures. He found that the value of the reflection coefficient calculated in the case of irregular waves is smaller than the one obtained in the case of regular waves. However, it resulted that the difference between these two values did not exceed 5%.

Several studies ([Huang and Chao, 1992], [Twu and Chieu, 2000]) have shown that the width of a permeable submerged breakwater is a fundamental variable in the design of the same, in terms of protection performance. Huang and Chao [Huang and Chao, 1992] found that the reflection coefficient decreases with the increasing of the porosity of a porous submerged structure. The energy dissipation increases with the increasing of the width and the number of the layers of the porous structure, which causes a reduction of reflection. Losada [Losada et al., 1996] has derived a critical value of the width of the structure, over which the reflection coefficient is not affected by the change of that size.

Stamos has studied the reflection of waves in the case of rigid and flexible structures [Stamos et al., 2002]. He claimed that the reflection coefficient increases with the increasing of rigidity of the barrier, regardless of the product between the number of wave, k, and water depth, h.

Among the many studies in the literature, a few methods allow for the parametrization of the reflection coefficient. Van der Meer [Van der Meer et al., 2005] in 2005 introduced a parametric calculation only for the case of reflection on porous structures (rubble-mound). In order to parametrize the reflection coefficient in the generic case of submerged breakwater, Young and Testik [Morgan and Testik, 2011] conducted experimental tests with vertical and semicircular barriers. It is observed that the reflection coefficient mainly depends on the ratio between the submergence of the structure, a and the height of incident wave, H_i. This allowed to obtain two semi-empirical parametric expressions of the reflection coefficient in the case of vertical and semicircular breakwater. For the same values of the ratio a/H_i, it was found that the rectangular structures reflects more energy than semicircular structures.

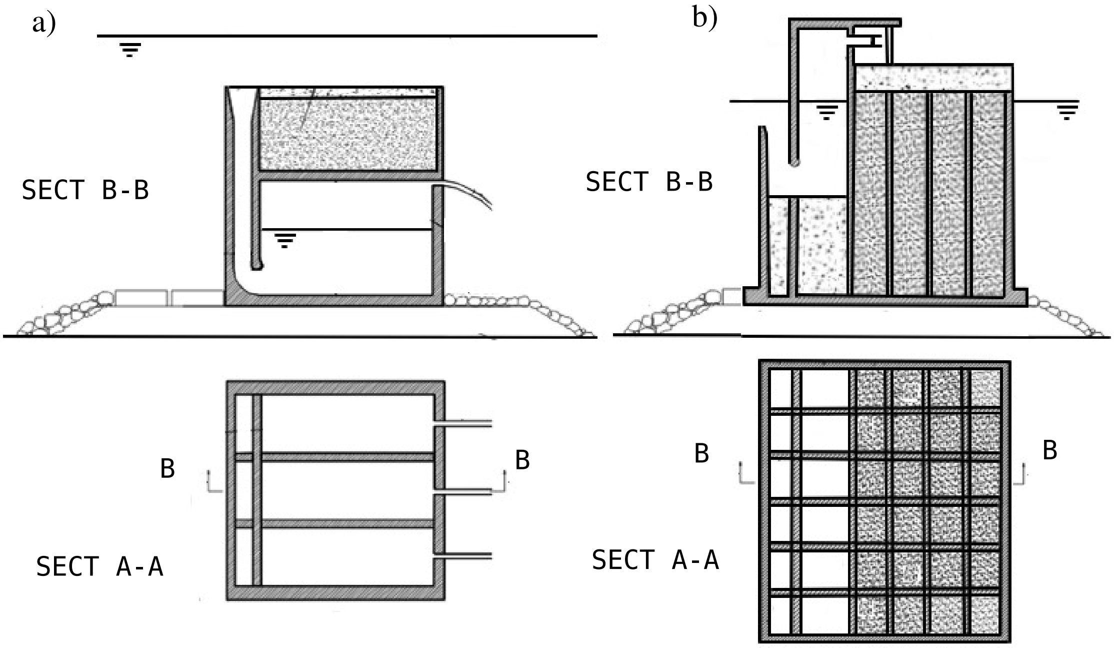

Fig. 3.7-1 The REWEC1, a), and the REWEC3, b)

From the analysis of the flow field upstream the breakwater, the reflection coefficient can be obtained by calculation methodologies that allow to separate the reflected waves from the incidents ones. These methods can be divided into two categories: methods operating in the time domain and methods operating in the frequency domain. Between the methods belonging to the second category, the most significant are the Goda & Suzuki method [Goda and Suzuki, 1976] and the Kittitanasuan method [Kittitanasuan and Goda, 1994].

3.7 The REWEC plants

In the aim of integrate OWC-type devices inside breakwaters, Boccotti patents the REWEC (Resonant Wave Energy Converter) [Boccotti, 1998] in two realizations. The first is the submerged device REWEC1 (Fig. 3.2-1a) and the second the emerged REWEC3 (Fig. 3.7-1b). A REWEC1 breakwater consists of several caissons placed close one to each other to form a submerged barrier. The well-proven prefabrication technique of caissons drastically reduce the incidence of the construction costs, and the REWEC1s fulfil a dual purpose: increase the performance of coastal protection of the breakwater by absorbing a part of the incident wave energy and produce electrical energy by means of a PTO-system. As we can see in fig. 3.7-2a, the REWEC1 is essentially a submerged caisson with a U-tube inside.

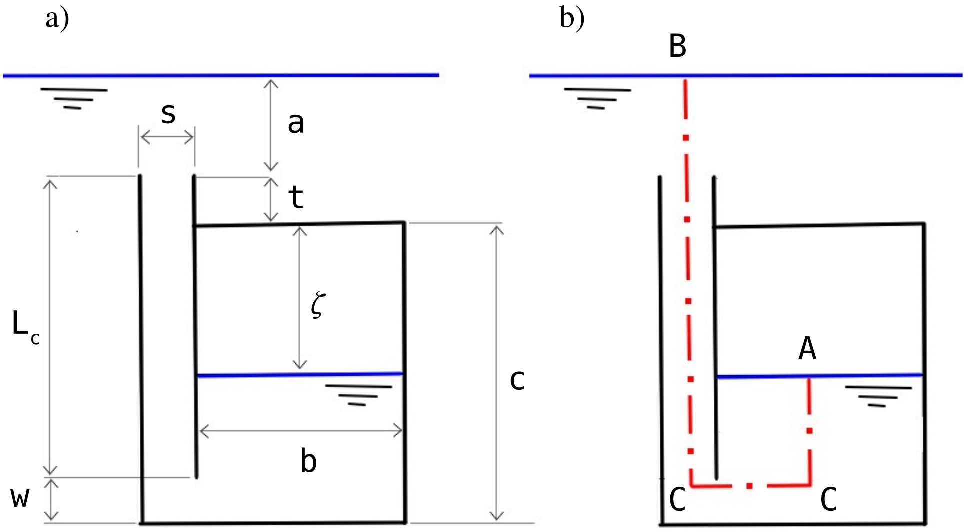

Fig. 3.7-2 REWEC1 geometrical parameters, a), and streamlines, b)

The first branch of the U-tube is a vertical duct connecting the sea water to a chamber that encloses a pressurized air volume. This pocket is generated by a compressor after the installation of the device, achieving a value of the air pressure that is the same of the hydrostatic pressure of the water under the pocket when sea is at rest. A low solidity Wells turbine [Torresi et al., 2004] can be placed as PTO-system in the vertical duct. When the wave crests passes above the vertical duct the pressure of the water inside the device increases, because of the growth of the hydrostatic load, raising the free water level inside the chamber and compressing the air pocket. Similarly, when the wave trough passes above the vertical duct, the free water level inside the chamber lets down decompressing the air pocket. This alternate compression and decompression of the air pocket generates an alternate inhalation and exhalation of water through the vertical duct, which drives the turbine.

In addition to the double purpose of coastal protection and energy production, another interesting aspect of the REWEC1 is the possibility of design it in order to reach resonance conditions with the incident waves. In fact, the device is essentially a U-tube (Fig. 3.7-2a) and the fluid-dynamic behaviour of the water can be correctly described along a streamline, which starts from the free water level inside the chamber (point A) and ends at the see free water level (point B) (Fig 3.7-2b).

Applying the generalized Bernoulli equation along this streamline, one obtains (Eq. 3.7-1):

$$\frac{1}{g}\int_A^B \frac{\delta u}{\delta t} ds = H_A - H_B - \sum H_W \qquad (3.7\text{-}1)$$

where H_A and H_B are the total heads in the points A and B, respectively, whilst ΣH_w is the sum of the head losses along the streamline. The left hand side of equation 3.7-1 is actually the integral of the Euler equation and, for the sake of simplicity, can be computed considering only the two vertical paths along the streamline, neglecting the contribution of the local inertia of the water below the bottom end of the duct. The first path goes from the air-water interface inside the chamber to the bottom opening of the vertical duct (C); the second goes from the aforesaid aperture to the top opening of the vertical duct. Hence, the integral can be rewritten as follows (Eq. 3.7-2):

$$\frac{1}{g}\int_A^B \frac{\delta u}{\delta t} ds = \frac{1}{g}\int_A^C \frac{\delta u}{\delta t} ds + \frac{1}{g}\int_C^B \frac{\delta u_w}{\delta t} ds \qquad (3.7\text{-}2)$$

where, in the first integral, u can be expressed as the derivative of the height, ζ, of the air pocket inside the chamber, whilst u_w is the velocity in the vertical duct. According to the continuity equation the velocity u_w can be written as a function of u as follows (Eq. 3.7-3):

$$u_w = \frac{b}{s}\frac{d\zeta}{dt} \qquad (3.7\text{-}3)$$

where b and s represent the cross sections of the chamber and the vertical duct, respectively (Fig.3.7-2a). In this model, we assume small values of the oscillations of ζ and a, with respect to the height of the air pocket in resting condition, ζ_0. According to this assumption, the values of ζ and a are always assumed to be equal to ζ_0 and a_0 when the geodetic heads are considered. Therefore the integration along the first and the second path gives (Eq. 3.7-4):

$$\frac{1}{g}\int_A^B \frac{\delta u}{\delta t} ds = \frac{1}{g}\left(c - w - \zeta_0\right)\frac{d^2\zeta}{dt^2} + \frac{1}{g}\left(\frac{b}{s}\right) L_c \frac{d^2\zeta}{dt^2} \qquad (3.7\text{-}4)$$

The total head, H_A, is related to the absolute pressure, p_A, of the air pocket inside the chamber, as follows (Eq. 3.7-5):

$$H_A = -\left(a_0 + t + \zeta_0\right) + \frac{p_A}{\rho g} + \frac{1}{2g}\left(\frac{d\zeta}{dt}\right)^2 \tag{3.7-5}$$

Assuming a polytropic law for the thermodynamic behaviour of the air inside the chamber, p_A can be evaluated as a function of the air volume, which is directly proportional to the height, ζ, of the air pocket (Eq. 3.7-6):

$$p_A = \left[p_{1,0} + \rho g\left(a_0 + t + \zeta_0\right)\right]\left(\frac{\zeta_0}{\zeta}\right)^m \tag{3.7-6}$$

where the subscript “0” refers to the resting condition (sea at rest) and m is the polytropic index. Actually, an isentropic law for the thermodynamic behaviour of air has been assumed ($m = 1.4$). The total head, H_B, is evaluated as follows (Eq. 3.7-7):

$$H_B = \frac{p_{1,0}}{\rho g} + \left(\frac{b}{s}\right)^2 \frac{1}{2g}\left(\frac{d\zeta}{dt}\right)^2 \tag{3.7-7}$$

The head losses, ΣH_w, can be estimated as the sum of the continuous friction losses, H_c, and the minor head losses in the vertical duct, H_d, whose general form is the following (Eq. 3.7-8):

$$H_{W,i} = \frac{1}{2g} k_i |u| u \tag{3.7-8}$$

where k_i can be assumed as the value of the coefficient of either the friction losses, k_c, or minor head losses, k_d. Therefore, the head losses are written as (Eq. 3.7-9):

$$\sum H_W = \frac{1}{2g}\left(\frac{b}{s}\right)^2 \left(k_c + k_d\right)\left|\frac{d\zeta}{dt}\right|\frac{d\zeta}{dt} \tag{3.7-9}$$

Substituting equations 3.7-5, 3.7-7, 3.7-9 in Eq. 3.7-1 leads to a non-linear second order differential equation (Eq. 3.7-10):

$$\begin{aligned} &\left[\left(c - w - \zeta_0\right) + \left(\frac{b}{s}\right) L_C\right]\frac{d^2\zeta}{dt^2} + \frac{1}{2}\left[\left(\frac{b}{s}\right)^2 - 1\right]\left(\frac{d\zeta}{dt}\right)^2 + \\ &\quad + \frac{1}{2}\left(\frac{b}{s}\right)^2 \left(k_c + k_d\right)\left|\frac{d\zeta}{dt}\right|\frac{d\zeta}{dt} + g\left(\zeta_0 + t + a_0\right) + \\ &\quad + \frac{p_{1,0}}{\rho} - \left[\frac{p_{1,0}}{\rho} + g\left(\zeta_0 + t + a_0\right)\right]\left(\frac{\zeta_0}{\zeta}\right)^m = 0 \end{aligned} \tag{3.7-10}$$

In order to obtain a simple solution of this problem, equation 3.7-10 needs to be linearised, in particular the terms associated to polytropic law inside the air pocket and the head losses. The linearised form of equation 3.7-10 becomes (Eq. 3.7-11):

$$A\frac{d^2\zeta}{dt^2}+B\frac{d\zeta}{dt}+C\zeta=0 \tag{3.7-11}$$

where (Eqs. 3.7-12, 3.7-13, 3.7-14):

$$A=\left(c-w-\zeta_0\right)+\left(\frac{b}{s}\right)L_C \tag{3.7-12}$$

$$B=\frac{\pi}{8g}\left(k_c+k_d\right)\left[\left(\frac{b}{s}\right)^2\omega\bar{\zeta}\right]+\frac{\pi}{8}\left[\left(\frac{b}{s}\right)^2-1\right]\omega\bar{\zeta} \tag{3.7-13}$$

$$C=\frac{m}{\zeta_0}\left[\frac{p_{1,0}}{\rho}+g\left(\zeta_0+t+a_0\right)\right] \tag{3.7-14}$$

$\bar{\zeta}$ is related to the amplitude of the ζ oscillations in the time domain. Equation 3.7-11 represents the equation of a damped harmonic oscillator. According to vibration theory, the undamped natural frequency of the system is then (Eq. 3.7-15):

$$f_n=\frac{1}{2\pi}\sqrt{\frac{C}{A}} \tag{3.7-15}$$

The value of the REWEC1 undamped natural frequency, f_n, depends on the value of the height of the air pocket under resting conditions, ζ_0, and on the values of both the vertical duct and the chamber cross section, s, and, b (Fig. 3.7-2a). In a REWEC1 the values of s and b are fixed, so it is convenient to set them in order to reach resonance with the most probable sea state. Instead, the value of ζ_0 can be modified varying the pressure inside the chamber by means of the compressor. In this way, the value of f_n can be modified in order to reach the resonance conditions with the fundamental frequency of the sea which is expected, for example, in a certain period of the year.

When a U-OWC device operates in resonance conditions, it achieves very large absorption of wave energy. In fact, it has been registered a maximum absorption rate equal to the 60% of the incident wave energy during the experiments carried out on a small-scale device placed in the natural laboratory of Reggio Calabria (Italy) [Camporeale and Filianoti, 2008].

REWEC3 plants are emerged, then the caissons can be integrated into pre-existing harbour defence breakwaters or new constructed ones. The air pocket is connected to the atmosphere through an air conduit, and in the air conduit is embedded the PTO system (i.e. a high solidity Wells turbine). Fig 3.7-3a reports a REWEC3 device schematics, with the geometrical parameters. Along with the parameters defined for the REWEC1 (see Fig. 3.7-2a) there are new ones: the air conduit length, L_a, and its diameter, D. Considering Fig. 3.7-3b, the fluid-dynamic behaviour of the water can be correctly described along a streamline, which starts from the free water level inside the chamber (point A) and ends at the opening of the vertical duct (point B) (Fig 3.7-3b). Applying the generalized Bernoulli equation along this streamline, one obtains (Eq. 3.7-16):

$$\frac{1}{g}\int_A^B \frac{\delta u}{\delta t} ds = H_A - H_B - \sum H_W \tag{3.7-16}$$

The integral in the left side of Eq. 3.7-16 can be substituted by the sum of the three integrals, each one of them refers to three different streamline parts, as reported in Fig. 3.7-3b. Hence, the integral can be rewritten as follows (Eq. 3.7-17):

$$\frac{1}{g}\int_A^B \frac{\delta u}{\delta t} ds = \frac{1}{g}\int_A^D \frac{\delta u_{A-D}}{\delta t} ds + \frac{1}{g}\int_D^C \frac{\delta u_{D-C}}{\delta t} ds + \frac{1}{g}\int_C^B \frac{\delta u_w}{\delta t} ds \tag{3.7-17}$$

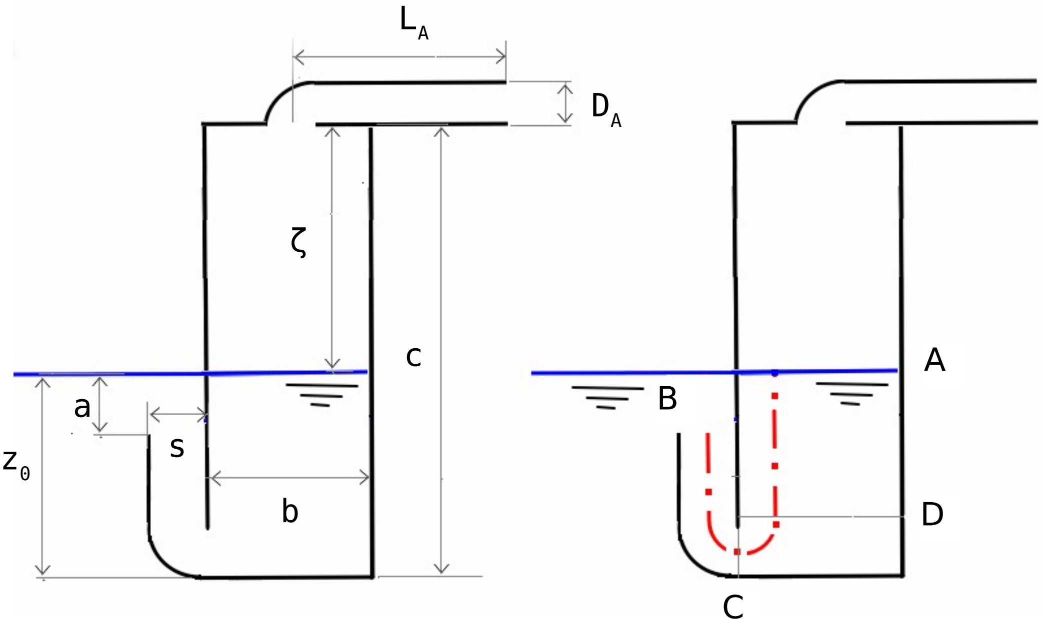

Fig. 3.7-3 REWEC1 geometrical parameters, a), and streamlines, b)

The geometrical characteristics of the three streamlines considered are reported in the table below:

A-D:	length: $L_{A-D} = z_0 - s$	width: $A_{A-D} = b$
D-C:	length: $L_{D-C} = \frac{\pi}{4} s$	width: $A_{D-C} = (b+s)/2$

C-B:	length: $L_{C-B}=z_0-a-s+\frac{\pi}{4}s$	width: $A_{C-B}=s$

The streamlines A-D and C-B have a constant width, whilst the D-C one is supposed to have a constant width equal to the average between s and b. In accordance with the continuity equation, the water flow velocity along the D-C e C-B streamline parts are, respectively (Eq. 3.7-18):

$$u_{A-D}=\frac{d\zeta}{dt},\ u_{D-C}=\frac{b}{(b+s/2)}\frac{d\zeta}{dt} \tag{3.7-18}$$

For u_w is valid the same equation reported in Eq. 3.7-3. Eq. 3.7-17 can be rewritten as follow (Eq. 3.7-19):

$$\frac{1}{g}\int_A^B\frac{\delta u}{\delta t}ds=\frac{1}{g}\left(L_{A-D}+L_{D-C}\frac{b}{(b+s)/2}+L_{C-B}\frac{b}{s}\right)\frac{d^2\zeta}{dt^2} \tag{3.7-19}$$

The term H_A in Eq. 3.7-16 can be written as (Eq. 3.7-20):

$$H_A=z_A+\frac{p_A}{\rho_w}+\frac{u_{A-D}^2}{2}=\frac{p_A}{\rho_w}+\frac{1}{2}\left(\frac{d\zeta}{dt}\right)^2 \tag{3.7-20}$$

The value of the pressure inside the chamber, p_A, can be derived from the calculation of the total head variation inside the air conduit, ΔH_a. The air compressibility inside the chamber can be neglected in comparison to the pressure losses due to the operation of the air turbine. Then, the value of p_A at the entrance of the air channel is the same that we have at the free water surface inside the chamber. Applying the Bernoulli's equation for an inviscid and unsteady flow, between the ends of the air conduit, we have (Eq. 3.7-21):

$$\Delta H_a=\frac{1}{\rho_a g}(p_A-p_{atm})+\frac{1}{g}L_a\frac{du_a}{dt} \tag{3.7-21}$$

Where p_{atm} is the atmospheric pressure and u_a is the air velocity inside the air conduit, its value is assumed to be positive in the occurrence of air outflow.

From the continuity equation, we can write u_a as (Eq. 3.7-22):

$$u_a=-\frac{4b}{\pi D_a^2}\frac{d\zeta}{dt} \tag{3.7-22}$$

The total head variation inside the air conduit, ΔH_a, can be written also as the sum of the losses contribution, due to friction, minor head losses and turbine operation. The first two can be written starting from the general form reported in Eq. 3.7-8. The turbine losses, ΔH_t, are (Eq. 3.7-23):

$$\Delta H_t = -\left(\frac{1}{2g} U_{tip} B_t \frac{b}{A_t}\right)\frac{d\zeta}{dt} = -F_t \frac{d\zeta}{dt} \qquad (3.7\text{-}23)$$

Where U_{tip} is the turbine blade tip velocity, B_t is the turbine damping ratio and A_t is the turbine cross section. Then, the equation for the calculation of ΔH_a is (3.7-24):

$$\Delta H_a = -\frac{1}{2g}\left(k_{c,a} - k_{d,a}\right)\frac{4b}{\pi D_a^2}\left|\frac{d\zeta}{dt}\right|\frac{d\zeta}{dt} - \frac{1}{2} U_{tip} B_t \frac{b}{A_t}\frac{d\zeta}{dt} \qquad (3.7\text{-}24)$$

The formulation of ΔH_a deriving from Eq. 3.7-24 can be substituted in Eq. 3.7-21 in order to obtain p_A. Then, p_A can be substituted in Eq. 3.7-20, in order to write H_A as a function of ζ. Following the same procedure adopted in the REWEC1 analysis, the prevalence term at the duct mouth, H_B is (Eq. 3.7-25):

$$H_B = z_B + \frac{p_B}{\rho_w g} + \frac{v_B^2}{2g} = \frac{p_{atm}}{\rho_w g} + \frac{1}{2g}\left(\frac{b}{s}\right)^2\left(\frac{d\zeta}{dt}\right)^2 \qquad (3.7\text{-}25)$$

Considering the water flow from A to B and neglecting the losses in A-D and D-C, the sum of the friction and minor head losses can be written as (Eq. 3.7-26):

$$\sum H_W = \frac{1}{2g}\left(\frac{b}{s}\right)^2\left(k_{c,w} + k_{d,w}\right)\left|\frac{d\zeta}{dt}\right|\frac{d\zeta}{dt} \qquad (3.7\text{-}26)$$

Substituting equations 3.7-20, 3.7-25, 3.7-26 in Eq. 3.7-16 leads to a non-linear second order differential equation. In order to obtain a simple solution of this problem, this equation needs to be linearised. The linearised form (Eq. 3.7-27):

$$A\frac{d^2\zeta}{dt^2} + B\frac{d\zeta}{dt} + C\zeta = 0 \qquad (3.7\text{-}27)$$

where (Eqs. 3.7-28, 3.7-29, 3.7-30):

$$A = L_{A-D} + L_{D-C}\frac{b}{(b+s)/2} + L_{C-B}\frac{b}{s} + L_a\frac{\rho_a}{\rho_w}\frac{4b}{\pi D_a^2} \qquad (3.7\text{-}28)$$

$$\begin{aligned} B = {} & \frac{\pi}{8g}\left(k_{c,w} + k_{d,w}\right)\left[\left(\frac{b}{s}\right)^2 \omega\bar{\zeta}\right] + \frac{\pi}{8}\left[\left(\frac{b}{s}\right)^2 - 1\right]\omega\bar{\zeta} + \\ & -\frac{\pi}{8g}\left(k_{c,a} + k_{d,a}\right)\left[\left(\frac{4b}{\pi D_a^2}\right)^2 \omega\bar{\zeta}\right] + \frac{\pi}{8}\left[\left(\frac{4b}{\pi D_a^2}\right)^2 - 1\right]\omega\bar{\zeta} - F_t \end{aligned} \qquad (3.7\text{-}29)$$

$$C = g \qquad (3.7\text{-}30)$$

$\bar{\zeta}$ is related to the amplitude of the ζ oscillations in the time domain. Equation 3.7-27 represents the equation of a damped harmonic oscillator. As in the case of the REWEC1, the undamped natural frequency of the system is (Eq. 3.7-31):

$$f_n=\frac{1}{2\pi}\sqrt{\frac{C}{A}} \tag{3.7-31}$$

4. CFD models and settings for the simulation of REWEC devices

4.1 Modelling a multiphase flow

Considering the presence of two different fluid, air and water, inside both REWEC1 and REWEC3, CFD modelling starts with the definition of the method to be used to simulate a multiphase flow. There are two different approaches to the numerical solution of a multiphase flow: the Eulerian-Lagrangian [Subramaniam, 2013] and the Eulerian-Eulerian [Harlow and Amsden, 1975]. The first has been developed to solve the case of one or more phases, that are the secondary phases, dispersed as particles or bubbles into the primary phase. The second is used in the case of two immiscible phases, that are separated by a wide and the defined surface. This is the case of the simulation of the water-air interaction, that is on the basis of the present work.

In accordance with the Eulerian-Eulerian approach, at each cell of the numerical domain are associated a number of Volume Fractions, one for each phases. A Volume Fraction represents the ratio between the cell volume occupated by a phase and the overall cell volume. Since we are considering immiscible phases, the sum of all the Volume Fraction is always equal to one in each cell of the domain. In the Ansys Fluent code, the Volume Of Fluid (VOF) model is a Eulerian-Eulerian multiphase model that leads to an accurate definition of the interface between immiscible fluids.

The VOF model solves a Volume Fraction continuity equation into each cell of the numerical domain. If we consider the *q* phase, with *n* the number of all phases inside the domain, the Volume Fraction equation for this phase is (Eq. 4.1-1):

$$\frac{1}{\rho_q}\left[\frac{\partial\left(\alpha_q\rho_q\right)}{\partial t}+\nabla\cdot\alpha_q\rho_q\vec{v_q}=S_{\alpha_q}+\sum_{p=1}^{n}\left(\dot{m}_{pq}-\dot{m}_{qp}\right)\right] \tag{4.1-1}$$

where ρ_q is the *q* phase density, $\vec{v}_q$ is the velocity vector in the cell and $\dot{m}_{pq}$, $\dot{m}_{qp}$ the mass exchanges between the *q* phase and the others phases and vice versa. $S_{\alpha q}$ is a source term, that is equal to zero by default. The Volume Fraction equation is solved for each phase except the primary phase, the Volume Fraction value of which derives from the calculated other phases ones. Then, named α_q the Volume Fraction of a phase, the value of the primary phase Volume Fraction will satisfy the no-penetrable conditions of the phases (Eq. 4.1-2):

$$\sum_{q=1}^{n}\alpha_q=1 \tag{4.1-2}$$

Eq. 4.1-1 is a partial differential equation that is solved by substituting the partial derivatives with discretized forms, in accordance with the Finite Volume approach. Once discretized, the Volume Fraction equation can be solved by means of both explicit or implicit methods.

In the explicit method, the Volume Fraction values at the current simulation time step, *n+1*, are evaluated from the former time step values, *n*. Then, the discretized form of Eq. 4.1-1 will be (Eq. 4.1-3):

$$\frac{\alpha_q^{n+1}\rho_q^{n+1}-\alpha_q^{n}\rho_q^{n}}{\Delta\tau}V+\sum_f \rho_q^n U_f^n \alpha_{q,f}^n=\left[\sum_{\rho=1}^{n}\left(\dot{m}_{pq}-\dot{m}_{qp}\right)+S_{\alpha_q}\right]V \qquad (4.1\text{-}3)$$

Where the subscript *f* refers to the *f* face of a numerical domain cell, U^n_f is the volumetric flow rate through the *f* face at the time *n* and *V* is the cell volume.

The Volume Fraction equation is discretized over a time step, Δτ, that is generally different in respect to the time step, Δt, of the simulation. The Δτ is automatically calculated from the Courant Number, $N_{Courant}$, value near the fluids interface. $N_{Courant}$ is a dimensionless parameter equal to the ratio between Δτ and the minimum time that fluids need to pass trough a cell near the fluids interface (Eq. 4.1-4):

$$N_{Courant}=\frac{\Delta\tau}{\Delta x_{cell}/v_{fluid}} \qquad (4.1\text{-}4)$$

When the value of the ratio between Δt and Δτ is high (it is appropriate to not exceed 1000) the computational effort increases and the solution is less stable. Then, when the explicit VOF model is used, the simulation time step, Δt, has to be set in accordance with the parameters from which Δτ depends. Namely, these parameters are the Courant Number, the minimum cell dimension and the maximum flow velocity near the fluids interface. Indeed, if Δt is much bigger than Δτ, the Δτ value automatically increases. Then, also the Courant Number value grows, and the simulation stops if it exceed the value of 250.

In the explicit model, both the Volume Fraction and the other flow properties near the interface, at n+1 and n time step, are calculated concurrently. The discretized Volume Fraction equation is (Eq. 4.1-5):

$$\frac{\alpha_q^{n+1}\rho_q^{n+1}-\alpha_q^{n}\rho_q^{n}}{\Delta\tau}V+\sum_f \rho_q^{n+1} U_f^{n+1} \alpha_{q,f}^{n+1}=\left[\sum_{\rho=1}^{n}\left(\dot{m}_{pq}-\dot{m}_{qp}\right)+S_{\alpha_q}\right]V \qquad (4.1\text{-}5)$$

The Volume Fraction value at the current time step, n+1, is calculated by an iterative solution. Then, a scalar transport equation, with the Volume Fraction as variable, is solved at each simulation time step. This equation adds to the equations solved at each time step regarding the others flow properties, increasing the computational effort in comparison to the explicit method.

The time step, Δτ, of the Volume Fraction equation not depends on the Courant Number value, that in this case is not an input of the multiphase flow simulation. Then, when the implicit method is used, there are not limitations on the simulation time step size, Δt, due to the Courant Number. Due to its solution scheme, the implicit method leads to good simulation result in the case of steady multiphase flows, whilst explicit method is recommend for the simulation of unsteady flows.

Once the Volume Fraction values have been calculated for all the cells faces, interpolation schemes are used in order to draw the interface surface in cells having two or more phases inside. For both explicit and implicit VOF methods, two different interpolation schemes have been developed:

- ***Geometric-Reconstruction scheme***
- ***Donor-Acceptor scheme***

As shown in Fig. 4.1-1 the Geometric-Reconstruction leads to a interface tracking that is closer to the real shape in comparison to the Donor-Acceptor scheme. In the Geometric-Reconstruction approach, the standard interpolation schemes that are used Fluent are used to obtain the face fluxes whenever a cell is completely filled with one phase or another. When the cell is near the interface between two phases, the Geometric-Reconstruction scheme is used.

The Geometric-Reconstruction scheme represents the interface between fluids using a piecewise-linear approach. In Fluent this scheme is the most accurate and is applicable for general unstructured meshes. The geometric reconstruction scheme is generalized for unstructured meshes from the work of Youngs [Youngs D.L., 1982]. It assumes that the interface between two fluids has a linear slope within each cell, and uses this linear shape for calculation of the advection of fluid through the cell faces.

The first step in this reconstruction scheme is calculating the position of the linear interface relative to the center of each partially-filled cell, based on information about the volume fraction and its derivatives in the cell. The second step is calculating the advecting amount of fluid through each face using the computed linear interface representation and information about the normal and tangential velocity distribution on the face. The third step is calculating the volume fraction in each cell using the balance of fluxes calculated during the previous step.

In the donor-acceptor approach, the standard interpolation schemes that are used in FLUENT are used to obtain the face fluxes whenever a cell is completely filled with one phase or another. When the cell is near the interface between two phases, a "donor-acceptor" scheme is used to determine the amount of fluid advected through the face [Holmes D.G. and Connell S.D., 1989]. This scheme identifies one cell as a donor of an amount of fluid from one phase and another (neighbour) cell as the acceptor of that same amount of fluid, and is used to prevent numerical diffusion at the interface.

The amount of fluid from one phase that can be convected across a cell boundary is limited by the minimum of two values: the filled volume in the donor cell or the free volume in the acceptor cell. The orientation of the interface is also used in determining the face fluxes. The interface orientation is either horizontal or vertical, depending on the direction of the volume fraction gradient of the phase within the cell, and that of the neighbour cell that shares the face in question. Depending on the interface's orientation as well as its motion, flux values are obtained by pure up-winding, pure down-winding, or some combination of the two.

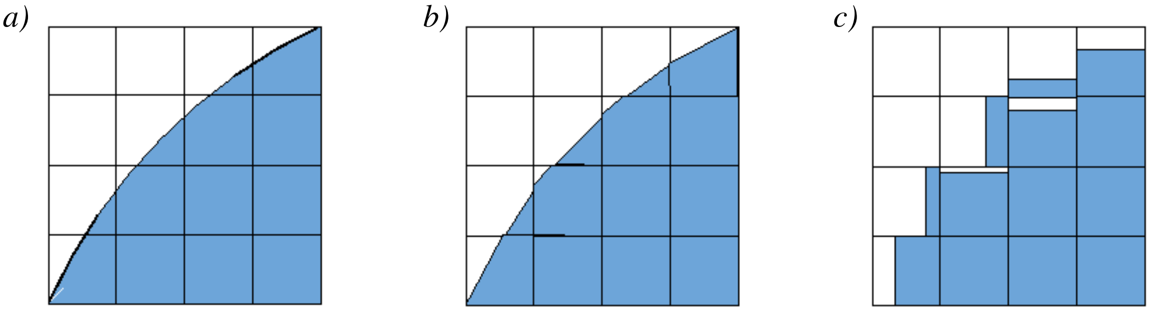

Fig 4.1-1 Interface tracking with the Geometric-Reconstruction scheme, b), and with the Donor-Acceptor scheme, c), in comparison to the actual interface shape, a)

4.2 Solver typologies

All the simulation have been carried by means of the Fluent solver, that provides for the numerical solution of the differential equations that govern the flow by means of the finite volume discretization method. In the simulation of the operation of REWEC plants, the equations to be discretized and numerically solved are the continuity, momentum, volume fraction and energy ones. Even if the thermal exchanges are negligible, as in the case of REWECs, the solution of the energy equation is still necessary in order to be able to know the thermodynamic status variables of the air, which will be assumed as an ideal compressible gas.

In Fluent there are two different methodologies to solve the flow equation system:

- ***Pressure Based solver***
- ***Density Based solver***

In both solvers flow velocity is calculated from the solution of the momentum equation. According to the Pressure Based solver, the pressure field is obtained directly from an appropriate formulation of the continuity equation; whilst in the case of the Density-Based approach the continuity equation is used to obtain the density field and the pressure is obtained successively from the equation of state.

This derives from the fact that the Pressure-Based model was developed for the resolution of incompressible flows, whilst the Density-Based model for compressible ones. Both models have been extended and reformulated in the years in order to be adopted for both types of flow. However, the Pressure-Based model is the only model available for the resolution of a multiphase flow, it has been adopted for the carried out simulations.

A finite volume solver needs a numerical grid, that is a discretization of the simulation domain. The solution process on the numerical grid is essentially divided in two phases:

- Integration of the flow equations in each control volume of the calculation grid (cell), in order to construct the system of discretized equations;

- Linearisation of the discretized equations and solution of the resulting linear system through an iterative cycle, in order to update the values of the dependent variables at each time step of the simulation.

The integration phase leads to a space discretization of the equations. At this stage, the solver adopts numeric interpolation techniques to obtain values along the faces of cells, starting from the centers ones. In the case of unsteady flows, further temporal discretization is needed for the temporal derivatives of variables. The process of equations integration is, then, characterized by both spatial and temporal discretization schemes. These schemes will be described in the next sections.

4.3 Spatial discretization schemes

The finite volumes approach is based on the integration of differential equations in each control volume of the numerical grid, providing discrete equations to the conservation laws of the scalar quantities. Considering the transport equation of a generic scalar quantity, φ, the discrete equation form written on an arbitrary control volume, *V*, is:

$$\int_V \frac{\partial \rho \phi}{\partial t} dV + \oint \rho \phi \vec{v}\, d\vec{A} = \oint \Gamma_\phi \nabla \phi \cdot d\vec{A} + \int_V S_\phi dV \qquad (4.3\text{-}1)$$

Where ρ is the density, *v* the velocity vector, *A* the surface area vector and S_φ the source term per unit of volume. This discrete equation is integrated into each control volume, that is each cell in the computing domain. The result of the integration is as follows:

$$\frac{\partial \rho \phi}{\partial t} V + \sum_f^N \rho_f \vec{v}_f \phi_f \cdot \vec{A}_f = \sum_f^N \Gamma_\phi \nabla \phi_f \cdot \vec{A}_f + S_\phi V \qquad (4.3\text{-}2)$$

The subscript *f* indicates that the quantity value refers to one of the total faces, *N*, which surround the control volume. Fluent solver stores the values of φ in the center of the cells of the computational domain by default. However, the convective term of the integrated equation is calculated starting from the values of φ on the faces of the cell, φ_f, which must therefore be obtained starting from the values on the center through appropriate interpolation schemes (for example upwind schemes). The upwind schemes allow to derive the value of φ_f from the quantities present in the upstream cells, considering the velocity direction, v_n, normal to the considered face.

Fluent allows you to choose between four different schemes: first order upwind, second order upwind, power-law and QUICK.

When the accuracy of the upwind scheme is at the first order, the value of the generic quantity φ on the faces of a cell is calculated starting from the assumption that the value at the center of the cell is the average value of the quantity over the whole cell. Therefore, using the first upwind scheme, the value of the quantity φ_f on the face of a cell is considered equal to the value of the quantity, φ_u, at the center of the cell immediately upstream.

In the second order upwind scheme, instead, the value of φ_f is equal to the sum of φ_u added to the scalar product between the gradient of φ_u and the vector distance between the centers of the two cells considered:

$$\phi_f = \phi_u + \nabla \phi_u \cdot \vec{r} \tag{4.3-3}$$

The first order upwind scheme is more stable than the second order one when the explicit VOF multiphase model is used.

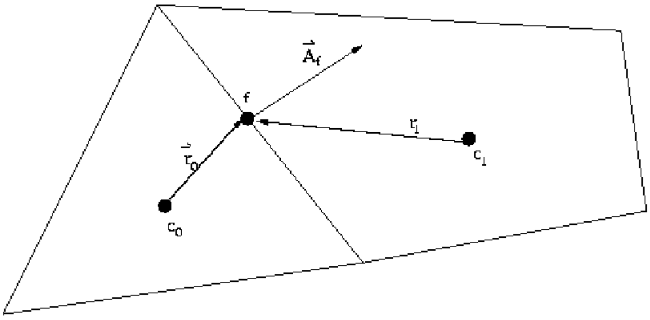

Fig 4.3-1 Scheme for the reconstruction of gradients on the face of a cell starting from the quantity values at the center of the adjacent face

4.4 Gradient Reconstruction methods

To obtain the value of a scalar quantity gradient in a given cell, two different models can be used, both based on the Green-Gauss theorem. Applying the Green-Gauss theorem, the gradient of a scalar quantity φ in the center of a cell is calculated as:

$$\nabla \phi = \frac{1}{V} \sum_f \bar{\phi}_f \vec{A}_f \tag{4.4-1}$$

where A_f is the face area.

The first gradient reconstruction method is the Green-Gauss cell-based method, in which the face value, φ_f, is calculated as the average of the values in the center of the nearby cells:

$$\bar{\phi}_f = \frac{\phi + \phi_{nearby}}{2} \tag{4.4-2}$$

The second method is the Green-Gauss nodes based, in which the value is calculated as the average of the values on the faces nodes:

$$\bar{\phi}_f = \frac{1}{N_f} \sum_{n}^{N_f} \bar{\phi}_n \tag{4.4-3}$$

where N_f is the number of faces nodes and φ_n is the value at node n. In turn, the φ_n values are calculated as the weighted averages of the values at the cells surrounding the node. This second method is mainly used for triangular or tetrahedral cell grids.

As it will be described in the next sections, the simulations have been carried out on structured meshes. Then, the Green-Gauss cells-based method was used, that is also the default method for the Pressure Based solver.

4.5 Time discretization methods

Considering an unsteady flow, the time derivative of a generic scalar quantity, φ, is not null and must be discretized temporally on the time step of the simulation, Δt. The time discretization method is based on the finite differences approach, which can be accurate first or second order. The first order discretized form will be:

$$\frac{\partial \phi}{\partial t} = \frac{\phi^{n+1} - \phi^{n}}{\Delta t} \tag{4.5-1}$$

whilst the second order discretized form is:

$$\frac{\partial \phi}{\partial t} = \frac{3\,\phi^{n+1} - 4\,\phi^{n} + \phi^{n+1}}{2\Delta t} \tag{4.5-2}$$

When the computing domain has deformed areas, as in the case of deforming meshes, it is suggested to use first order temporal discretization schemes in order to improve the solution stability.

Finally, in the transport equation of φ, the discretized form equals other terms that are functions of the quantity φ, as reported in Eq. 4.5-3. In the case of timing discretization at the first order:

$$\frac{\phi^{n+1} - \phi^{n}}{\Delta t} = F(\phi) \tag{4.5-3}$$

Depending on whether the value of φ in $F(\varphi)$ is the one calculated at the current time step, $n+1$, or at the previous time step, n, the temporal discretization model will be implicit or explicit respectively.

When adopting the Pressure Based solver, only the implicit model can be used. The value of φ at $n + 1$ is obtained by solving the following implicit equation:

$$\phi^{n+1}=\phi^{n}+\Delta t\, F\left(\phi^{n+1}\right) \tag{4.5-4}$$

As implicit, this equation must be resolved iteratively before be passed to the next time step. The implicit discretization method is more costly from the computational point of view but has the advantage of being stable over any size of the time step, unlike the explicit model for which a small size time step is recommended.

4.6 Equations linearisation and solution schemes

The Pressure-Based Solution Model presents two different methods of linearisation and solution of discrete non-linear equations:

- Sequential Calculation Method (Segregated)
- Coupled Calculation Method

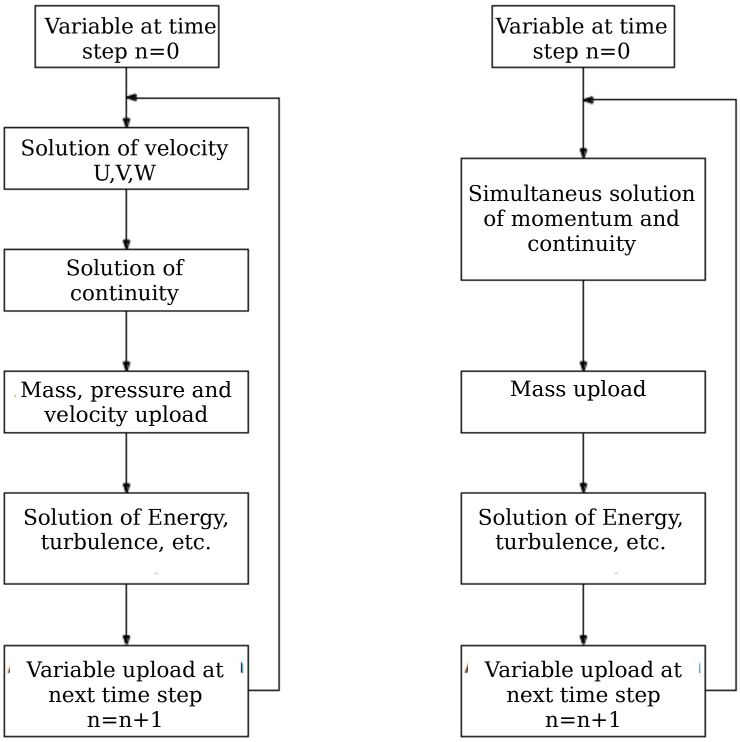

Fig 4.6-1 Segregated and Coupled Calculation Schemes Algorithms

The solution procedure of both methods is showed in flow diagrams in Figure 4.6-1. Both discrete and non-linear equations of continuity and momentum presents both pressure and velocity as variables, so the solution process of these equations must start from a method of decoupling variables in the two equations. In accordance with the Segregated method, all discrete equations, and therefore also those of continuity and momentum, are solved separately and sequentially. Whilst, in the Coupled method the continuity and momentum equations are solved simultaneously but in a separate and sequential manner with respect to the other equations, as well as in the Segregated method.

The Segregated method is more efficient in the use of the computer memory, since equations are stored one at a time. However, the convergence of the solution is relatively slow due to the fact that the equations are solved decoupled by introducing a breakdown error.

On the contrary, since in the Coupled method the equations of continuity and momentum are solved together, the breakdown error is not introduced. Then, the converging solution improves. However, the memory requirement increases, since both continuity and momentum equations must be loaded into memory simultaneously in order to solve the pressure and velocity field. The Coupled method is preferably used in the case of compressible high speed flows or having high rotational or floating forces, and in the case of very fine grids.

In the simulations carried out, the Pressure-Based Segregated solver model was adopted, considering the relatively low flows speeds and rotational and floating forces.

4.7 Under relaxation factors

An under relaxation factors defines the correction fraction to be made on the previous value of an equation variable, before the next iteration. If we indicate with φ the current value of the variable, we have that this is equal to:

$$\phi = \phi_{old} + \alpha \Delta \phi \qquad (4.7\text{-}1)$$

Where α is the under relaxation factor and $\Delta\varphi$ the correction to add to the previous value φ_{old}.

In the cases under consideration, a Pressure-Based Pressure Solver was adopted, in which each resolved equation has a sub-zero factor associated with it. To reduce the possible tendency of the equation system to vary, it is appropriate to reduce the value of the sub-silence factors for the individual equations, with respect to the default values, so that the correction is not applied entirely but only of the fraction indicated by the sub-zero factor .

4.8 Use of the dynamic mesh tool for simulate a Wave-maker

In both simulations of REWEC1 and REWEC3 breakwaters under incident waves, the wave motion has been generated by a moving wall into the numerical domain. The moving wall acted as a piston-type wave-maker, characterized by a stroke and an oscillation period. The oscillation period of the moving wall has been the same of the generated waves, whilst the stroke has been derived in accordance with the theory proposed by Galvin (1964) for the study of the generation of waves by means of a piston-type wave-maker [O'Dea and Newman, 2007]. The calculation starts from the consideration that the volume of water displaced by the wave-maker must be equal to the volume of the crest of the propagated wave (see Fig. 4.8-1). If the piston stroke is S and h is the water level inside the thank, the volume of water displaced by the piston over a period of oscillation will be equal to Sh. The volume of water under the generated wave crest is:

$$\int_0^{L/2}\left(\frac{H}{2}\right)\sin k\,x\,dx=\frac{H}{k} \tag{4.8-1}$$

where k indicates the wave number. Equating the two volumes we have that:

$$Sh=\frac{H}{k}=\frac{H}{2}\left(\frac{L}{2}\right)\cdot\frac{2}{\pi} \tag{4.8-2}$$

where $2/\pi$ represents the ratio between the shaded area subtended by the crest of the wave on the rectangular area that contains it (Fig. 4.8-1).

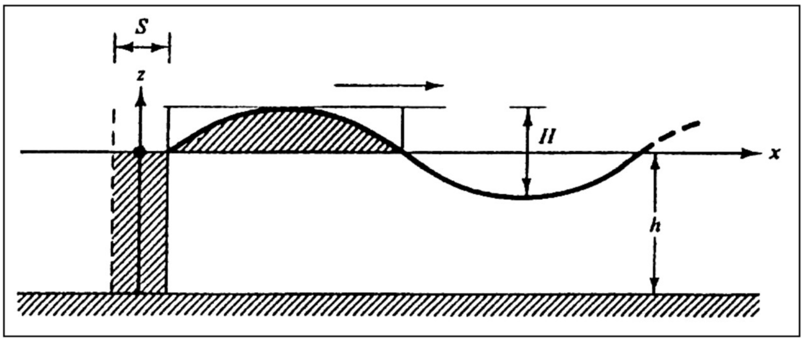

Fig. 4.8-1 Volume of water displaced in a piston stroke

Equation 4.8-2 can also be written as:

$$\frac{H}{S}=kh \tag{4.8-3}$$

where H/S indicates the ratio between the wave height and the stroke of the piston. Then, the value of the moving wall stroke is derived, depending on the wave height to be generated.

The dynamic mesh feature has been used for both the moving wall and the neighbouring deforming mesh of the numerical domains containing a moving wall. The dynamic mesh model can be used when the form of the numerical domain changes over time due to the movement of one or more domain contours. The contours can move in accordance to a given velocity law or as a consequence of flow forces that act on it. In the simulations carried out, the velocity law of the contour acting as a piston is known beforehand, and the movement of the same is defined by the velocity returned by an User Defined Function (UDF).

Since the computing domain will present moving contours and other fixed over time, there will be grid areas whose cells will deform. When setting a dynamic mesh in Fluent, it must be specified the moving contour/s, indicating how the motion is handled, and the grid zones that will deform.

When a dynamic mesh model is used, the integral form of the conservation equation for a scalar, φ, in an arbitrary control volume that has moving margins, V, can be written as follows:

$$\frac{d}{dt}\int_V \rho\phi dV + \int_{\partial V} \rho\phi(\vec{u}-\vec{u}_g)\cdot d\vec{A} = \int_{\partial V} \Gamma_\phi \nabla\phi\cdot d\vec{A} + \int_V S_\phi dV \tag{4.8-4}$$

Unlike the case of a cell that does not deform, the velocity vector in the convective term is the vector difference between the flow vector velocity, v, and the velocity vector of the dynamic mesh, v_g.

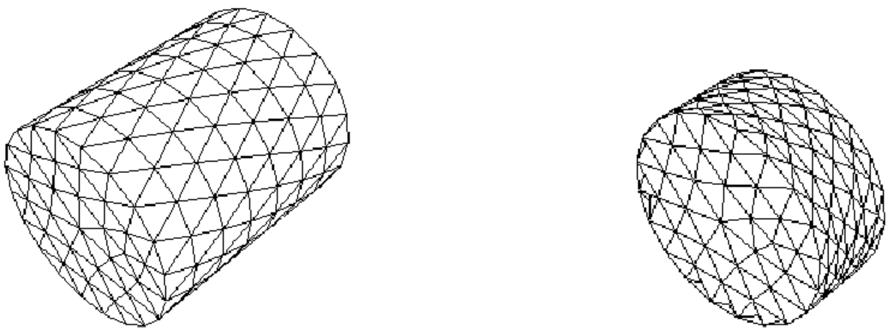

Fig 4.8-2 Example of elastic smoothing applied to a cylinder in the compression phase

The temporal discretization of the first term of the equation involves the calculation of the cell volume at instant $n + 1$:

$$\frac{d}{\partial t}\int_V \rho\phi dV = \frac{(\rho\phi V)^{n+1}-(\rho\phi V)^n}{\Delta t} \tag{4.8-5}$$

in which:

$$V^{n+1} = V^n + \frac{dV}{dt}\Delta t \tag{4.8-6}$$

The time derivative of V is calculated from the continuity equation on the cell:

$$\frac{dV}{dt} = \int_{\partial V} \vec{u}_g \cdot d\vec{A} = \sum_j^{N_f} \vec{u}_{g,j}\cdot \vec{A}_j \tag{4.8-7}$$

wherein N_f is the number of faces delimiting the control volume, whilst the vector, A_j, corresponds to the area of the j-th face. The scalar product is calculated as:

$$\vec{u}_{g,j} \cdot \vec{A}_j = \frac{\delta V_j}{\Delta t} \tag{4.8-8}$$

where the derivative represents the volume part moved to the time step Δt.

The mesh volume updating is automatically managed by Fluent at each time step, based on the position of the grid contours, using one of the three possible methods available:

- Elastic smoothing method
- Layering method
- Re-meshing method

The elastic smoothing method will then be analysed since it is the only method for updating the grid used in the simulations carried out.

The elastic smoothing method considers the edges that are in the grid area which is subject to deformation as a network of interconnected springs. The initial distance between the edges before each movement at the boundary represents the equilibrium condition of the mesh. When the nodes belonging to the boundary to which the motion is imposed begin to move, a force of an elastic nature will be generated and transmitted to all the edges that intersect in those nodes. According to the law of Hook, the total force that a single moving node transmits to the n-th junctions located at the other end of the edges which intersect in the node *i* is as follows:

$$\vec{F}_i = \sum_j^{n_i} k_{ij} (\Delta \vec{x}_j - \Delta \vec{x}_i) \tag{4.8-9}$$

Where Δx_j and Δx_i are respectively the displacements of a node j-th and of the node i, n_j is the total number of nodes of the edges that intersect in *i* and k_{ij} is the elastic constant of the edge connecting the node *i* to the node *j*, thus defined:

$$k_{ij} = \frac{1}{\sqrt{|x_i - x_j|}} \tag{4.8-10}$$

For the balance of forces, the force on a node due to all connected sides must be zero.
Starting from this condition we build the following iterative update:

$$\Delta x_i^{m+1} = \frac{\sum_j^{n_i} k_{ij} \Delta x_j^m}{\sum_j^{n_i} k_{ij}} \tag{4.8-11}$$

Since the displacements of the nodes that move with the rigid body are known, it is possible to find the displacement of all the internal nodes by solving the iterative process with the Jacobi method. Called $\Delta x_i^{m,conv}$ the displacement value for which the iterative process converges, the position of the node *i* at the time step *n + 1* will be calculated as a function of the position at the previous time step n according to the expression:

$$x_i^{n+1}=x_i^n+\Delta x_i^{m,conv} \tag{4.8-12}$$

The elastic smoothing updating method can be applied to mesh having quadrangular cells (in the two-dimensional case) if the motion of the moving contour occurs mainly in one direction. Therefore, considering the occurrence of this condition, in all the test cases carried out, the elastic smoothing method was used as a method for updating the grid.

It should be noted, however, that the elastic smoothing method has no replacement or reconstruction systems for excessively deformed cells. For this reason we could find the presence of low quality cells that can lead to problems of convergence for the calculation or even the presence of cells with negative volume that would lead to the immediate stop of the calculation code. In order to have an optimal quality of the deformed cells it is necessary that in the preprocessing phase the dimension of the grid area which will be subjected to deformation is appropriately considered, considering that increasing this dimension the computational domain will have more deformed cells but each to a lesser extent.

4.9 Modelling a porous media

As it will be described in section 7.1, the REWEC3 breakwater has been simulated modelling the part of the numerical domain corresponding to the air turbine duct as a porous media (see Fig. 7.1-4). The “porous zone” is characterised by viscous and inertial losses which are used to reproduce the actual pressure losses in the air duct according with the following procedure that aims at identifying the parameters of the “equivalent” porous zone model.

Being the air flow in the conduit fully turbulent, the continuous pressure losses, due to friction on conduit walls have been calculated analytically from Eq. 4.9-1 with Tsal approximation [Genic S., 2011] for the calculation of the friction coefficient, *F* (Eq. 4.9-2):

$$\Delta p_c=\frac{\rho_a F_c \Delta l v_t^2}{2D} \tag{4.9-1}$$

$$F_c=0.11\left(\frac{\epsilon}{D}+\frac{68}{Re}\right)^{0.25} \tag{4.9-2}$$

where ρ_a is the air mean density (assumed constant and uniform in the air duct), v_t is the air flow speed, ε is the wall roughness, *Re* is the Reynolds number, *D* and Δl are the diameter and the length of the conduit, respectively. Minor losses at the entrance and the outlet of the conduit have been evaluated from

$$\Delta p_{i+o} = \frac{1}{2} \rho_a F_{e+o} v_t^2 \tag{4.9-3}$$

where F_{e+o} is the sum of the minor losses coefficients, F_e (entrance) and F_o (outlet). Table 4.9-2 shows the values of the coefficients adopted in Equations 4.9-2 and 4.9-3.

Table 4.9-2 Assumed parameters for Darcy-Weisbach formula and Tsal approximation

Parameter	**Value**
ε [m]	3e-05
F_e	0.5
F_o	1

In order to reproduce the total pressure losses $\Delta p_c + \Delta p_{e+o}$, that are proportional to $\rho_a v_t^2$, by means of the porous medium in the CFD code, the following procedure has been adopted. Recalling the model of a porous medium, the pressure drop $\Delta p_c + \Delta p_{e+o}$ is put equal to the pressure Δp_i due to the "inertial losses" in the porous medium and evaluated by means of an "inertial" resistance coefficient, R_i:

$$\Delta p_i = \frac{1}{2} \rho_a \Delta l R_i v_p^2 \tag{4.9-4}$$

where v_p is the air velocity inside the porous media and Δl is the length of the porous media (equal to the conduit length).

The velocity v_p is evaluated by the continuity equation, neglecting the fluctuations of the air density, ρ_a, in the chamber:

$$G = \rho_a A_t v_t = \rho_a A_c v_c \tag{4.9-5}$$

where G is the instantaneous air mass flow rate, in the air conduit, v_c is the velocity of displacement of the mean water level in the chamber, A_c and A_t are the cross section area of the chamber and the turbine conduit, respectively. The air mass flow rate in the 2D domain, G', per unit of the width of the breakwater, is given by

$$G' = \frac{G}{s} = \rho_a \left(\frac{A_c}{s} \right) v_c = \rho_a A'_p v_p \tag{4.9-6}$$

where s is the width of the plant and A'_p is the cross section area of the porous media per unit of width of the plant. From Eqs. 4.9-5 and 4.9-6, both the equations of v_p and v_t can be obtained as a function of v_c. Putting these equations in Eqs. 4.9-3 and 4.9-4 and imposing $\Delta p_c + \Delta p_{e+o} = \Delta p_i$, the value of R_i has been calculated. Neglecting the influence of v_c on the friction coefficient (Eq. 4.9-2), the value of R_i has been evaluated, resulting equal to 26.4 m^{-1}.

The pressure drop across the Wells turbine is about linearly variable with the axial flow velocity, as confirmed by experiments, (e.g. [Torresi et al., 2007] and [Camporeale and Filianoti, 2008]), and numerical simulations, (e.g. [Camporeale et al., 2003], [Torresi et al., 2008] and [Torresi et al., 2009]). During the operation of the U-OWC installed in Civitavecchia's harbour [Arena et al., 2015], the parameters characterizing the turbine behaviour have recorded under several sea states. In particular, the following parameters were evaluated:

i. the non-dimensional flow coefficient

$$U^* = \frac{u_a}{\omega R_{tip}} \qquad (4.9\text{-}7)$$

obtained from the axial velocity u_a across the turbine, the turbine angular speed ω, the pressure difference and turbine tip radius R_{tip};

ii. the pressure difference Δp, between the chamber and the atmosphere.

Starting from the pressure difference Δp, and neglecting the pressure drops along the air duct, it is possible to evaluate the non-dimensional turbine pressure drop:

$$\Delta p'^* = \frac{\Delta p}{\rho_a \omega^2 R_{tip}^2} \qquad (4.9\text{-}8)$$

The results given in [Arena et al., 2015] confirm about a linear relationship between the turbine parameters Δp^* and U^*. On the basis of these results, known the plant and turbine geometry, the pressure drop across the turbine Δp_t can be related to the air velocity in the air duct, v_t, by means of a proportionality coefficient, k_t:

$$\Delta p_t = k_t v_t \qquad (4.9\text{-}9)$$

In the CFD simulation, the viscous pressure drop Δp_v in the porous medium are associated to a viscous resistance by

$$\Delta p_v = \mu_a \Delta l R_v v_p \qquad (4.9\text{-}10)$$

where R_v, is the viscous coefficient and μ_a is the dynamic viscosity of air. Equating Δp_v to the pressure drop Δp_t across the Wells turbine, and taking into account the relationship between v_p and v_t given by Eqs. (4.9-5) and (4.9-6), it is possible to evaluate the coefficient R_v to be used to simulate the Wells turbine

$$R_v = \frac{4 k_t s}{\pi D \mu_a \Delta l} \qquad (4.9\text{-}11)$$

The value of R_v has been calculated considering in particular the sea state 7 in [Arena et al., 2015], resulting equal to 67.05e+06m^{-2}.

The total pressure drop, $\Delta p_{tot} = \Delta p_c + \Delta p_{e+o} + \Delta p_t$, in the air duct is evaluated as the sum of the “viscous” losses and the “inertial” losses:

$$\Delta p_{tot} = \Delta p_v + \Delta p_i \quad (4.9\text{-}12)$$

4.10 Overview of the solver settings and post-processing phase

The CFD model, used in the simulation of both REWEC1 and REWEC3 devices, solves the Navier-Stokes equations written for an unsteady, compressible, two-phase flow. These equations have been discretized according to a Finite Volume approach and adopting a pressure-based algorithm in its implicit formulation. The two-phase interaction has been taken into account by means of the Eulerian VOF (Volume Of Fluid) model in its explicit formulation, adopting the Geometric-Reconstruction scheme for the interface tracking. Air have been assumed to be compressible, in order to take into account the compressibility of the air pocket inside the chamber of REWECs.

Turbulence has been taken into account by the *Standard k-ω* turbulence model. The *k-ω* model includes two extra transport equations to represent the turbulent properties of the flow. This allows a two-equation model to consider effects like the convection and the diffusion of turbulent energy. The first transported variable is turbulent kinetic energy, *k*. The second transported variable is the specific dissipation, *ω* that determines the scale of the turbulence, whereas the first variable, *k*, determines the energy in the turbulence.

The SIMPLE (Semi-Implicit Method for Pressure Linked Equations) scheme has been used for the pressure-velocity coupling. It is a segregated algorithm that uses a relationship between velocity and pressure corrections to enforce mass conservation and to obtain the pressure field. In order to obtain the spatial discretization of the convection terms in the governing equations, we used the Green-Gauss Cell-Based method to gradient evaluation and PRESTO! (PREssure STaggering Option) scheme for pressure equation. The other convection-diffusion equations (e.g. momentum or energy equation) were discretized by means of the Second Order Upwind scheme.

During the simulations, the coordinates of the points of the domain that constitute the free water surface inside both the wave flume and REWECs chamber have been registered, allowing the analysis of the wave motion in the post processing step. In post processing step, using the registered data, it is possible to create graphs that show the water surface position at any time step of the simulation. Moreover, the value of the mean y-coordinate of the water surface averaged along an x-coordinate range can be evaluated as a function of the time. Reading the written data relative to a time step, a Python program approximately calculates the value of the integral of the water surface along an x-coordinate range, assigned as an input in the program.

The required averaged value, is then calculated as the ratio of the value of the integral over the value of the x-coordinate range. In order to analyse the response of the device under the wave forcing action, the averaged values are calculated considering the x-coordinate range corresponding to the duct mouth length and to the plenum chamber length. Subtracting the value of the water level at rest in the tank and in the plenum chamber and repeating the calculations for each time step of the simulation, the values of the displacement of the water surface, respectively over the duct mouth, y_d, and in the plenum chamber, y_c, as a function of the time are obtained.

5. CFD model validation: calculation of the natural frequency of a scaled REWEC1 device

5.1 Numerical domain description

The analytical model on the basis of the REWECs design had been validated by means of experimental tests. In particular, tests on the REWEC1 device were carried out by means of an experimental facility at Università Mediterranea di Reggio Calabria (Italy). An experimental test rig had been specifically designed (Fig 5.1-1 a and b), embodying a scaled REWEC1 device. The geometrical dimensions of the test rig are summarized in Table 5.1-1. The purpose of the experimental tests was to verify that the variation of the value of the height of the air pocket into the REWEC1, ζ_0, led to a variation of the value of its natural frequency, f_n, which is in agreement with the analytical expectations.

The experimental tests has been replicated by means of our CFD model, in the aim of explore the potential of a low computational effort 2D model. Moreover, the comparison of the CFD results with both analytical and experimental ones led to the validation of the CFD model, that has been used for further investigation on REWECs.

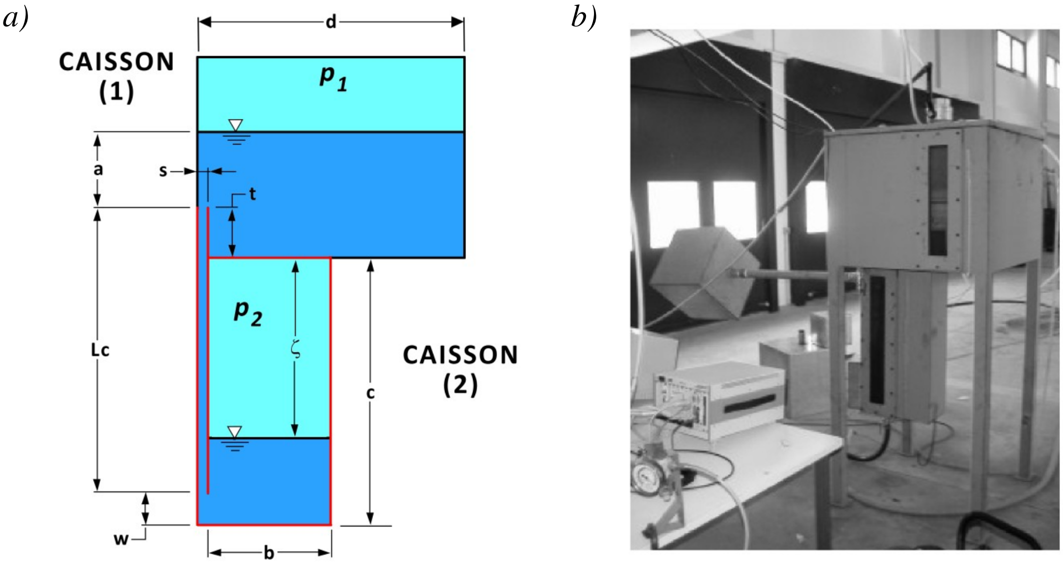

Fig. 5.1-1 The experimental device (b) and its section (a)

Table 5.1-1 Geometrical parameters of the REWEC1 experimental device

L_c [m]	c [m]	w [m]	t [m]	b [m]	d [m]	s [m]
0.850	0.797	0.100	0.153	0.366	0.797	0.032

The experimental test rig mainly consisted of two caissons (Fig 5.1-1a): the lower one (caisson 2) replicated the REWEC1 device, whereas the upper one (caisson 1) simulated the REWEC1 submergence. Moreover, caisson 1 served to generate a non-equilibrium initial condition, according to the following procedure:

1. The valves of both upper (1) and lower caissons (2) were opened, connecting each air pocket with the atmosphere;
2. A specified amount of water was introduced in the upper caisson and part of it overflowed in the lower one. During this operation, the valve in the lower caisson was closed, in order to generate an air pocket inside it with a ζ lower than ζ_0;
3. Air was pumped inside the lower caisson until the desired resting condition was achieved, which corresponds to the value of ζ_0 for which we will calculate the natural frequency, f_n, of the scaled REWEC1. The pressure inside the chamber, p_0, was equal to that arising from the hydrostatic equilibrium with the water into caisson 1;
4. In order to generate the initial non-equilibrium condition ($\zeta_i \neq \zeta_0$ and $p_{2,i} \neq p_{2,0}$), the valve of the upper caisson was closed and air was pumped inside it, reaching $p_{1,in} \neq p_{atm}$;
5. When the valve of the upper caisson was opened, the value of the pressure in the upper caisson dropped to the atmospheric value: the free water levels in the two caissons were no more in hydrostatic equilibrium, hence damped harmonic oscillations were generated reaching the equilibrium condition;
6. Finally, the resting conditions in caisson 2 were reached.

As a result of the free damped harmonic oscillations, the values of the damped natural frequency of the scaled REWEC1, f_d, and of the damping ratio, ξ, can be calculated. The values of f_d and ξ have been evaluated from the time history of the pressure inside caisson 2, p_2, which have been registered by means of pressure transducers. Then, the value of the undamped natural frequency, f_n, was derived:

$$f_n = \frac{f_d}{\sqrt{1-\xi^2}} \tag{5.1-1}$$

which was the objective of the experiments. Several tests had been reproduced by changing both the initial and the resting conditions, as summarized in Table 5.1-2 and Table 5.1-3, respectively.

The CFD analysis has been carried out using a computational domain (Fig. 5.1-2), which reproduces the 2D schematic reported in Fig 5.1-1a. Two different boundary conditions have been considered for the upper edge of the domain. In the first mesh (Fig. 5.1-2a) the whole edge has been set as pressure outlet. In the second mesh (Fig. 5.1-2b), only a part of this edge (with a width equal to 0.0045 m) has been set as pressure outlet. This part of the upper edge reproduces the opening of the valve of caisson 1, which has ½" diameter. In this way, the effect of the opening of the valve on the fluctuations of p_1 can been analysed. The domain has been discretized by means of the grid generator Pointwise adopting multi-block structured meshes. In both cases, the total mesh size is approximately 70,000 cells.

Table 5.1-2 Initial non-equilibrium conditions of the experimental tests (patm = 1013 [mbar])

Test	ζ_i [m]	a_{in} [m]	$p_{1,i}$ [mbar]	$p_{2,i}$ [mbar]
A	0.199	0.076	1241	1288
B	0.252	0.064	1250	1301
C	0.306	0.107	1227	1288
D	0.356	0.159	1229	1300

Table 5.1-3 Resting conditions of the experimental tests (patm = 1013 [mbar])

Test	ζ_0 [m]	a_0 [m]	$p_{1,0}$ [mbar]	$p_{2,0}$ [mbar]
A	0.241	0.064	1013	1063
B	0.306	0.074	1013	1071
C	0.366	0.079	1013	1077
D	0.425	0.140	1013	1089

Both meshes have the same discretization method in the y-axis direction. From the bottom edge of the lower caisson to the duct mouth (y=0 m; y=0.1 m) there are 25 cells whose heights vary from 0.005 to 0.0025 m. From the duct mouth to the upper edge of the lower caisson (y=0.1 m; y=0.797 m) there are 280 cells that have constant heights equal to 0.0025 m. In the upper caisson, a fine mesh zone has been generated in correspondence of the part of the domain in which there is the free water surface.

This zone goes from y=0.95 m to y=1.05 m, using 80 cells with constant heights equal of 0.0025 m. From y=0.797 m to y=0.95 m, there are 35 cells whose heights vary according to a symmetric tanh distribution with a minimum length equal to 0.0025 m. Finally, from y=1.05 m to the upper edge (y=1.397 m) there are 65 cells whose heights vary from 0.0025 to 0.005 m on the upper edge. In the x-axis direction, the same method of discretization has been used in the vertical duct and in the lower caisson of both meshes.

Actually, 10 cells have been used in the vertical duct (x=0 m; x=0.032 m), whose lengths vary according to a symmetric tanh distribution with a minimum length, equal to 0.003 m, near the duct walls. Whilst, 120 cells have been used in the lower caisson, whose lengths vary according to a symmetric tanh distribution with a minimum length, equal to 0.003 m, near the caisson walls. In the upper caisson, from x=0.032 m to x=0.398 m, there are 120 cells in both meshes, whose lengths vary according to a symmetric tanh distribution with a minimum length equal to 0.003 m in the first and from 0.003 m to 0.00225 m in the second mesh. In the first mesh, the part of the upper caisson, which goes from x=0.398 m to x=0.797 m, has been discretized using 100 cell whose lengths vary from 0.003 m to 0.005 m. In the second mesh, instead, 2 cells (having a constant length of 0.00225 m) are considered from x=0.398 m to x=0.4025 m, in order to discretize the opening of the valve. The remaining part of the upper caisson, which goes from x=0.4025 m to x=0.797 m, has been discretized with 85 cells whose length vary from 0.00225 to 0.005 m.

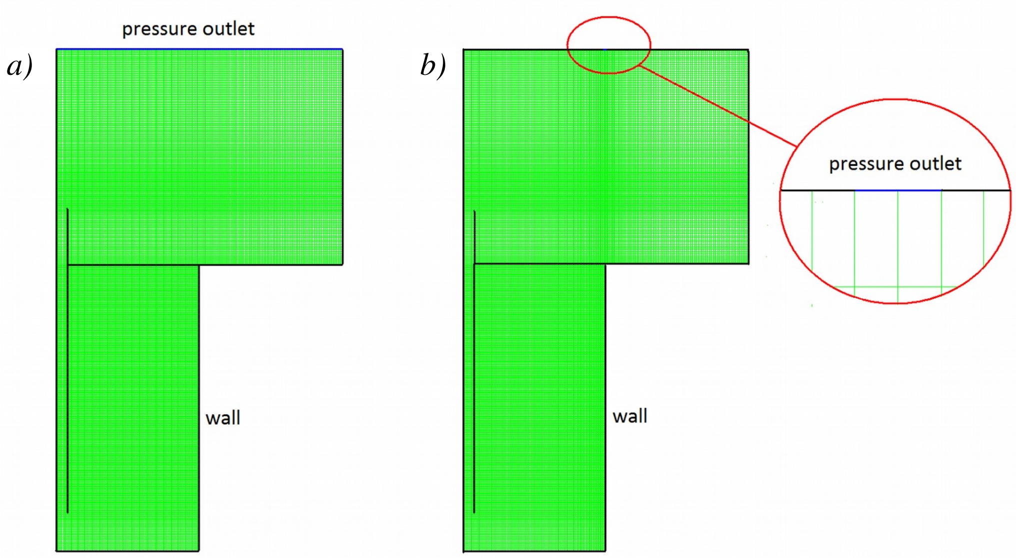

Fig. 5.1-2 The computational domains, considering the whole upper edge as pressure outlet, a), or reproducing the valve opening, b)

Every two time steps, the values of the pressure inside both the lower and the upper caissons have been registered, allowing the analysis of the dynamic behaviour of the water inside the device during post processing.

5.2 Performance analysis: calculation of the REWEC1 natural frequency

The simulation carried out reproducing the experimental test rig had the objective to verify the capability of a REWEC1 device to operate in resonance conditions. In the aim of reproduce with a CFD model the experimental tests, firstly the effect of the sudden opening of the valve has been analysed. Referring to Tables 5.1-2 and 5.1-3, the simulation of test A has been run using both the meshes *a* and *b*.

Moreover, the effect of modelling turbulence has been investigated. In fact, simulations have been carried out without any turbulence model (Fig. 5.2-1) and with the k-ω turbulence model (Fig. 5.2-2). In both cases, the values of p_2 registered during the simulations of test A on both meshes are almost the same, then it is possible to neglect the effect of the top wall opening width, since the p_2 values registered. This means that the ½" opening is sufficiently wide to allow a fast emptying of the initial pressurized air in the upper caisson. For this reason, the simulation of the other tests have been performed using only the first mesh. Fig. 5.2-3, 5.2-4, 5.2-5 and 5.2-6 shows the comparison between the values of p_2 registered during the experimental tests and the CFD simulations in tests A, B, C and D.

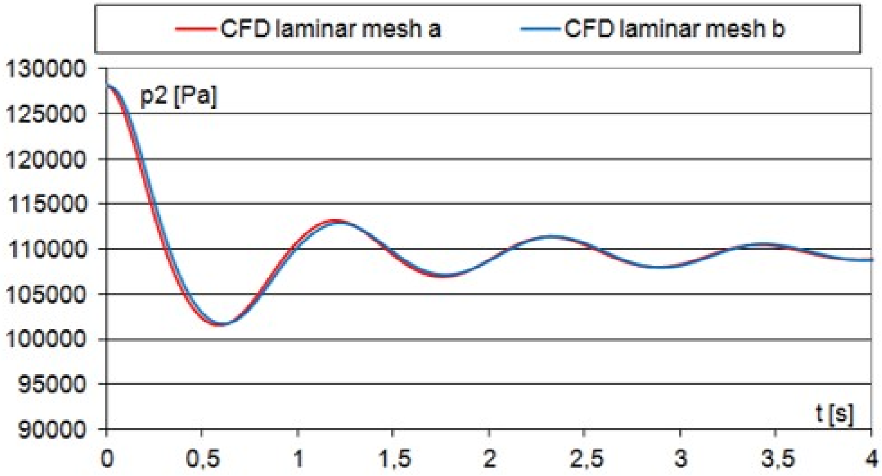

Fig. 5.2-1 Comparison between the values of p_2 registered adopting mesh a and mesh b during the simulation of test A. Turbulence has not been modelled

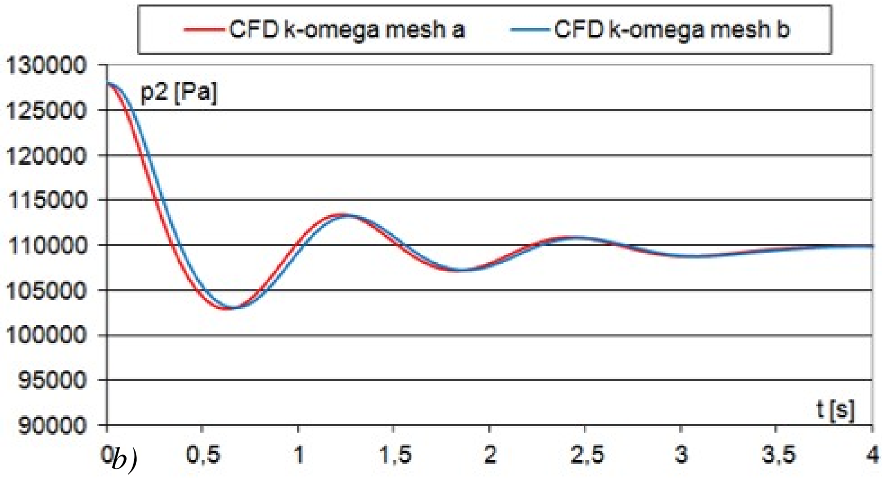

Fig. 5.2-2 Comparison between the values of p_2 registered adopting mesh a and mesh b during the simulation of test A. Turbulence has been modelled by the k-ω turbulence model

The first thing to put in evidence is that during the experiments it was not possible to have an infinitely fast opening of the valve like in the simulations. For this reason, there is a delay in the starting of pressure oscillation during the experiment in comparison to the CFD results.

For all the tests, the simulations carried out by using the standard *k-ω* turbulence model have shown better performance in terms of evaluation of the system natural frequency, f_n, with respect to simulations carried out without any turbulence model. In particular, in tests A and B the damping periods of p_2 registered without considering any turbulence model appear quite smaller than the ones arising from both the experimental and numerical results obtained implementing the k-ω turbulence model.

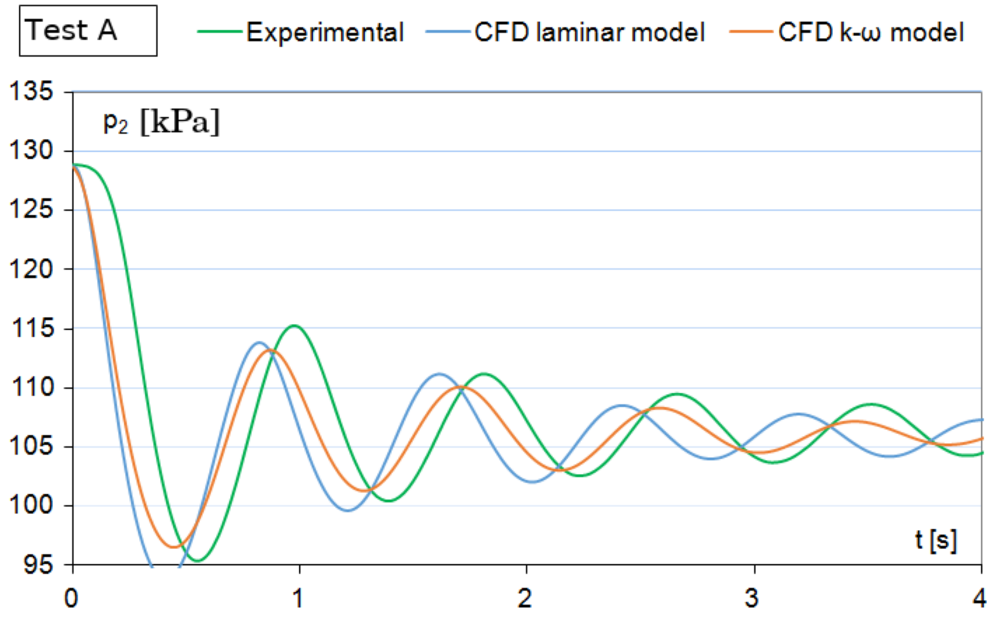

Fig. 5.2-3 Comparison between the values of p_2 registered during the experimental tests and the CFD simulations (Test A)

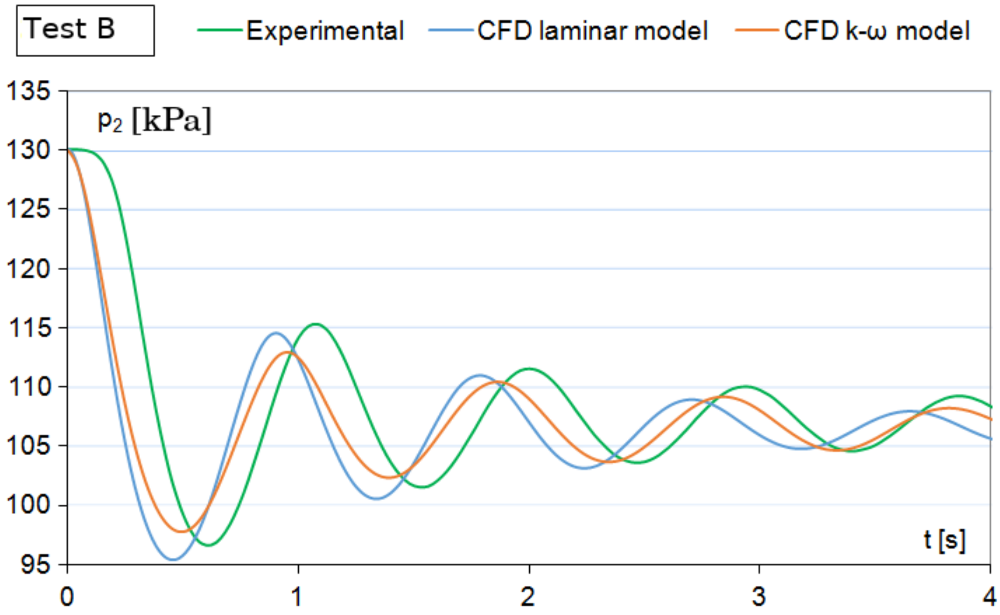

Fig. 5.2-4 Comparison between the values of p_2 registered during the experimental tests and the CFD simulations (Test B)

However, in tests C and D, a better agreement is achieved, in terms of damping period, between the results obtained without any turbulence model with both experimental results and the ones obtained with the k-ω turbulence model. It may be due the fact that oscillations get smaller and the natural frequencies are reduced.

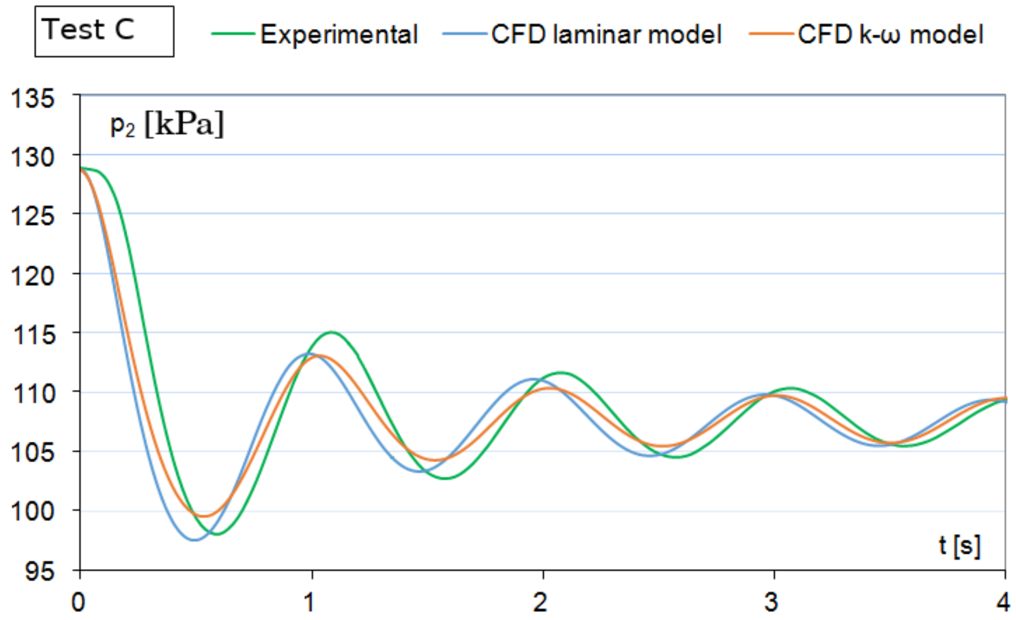

Fig. 5.2-5 Comparison between the values of p_2 registered during the experimental tests and the CFD simulations (Test C)

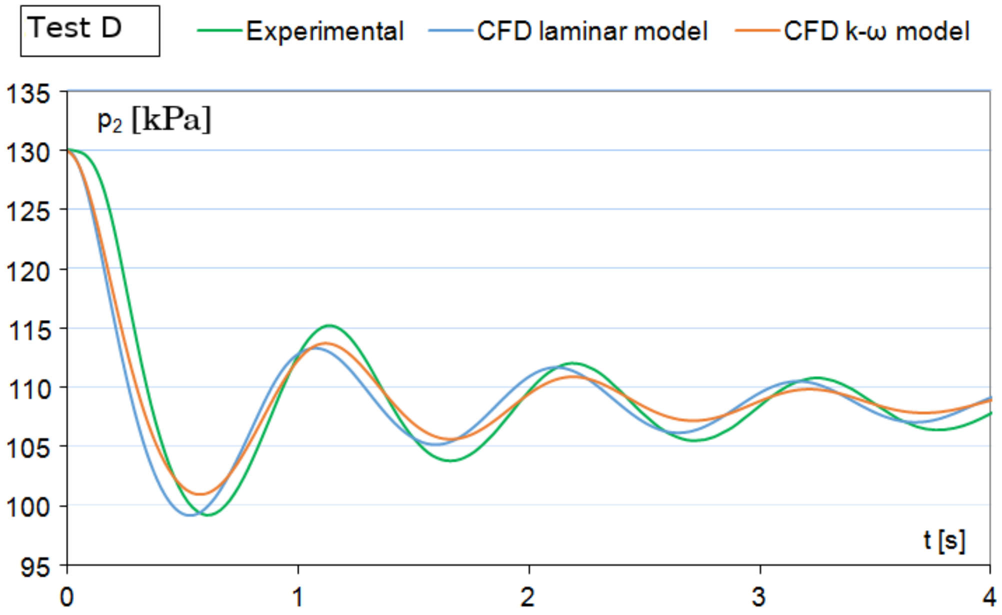

Fig. 5.2-6 Comparison between the values of p_2 registered during the experimental tests and the CFD simulations (Test D)

For both the experimental tests and the CFD simulations, the time period evaluated between the second and the third peak of the oscillations has been assumed to be equal to the damped natural period, T_d. From this, the values of the damped natural frequencies, $f_d=1/T_d$, have been calculated. The value of the undamped natural frequency, f_n, has been calculated from the value of f_d, in order to make a comparison with the analytical result:

$$f_n=\frac{f_d}{\sqrt{1-\xi^2}} \qquad (5.2\text{-}1)$$

The value of the damping ratio, ξ, has been evaluated computing the logarithmic decrement, δ, between the second and the third peak of the oscillations. From the value of δ, the following equation has been used for the calculation of the damping ratio, ξ:

$$\delta=2\pi\frac{\xi}{\sqrt{1-\xi^2}} \qquad (5.2\text{-}1)$$

The graph reported in Fig. 5.2-7 shows the comparison between the values of the natural frequency, f_n, calculated from the analytical model, the experimental tests and the CFD simulations (either without any turbulence model or with k-ω one). The values of f_n calculated by means of the analytical model are in fairly good agreement with the experimental ones for each test, except some differences found in test A.

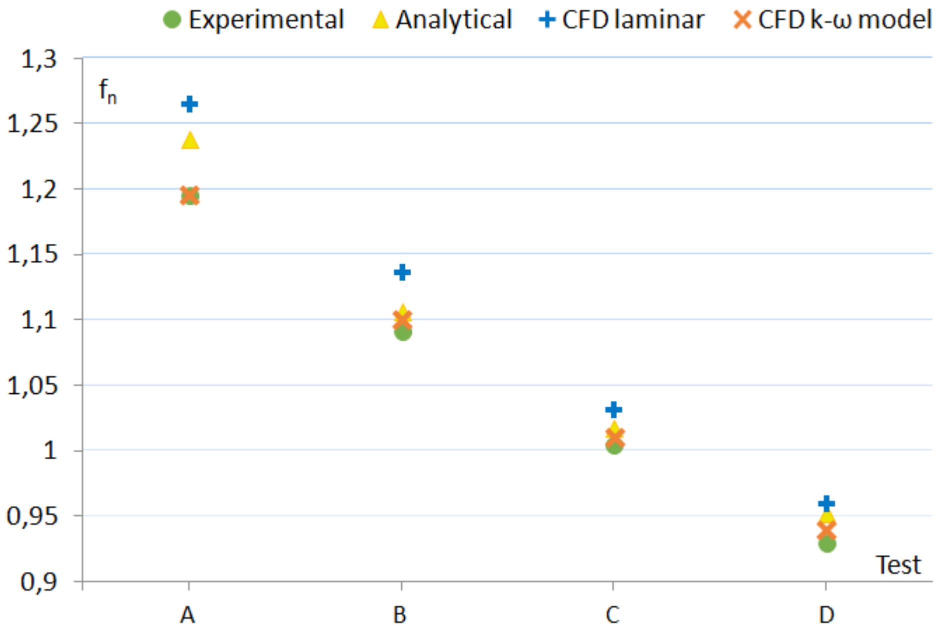

Fig. 5.2-7 Comparison between the values of f_n

The results arising from the CFD simulation carried out adopting the laminar model fit very well the experimental ones in tests C and D, while there are some differences in tests A and B. Finally, considering the values of f_n calculated from the CFD simulation carried out adopting the k-ω model, there is a good agreement with the experimental values for all the tests.

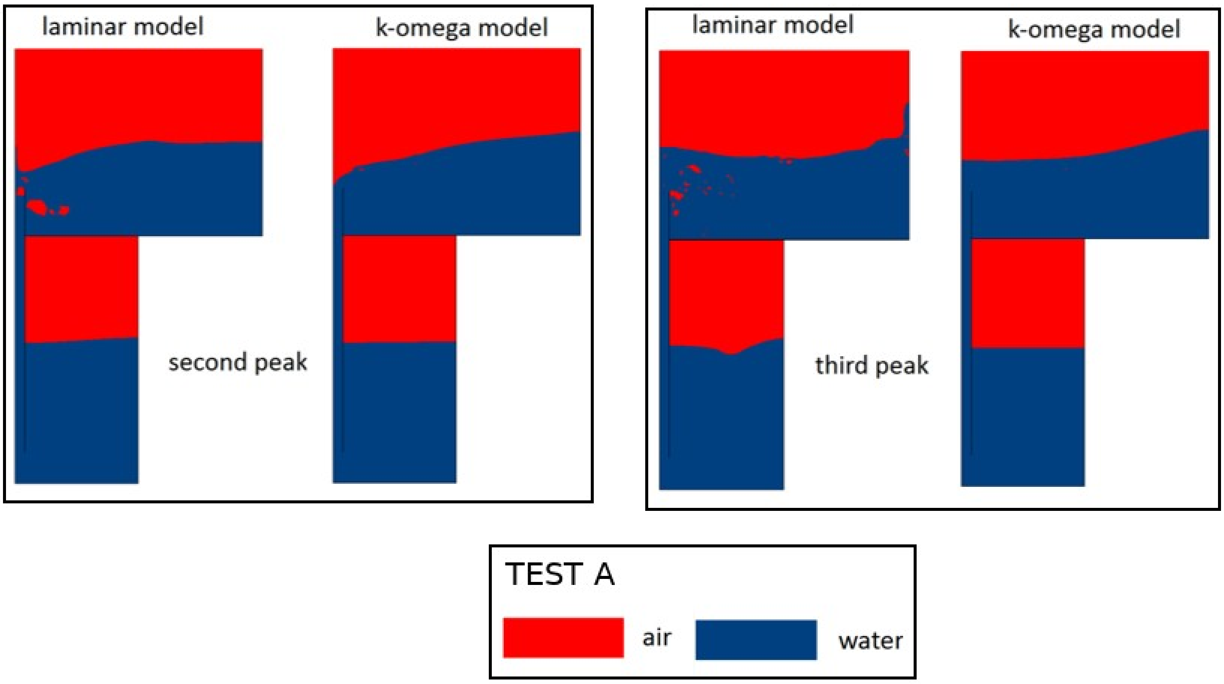

Fig. 5.2-8 Contours of water and air registered during the simulation of Test A

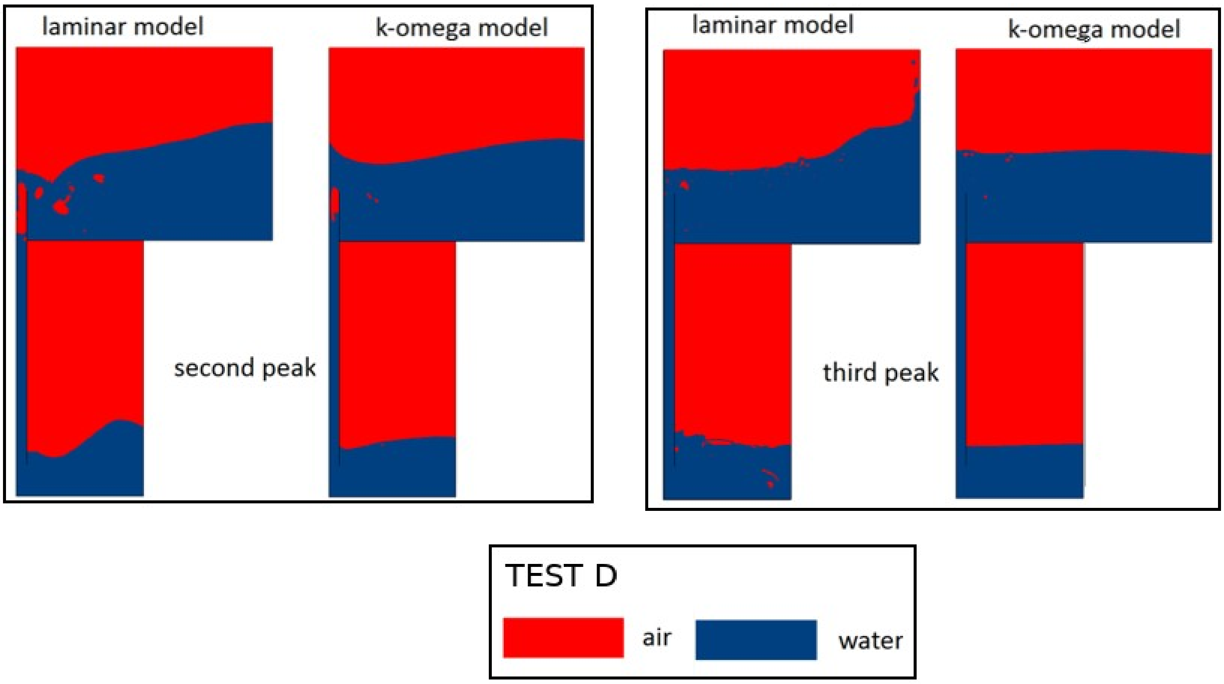

Fig. 5.2-9 Contours of water and air registered during the simulation of Test D

In order to evaluate the evolution of the free water surfaces in both caissons (1) and (2), the contours of air and water have been registered during the simulations. Fig. 5.2-8 and Fig

5.2-9 show the contours of air and water registered during the simulations of tests A and D, respectively.

The first is one in which the laminar model results differ from the analytical, experimental and k-ω ones (see Fig. 5.2-7); the second is one in which the analytical, experimental, laminar model and k-ω model results are in good agreement. It has been considered the occurrence of the second and the third peak of oscillation of p_2 inside the lower caisson. When the k-ω model has been used, the free water surface in the upper caisson is more regular than the one resulting from laminar calculations, without the generation of air bubbles. The same considerations are valid also when the free water surface in the lower caisson is considered, which, in accordance with the analytical expectation, is almost 1D in the k-ω simulations.

6. Simulation of the interaction between waves and a scaled REWEC1 breakwater

6.1 Numerical domain description

The validated CFD model has been applied for analyse the interaction between waves and a scaled REWEC1 breakwater. Scaled model are often used in experimental and CFD analysis for several purpose, such as to evaluate the design accuracy or to provide a deep insight of the flow dynamics aspects. Then, the CFD simulation of scaled REWEC1 breakwaters can be considered a useful and novel tool, permitting to investigate the dynamics of wave breaking on the device and the dynamic of the water flow near and inside the device, in order to define any design improvements. Moreover, a novel procedure to calculate the breakwater reflection, dissipation, absorption and transmission coefficient by means of CFD has been set up.

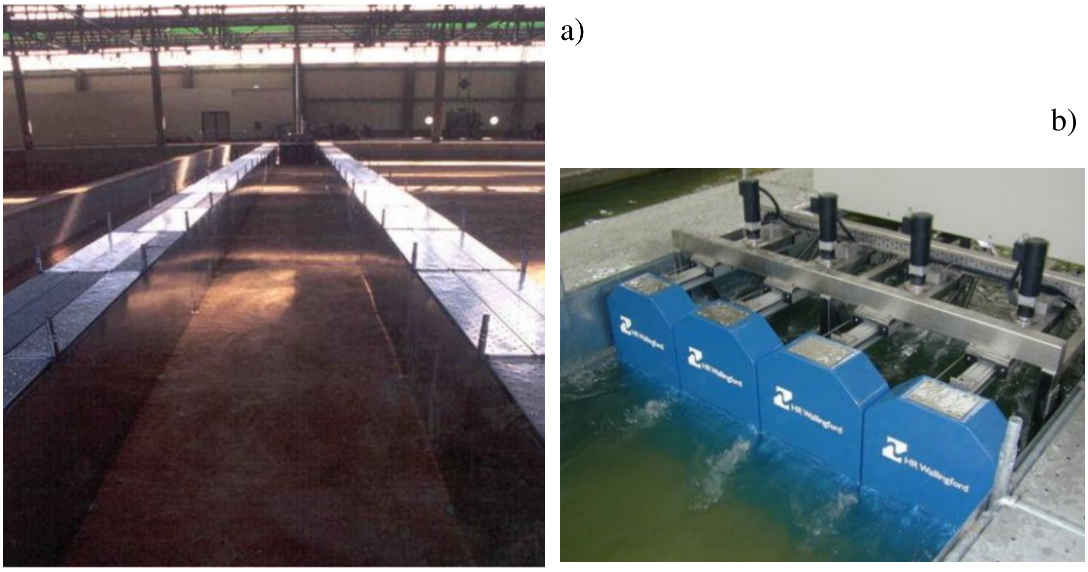

Fig. 6.1-1 LIC (Politecnico di Bari) facilities: channel used for two-dimensional simulations, a), and piston-type wave-makers b)

In the aim of investigate the possibility of carry out experimental tests in the future, the computational domain corresponded to one of the two identical wave flumes (figure 6.1-1a) available at LIC (Laboratorio di Ingegneria delle Coste) of Politecnico di Bari. The wave flumes, more similar to channels, are used for the reproduction of two-dimensional phenomena. They have a total length of 50 m for a width of 2.40 m and a depth of 1.20 m. Piston-type wave-makers (figure 6.1-1b) are used to generate waves with different characteristics, through the translation movement of the piston-wall.

A REWEC1 scaled device has been designed in order to operate inside the wave flume, following the analytical method analysed in the previous section. As a starting work, it as been considered the reproduction of a device without the power-take off system. The design constrains were related to the geometry of the LIC channel, then the values of the level of water filling the tank, of the amplitude of the generated waves and of the submergence *a* (see Fig. 4.1-2 and 4.1-3) have been preliminarily fixed. The geometrical parameters of the scaled device are reported I Table 6.1-1.

Table 6.1-1. Geometrical parameters of the scaled REWEC1 device

d_1	c'	d_3	l
[m]	[m]	[m]	[m]
0.9	0.2	0.25	2.4

Actually, a submerged impermeable breakwater first and a REWEC1 breakwater have been numerically simulated, in order to made a comparison between the two. The domain, reported in (Fig 6.1-2) was 2D, considering a section of both the impermeable and REWEC1 breakwaters. This simplified model provides a good reproduction of the interaction between regular waves, which propagate perpendicularly to the length of the breakwater, and the whole breakwater itself. In fact, the breakwaters length is usually large, then the wall effects at the ends can be neglected when one evaluates the behaviour of the whole system.

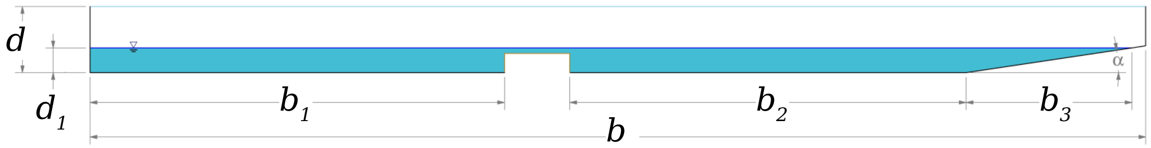

Fig 6.1-2 The numerical wave flume with a submerged breakwater inside

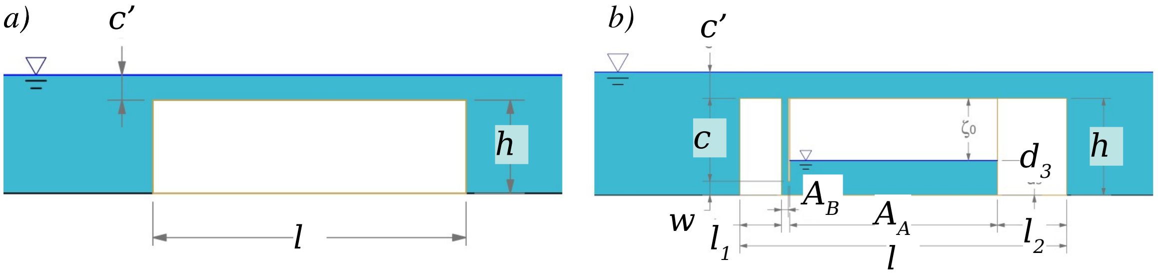

Fig 6.1-3 Dimensions of the impermeable breakwater, a), and of the REWEC1, b)

The numerical wave flume had an overall length of 38.1 m, an overall height of 2.4 m and the water level was set at an height d_1 equal to 0.9 m from the bedside. The breakwaters were placed 15 *m* downstream the left end of the domain, allowing the full development of regular waves of 0.08 m amplitude and 4 m wavelength. Past the breakwaters, there is first a horizontal stretch (b_2 =14.35 *m* in length) and then an inclined section (b_3=6.5 *m* in length) with a slope of 8.5°, simulating the presence of a shore.

The submerged impermeable breakwater had a rectangular section of width *l*=2.36 *m* and height *h*=0.7 *m*, hence the submergence was *c'*=0.2 *m*, as reported in Fig. 6.1-3a. The section of the REWEC1 breakwater (Fig. 6.1-3b) consists, instead, in a U-tube placed between two rectangular blocks of l_1 = 0.3 *m* and l_2 = 0.5 *m* in width. The left branch of the U-tube (called vertical duct) is connected to the sea through an upper opening. The vertical duct extends along the wave-beaten side of the caisson having an height *c* = 0.6 *m*. The second branch is a pressurized plenum chamber. The two branches are connected together by means of an opening with height *w* = 0.1 *m*. The width of the vertical duct was A_B = 0.05 *m*, whilst the width of pressurized chamber was A_A = 1.5 *m*.

Under the action of the waves, the pressure oscillates above the upper opening of the vertical duct. Therefore, the water flows up and down in the duct and in the plenum, in this way the air pocket acts as gas spring. Actually, the air pocket is pressurized by means of a compressor connected by a flexible pipe to an opening in the upper wall of the chamber. In order to reproduce that, the simulation has been initialized setting the value of the air pocket pressure equal to 107690 *Pa*. This value leads to an equilibrium, at rest water conditions, between the air pressure and the free water surface above it, considering the chamber filled of water for an height, d_3, equal to 0.25 *m*.

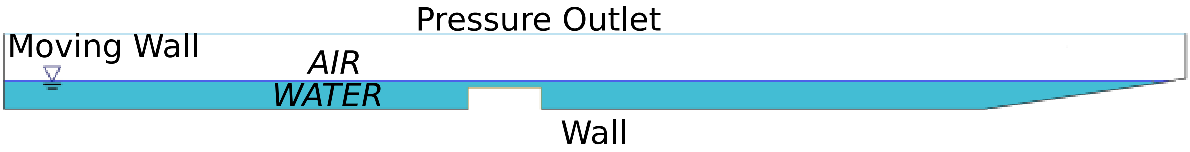

Fig. 6.1-4 The boundary conditions

The numerical domain has been discretized by means of the grid generator Pointwise adopting a multi-block structured mesh. A finer mesh has been used next to the two water free levels (inside the flume and inside the REWEC1), in order to accurately capture the wave profile. In the case of the impermeable breakwater, the total mesh size had approximately 547,000 cells. The same numerical flume has been used in the case of the REWEC1 breakwater, meshing the vertical duct and the plenum chamber. The additional mesh, associated to the U-tube, has been discretized with an hybrid mesh, reaching an overall number of cells equal to 1,093,700.

Regarding the boundary conditions (Fig. 6.1-4), the upper edge has been set as pressure outlet, reproducing the atmosphere above the channel. The walls representing the breakwater wall and the channel ground have been set as no slip walls. The whole edge at the left end of the flume has been setted as a moving no slip wall, acting as a piston-type wave maker and generating waves. In accordance with the wave-maker theory, regular waves of 0.16 m height and 1.706s period ware generated imposing by means of a User Defined Function (UDF) a sinusoidal motion (section 4.8).

6.2 Results: deep insight into the flow field and evaluation of the reflection, absorption and transmission coefficients

The CFD simulation of the interaction between waves and a scaled REWEC1 device has permitted a deep insight into the behaviour of the water flow inside the REWEC1 and around it.

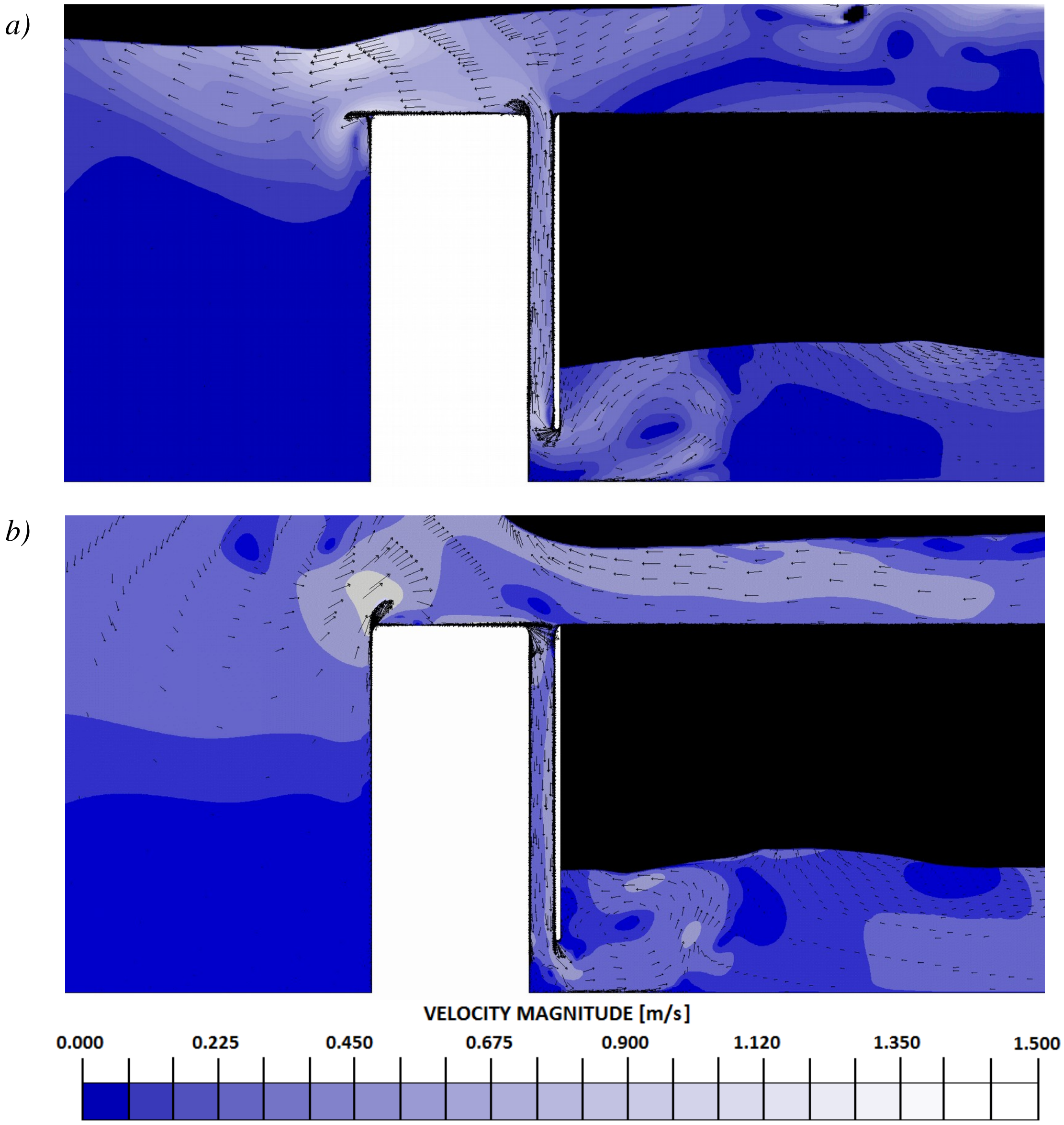

Fig. 6.2-1 Velocity vectors overlaid to the contours of velocity magnitude for the water phase near and inside the vertical duct

This allows, as a first result, to verify the analytical hypothesis of 1D water flow inside both the duct and the chamber, which is on the basis of the design of the REWEC1. Fig. 6.2-1 shows the velocity magnitude contours of the water flow inside the vertical duct, the velocity vectors are overlaid and their dimension is proportional to the velocity magnitude. Two opposite flow conditions are considered, namely the occurrences of maximum water outflow from the vertical duct, Fig 6.2-1a, and the maximum water inflow, Fig. 6.2-1b. In both cases, water flows vertically for almost the full length of the duct, in good agreement with the 1D flow hypothesis. Streamline deviations are evidenced only in correspondence of both the duct mouth and the bottom opening to the chamber, where vortexes are generated due to dissipation.

Fig. 6.2-2a and 6.2-2b show the contours of the velocity magnitude of the water flow inside the chamber. Also in this case they have been considered the two occurrences maximum water outflow and inflow, respectively. In both cases, the free water surfaces inside the plenum chamber are not horizontal, as we expected if the all the water in the chamber had followed a vertical (1D) streamline. It is evidenced the generation of a significant wave motion, connected to the propagation of the vortex generated at the vertical duct bottom opening. Then, it results a discrepancy between the fluid dynamics behaviour resulting from the CFD simulation in respect to the analytical design assumptions.

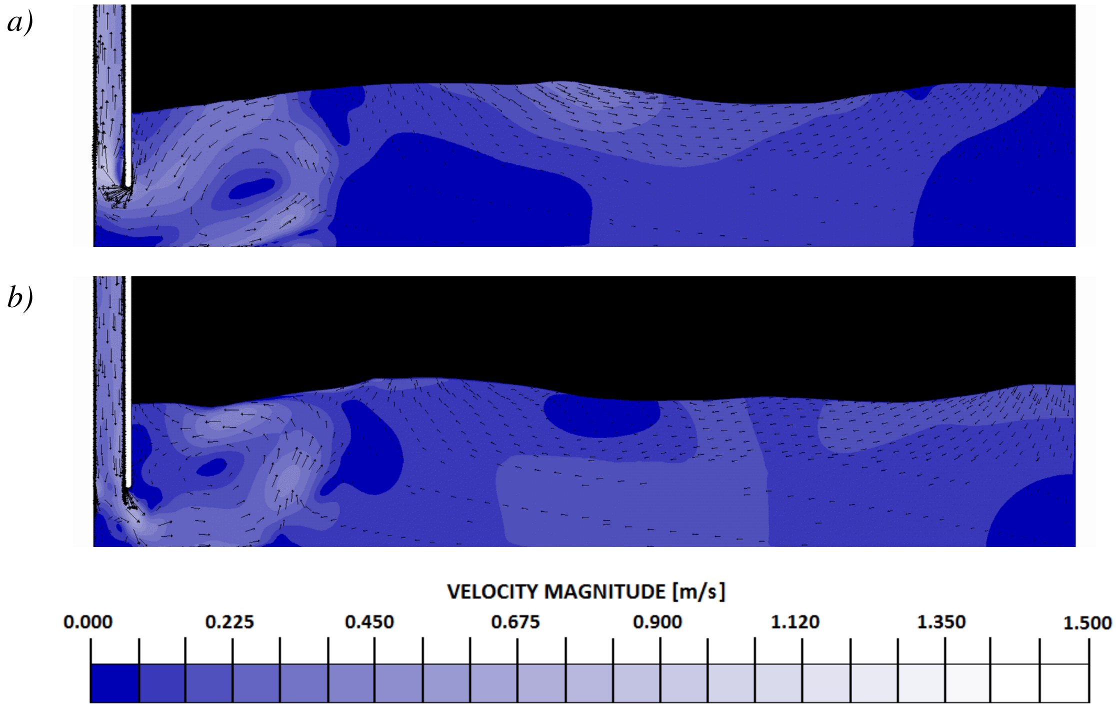

Fig. 6.2-2 Contours of the velocity magnitude of the water flow inside the chamber

Considering the wave field inside the channel, the progressive waves, generated by the moving wall, impacted on the breakwater being partially reflected towards the wave generator and partially transmitted on the lee. The reflected wave interacts with the incident progressive wave generating a partial standing wave field upstream of the breakwater, while the transmitted wave creates a progressive wave field downstream. For instance, Fig. 6.2-3 shows the surfaces of the waves upstream the breakwater (the breakwater is placed at x=15m), measured every one sixteenth of the 18th period of the simulation.

Fig. 6.2-4 shows the averaged envelopes of the waves upstream both the impermeable and REWEC1 breakwater, starting from the 14th up to the 18th period of the piston oscillations. The envelopes confirm the generation of a partial standing wave field due to reflection on both piston and breakwaters.

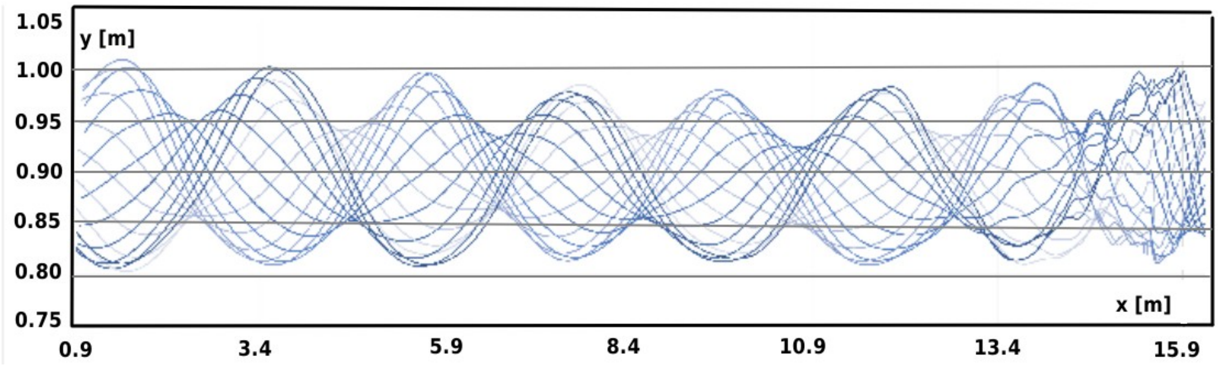

Fig. 6.2-3 Evolution of the water surface upstream the breakwater during the 18th period

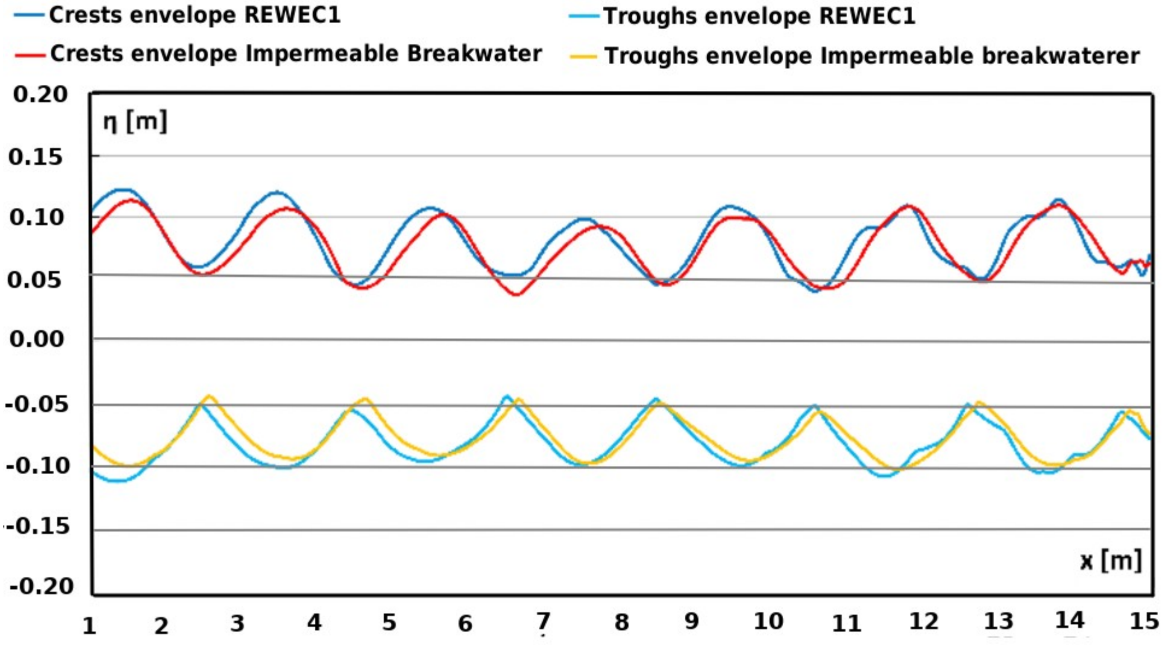

Fig. 6.2-4 Envelopes of waves upstream the breakwater, from the 14th up to the 18th period

Finally, Fig. 6.2-5 shows the averaged envelopes of the waves downstream both the impermeable and REWEC1 breakwater, starting from the 14th up to the 18th period of the piston oscillations. In this case is not possible to distinguish a periodic phenomenon as the partial standing wave in Fig. 6.2-3. The envelopes are almost flat, related to a progressive wave, with the presence of some peaks due to reflection on both the breakwater and the shore. Another important result has been the set up of a procedure for calculate the breakwaters performance coefficients in the post-processing phase. The reflection coefficients have been evaluated according to the method proposed by Kittitanasuan and Goda [Kittitanasuan W. and Goda Y., 1994]. This methodology is based on the Goda&Suzuki technique [Goda Y. and Suzuki Y., 1976], which operates in the frequency domain. The Kittitanasuan method allows the identification of the incident and reflected components, which determine the partial standing wave, starting from the simultaneous sampling of the wave records taken at two adjacent locations.

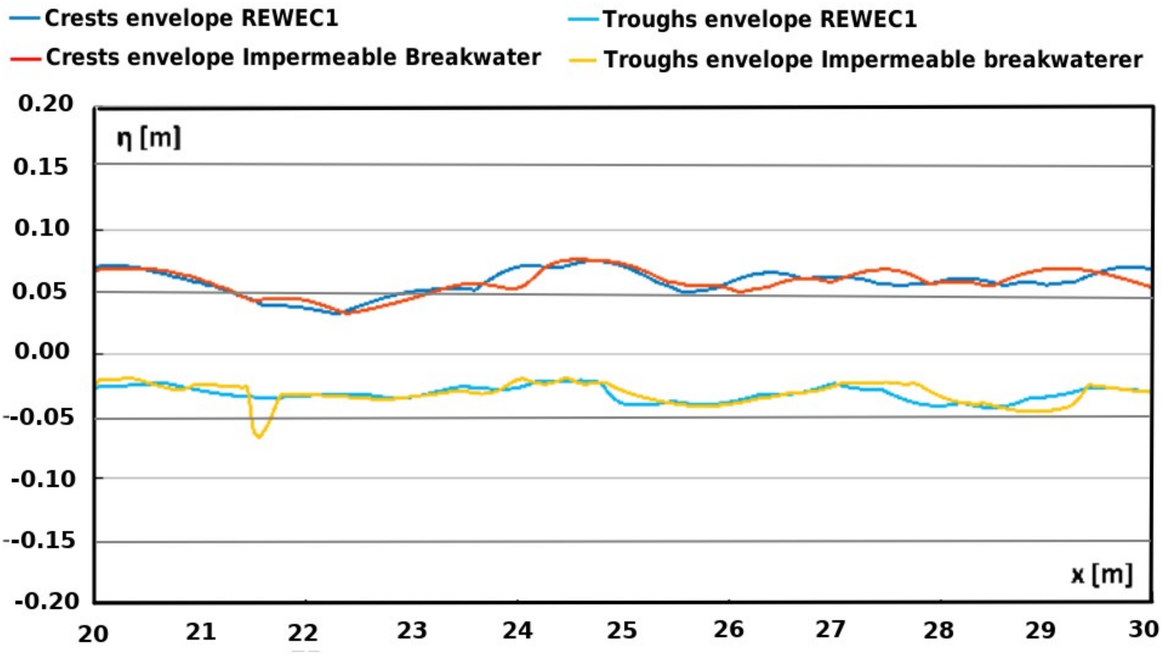

Fig. 6.2-5 Envelopes of waves downstream the breakwater, from the 14th up to the 18th period

Actually, the height of both the equivalent incident wave, H_i, and the equivalent reflected one, H_r, are evaluated based on the values of the amplitudes of the free water oscillations in the two axial positions. The gauge spacing, x, between the two adjacent points, has been determined by the value of the incident wavelength, λ, according to following guideline:

$$0.05 < \frac{\Delta x}{\lambda} < 0.45 \qquad (6.2\text{-}1)$$

The lower and upper limits correspond to f_{min} and f_{max} respectively, from which we obtain the spectral resolution. The incident and reflected wave heights are calculated by converting the energy of all resolved incident and reflected components. The values of incident and reflected energy are obtained by the amplitudes of incident and reflected wave components respectively. This amplitudes are estimated from the Fourier components, applying the FFT technique. According to this method, the distance between two axial positions has been set equal to 0.4 *m*, coherently with the expected spectral range. Furthermore, the first axial position, x_1, has been placed at 8 *m* from the wave-maker.

The time period in which the oscillations have been registered goes from the 14th to the 18th period of oscillation of the wave-maker. The data measured in the two axial positions, have been analysed by means of FFTs in the frequency domain, from which the values of H_i and H_r for the two cases of the impermeable breakwater and the REWEC1 one have been evaluated.

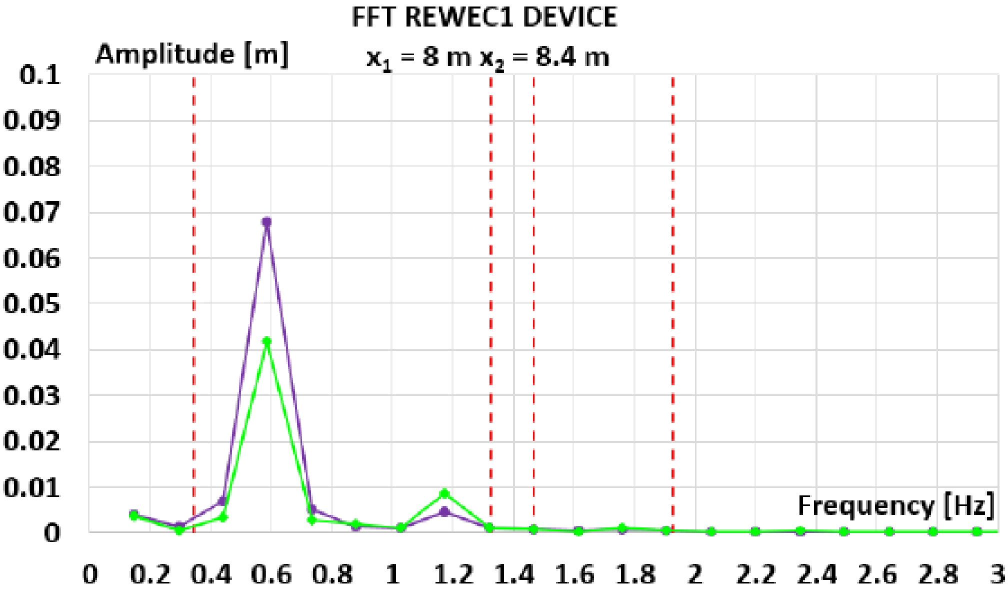

Fig. 6.2-6 FFT analysis upstream the REWEC1 breakwater

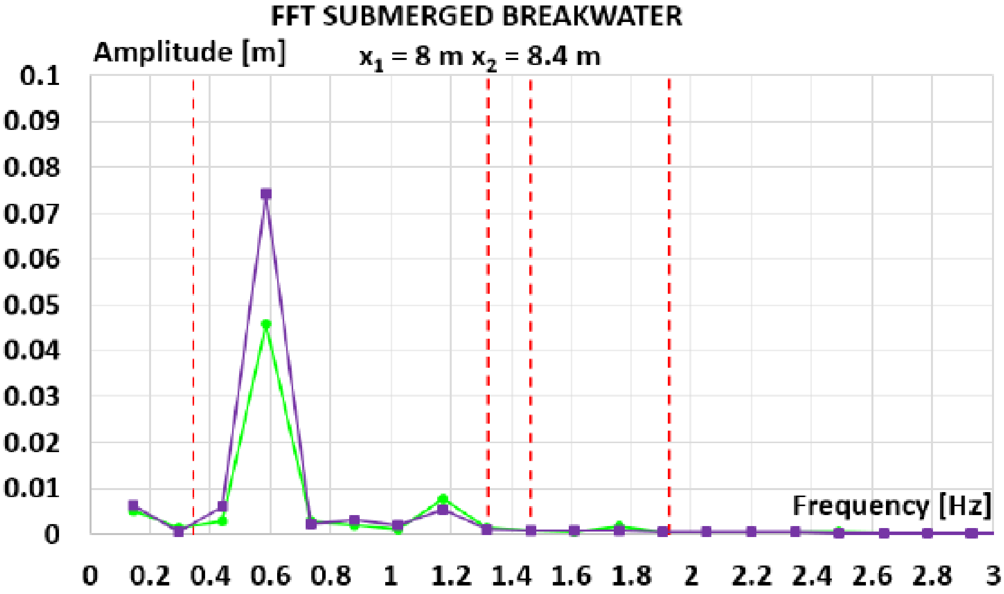

Fig. 6.2-7 FFT analysis upstream the impermeable breakwater

In Fig. 6.2-6 and 6.2-7 are reported the graph resulting from the FFT analysis carried out upstream the REWEC and the impermeable breakwater, respectively. The spectrum of the incident wave is represented in the blue line, whilst the one of the reflected wave in green. As we can see, only a peak of amplitude is present, corresponding to the waves frequency.

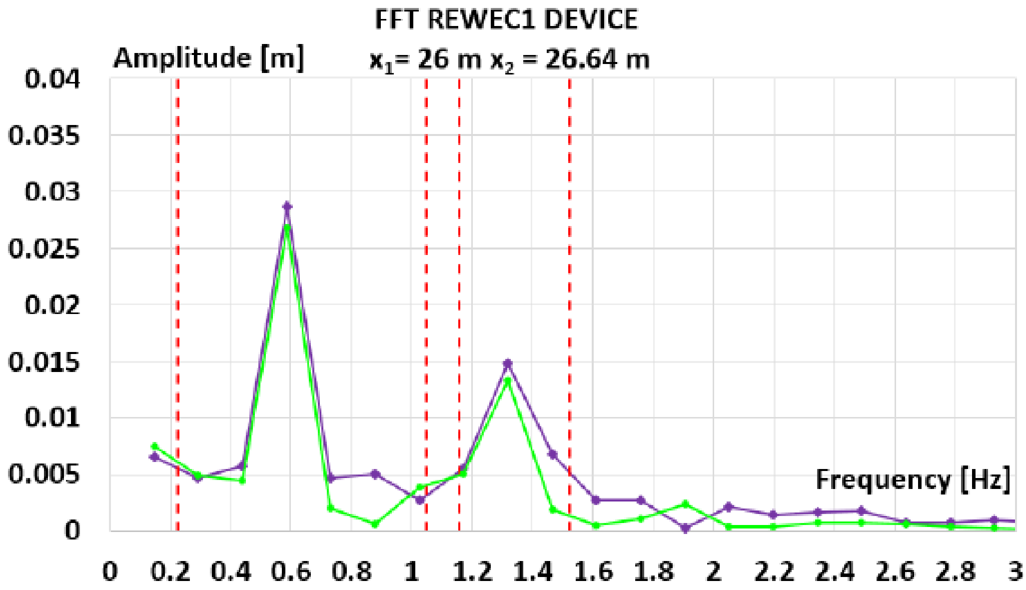

Fig. 6.2-8 FFT analysis downstream the REWEC1 breakwater

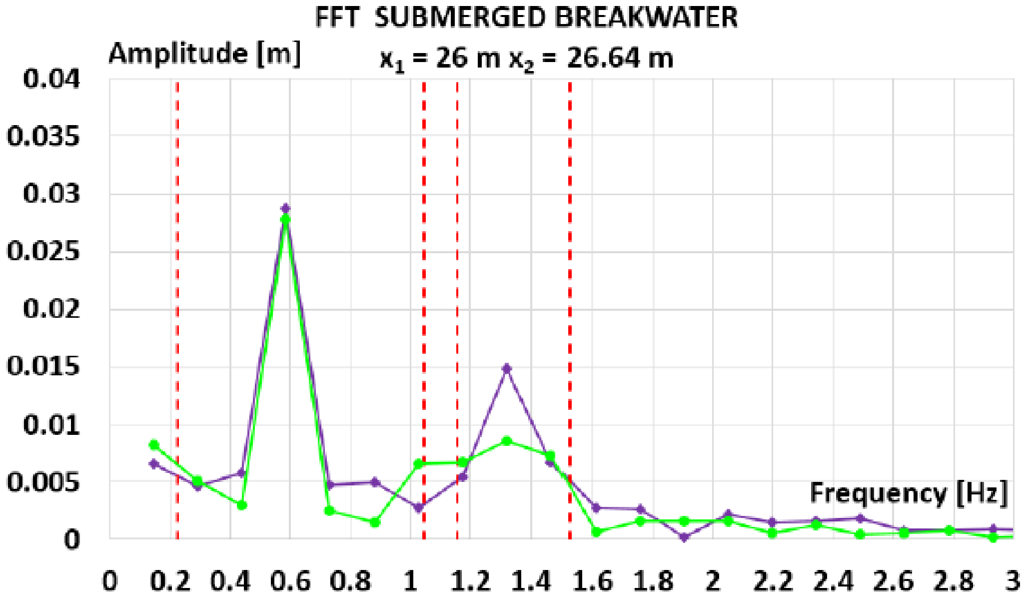

Fig. 6.2-9 FFT analysis downstream the impermeable breakwater

From FFT analyses, it results that in the case of the impermeable breakwater H_i and H_r are equal to 0.131 *m* and 0.052 *m*, respectively; whereas $H_i = 0.136$ *m* and $H_r = 0.054$ *m* in the case of the REWEC1. Therefore, the reflection coefficients result equal to $K_{r,b} = 39.40\%$ for the impermeable breakwater and $K_{r,R}$ = 39.90% for the REWEC1. All the results are reported in Table 6.2-1.

The transmitted wave had a lower height in comparison to the incident one, due to the reflection in front of the breakwater and the dissipation over it, as shown in the envelops in Fig. 6.2-5. The transmitted wave height, H_t, have been calculated in the same way for the case of the impermeable breakwater and the REWEC1 one, by means of the Kittitanasuan&Goda method.

Table 6.2-1 Evaluation of the reflection coefficient

	Impermeable Breakwater	**REWEC1 Breakwater**
H_i [m]	0.131	0.136
H_r [m]	0.052	0.054
K_r [%]	39.40	39.90

Table 6.2-2 Evaluation of the transmission coefficient

	Impermeable Breakwater	**REWEC1 Breakwater**
H_i [m]	0.131	0.136
H_t [m]	0.074	0.075
K_t [%]	56.65	55.35

This method allowed to separate the transmitted wave from the reflected one in the lee of the breakwaters. In fact, a reflected wave was generated by the impact with the shore. However, the incident wave height is the same which is obtained by Kittitanasuan&Goda technique for the calculating of the coefficient K_r. According to this technique, the wave gauge spacing is fixed at 0.64 *m*, where the first point has been placed at 26 *m* from the wave-maker. The results of the FFT analyses are reported in Fig. 6.1-8 and 6.1-9 for the cases of REWEC1 and impermeable breakwater, respectively. The equivalent transmitted wave height has been resulted equal to 0.074 *m* and 0.075 *m* for the impermeable breakwater and the REWEC1, respectively. The transmission coefficient result equal to $K_{t,b}$ = 56.65% for the impermeable breakwater and to $K_{t,R}$ = 55.35% for the REWEC1. All the results are showed in Table 6.2-2.

The amount of energy dissipated on a breakwater is mainly related to the breakwater form. Considering that, it is reasonable to assume that the dissipation coefficient, K_d, of both the impermeable breakwater and the REWEC1 one is the same. In fact, in the REWEC1 breakwater only the vertical duct opening differentiated the external form in respect to the impermeable breakwater.

In the case of the impermeable breakwater, the dissipation coefficient was derived from the energy balance applied starting from the values of the reflection and transmission coefficients:

$$K_r^2+K_t^2+K_d^2=1 \tag{6.2-2}$$

From which K_d results equal to 25.66%. In the case of the REWEC1 breakwater, the absorbed fraction must be taken into account in the energy balance:

$$K_r^2+K_t^2+K_d^2+K_a^2=1 \tag{6.2-3}$$

Then, imposing the value of the dissipation coefficient equal to the impermeable breakwater one, from eq. the value of the REWEC1 absorption coefficient resulted equal to K_a=5.29%.

6.3 Discussion: possible improvements

The original method proposed for the calculation of absorption and transmission coefficients of breakwaters can be applied to other cases. First of all, on the basis of the simulation carried out on the scaled REWEC1 breakwater, it can be explored the variation of the absorption coefficient as a function of the waves period. This would led to two results. The first one is to verify that the considered wave motion is actually the one which the REWEC1 device works under resonant conditions. In fact, smaller absorption values should be observed by varying the wave period. The second result is to verify if there is a narrow or a flat peak around the maximum absorption rate, as a function of the wave period.

The CFD model could led, also, to an extimation of the forces that waves transmits on the breakwaters, being an useful tool in the design phase of such type of structures.

Moreover, it could be considered the presence of a PTO-system inside the REWEC1. It would make more sense if a full-scale breakwater is simulated. In fact, in the simulation of the scaled device no PTO has been considered because the Wells water turbine would have been very small and difficult to achieve in a similar experimental model. The water turbine could be modelled by implementing its pressure loss law, in accordance with the method proposed for the REWEC3 air turbine.

Finally, it could be analysed the accuracy of the proposed 2D model by compare the results with the ones arising from the simulation of a three-dimensional device. In fact, some differences are expected, due to the friction of air and water on the walls that close the caisson in the transverse direction.

7. Simulation of a full-scale REWEC3 device

7.1 Numerical domain description

A 2D CFD method, similar to the ones applied for the analyses carried out on scaled REWEC1 devices, has been used for investigate the interaction of waves with a full-scale REWEC3 breakwater. The computational domain is composed by a wave-flume, having a piston-type wave-maker placed in the left extremity and a REWEC3 breakwater in the right extremity of the numerical domain (see Fig. 7.1-1). The 2D wave flume is 1 km long and 30 m high. The length of the flume has been chosen in order to have many wavelengths, generally at least 10, between the wave-maker and the breakwater. It allows the REWEC3 device to reach a steady operating condition under fully developed waves, before that waves reflected on the moving wall reach the breakwater.

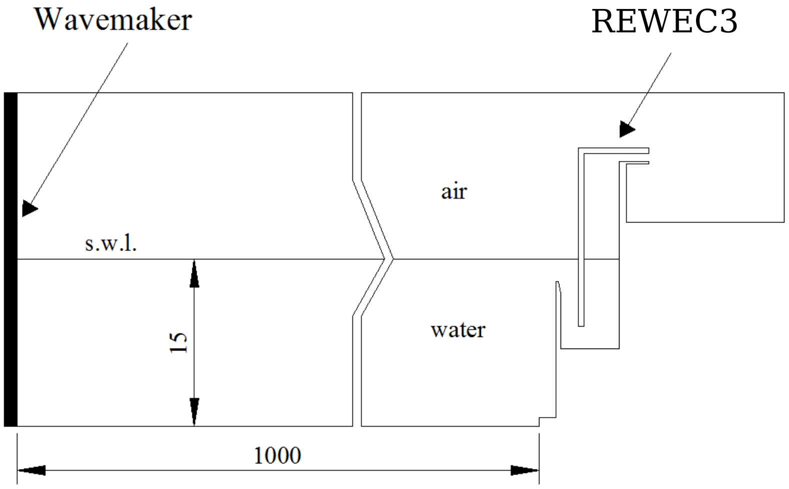

Fig. 7.1-1 Sketch of the computational domain (measures are in meter)

The REWEC3 plant has the same size of the plant installed at the Civitavecchia harbour of Rome (Italy) in the Tyrrhenian Sea. The plan view of the whole installation is shown in Fig. 7.1-2. As described in [Arena et al., 2015], the monitoring of the behaviour of the plants was made on 4 caissons (of 17) formed by cells independent each other.

The monitoring of the plant has been carried out under the twelve sea states, their characteristics are reported in Table 7.1-1. Supposing the waves moving perpendicularly to the REWEC3, a two-dimensional CFD simulation has been carried out, in order to reduce the computational effort and resources with respect to a full three-dimensional simulation. The dimensions of the cross section of the REWEC3 are shown in Fig. 7.1-3. As we can see, the plenum chamber is 3.2 m wide and the vertical duct 1.6 m, having an opening 2m width. The still water depth is 15 m. The conduit, in which a Wells turbine is placed as PTO-system, has a diameter of 0.75 m. In particular, the pressure drop in this region, induced by the presence of the turbine in the real case, has been reproduced by a porous zone in the CFD model.

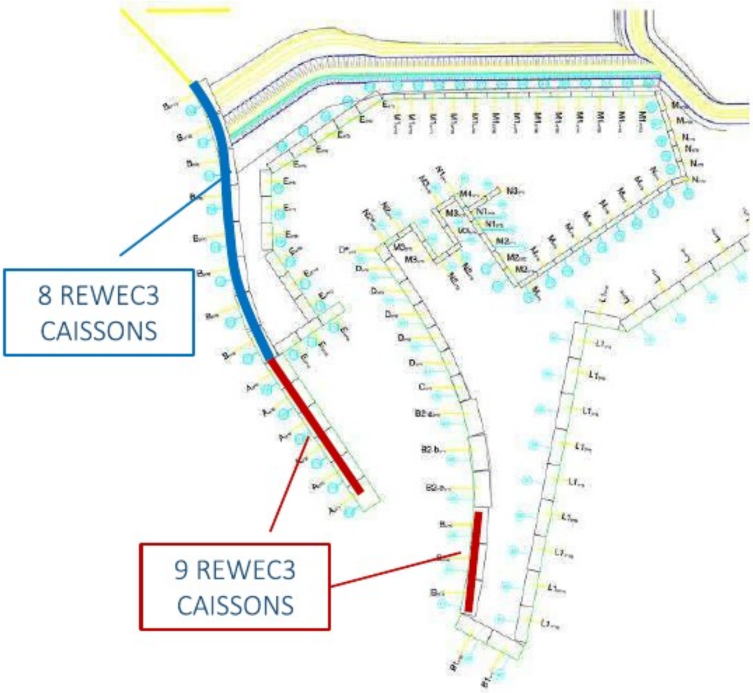

Fig. 7.1-2 Plan view on the location of the REWEC3 devices in Civitavecchia harbour (Italy)

Table 7.1-1 Specific wave height, H_s, and period, T_p, of the sea states registered during the monitoring of the REWEC3 devices

Sea State	**H_s [m]**	**T_p[m]**
1	0.5	3.0
2	1.0	4.3
3	1.5	5.2
4	2.0	6.0
5	2.5	6.7
6	3.0	7.4
7	3.5	8.0
8	4.0	8.5
9	4.5	9.0
10	5.0	9.5
11	5.5	10.5
12	6.0	10.4

A hybrid mesh has been used for the spatial discretization of the computational domain (see Fig. 7.1-4), formed by rectangular elements in the overall length of the flume and by triangular elements near the breakwater. The mesh has approximately 300,000 cells.

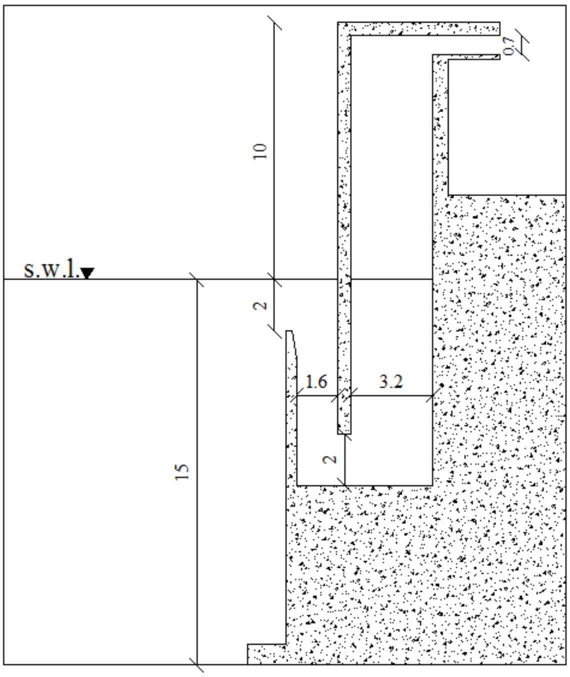

Fig. 7.1-3 The cross section of the caisson of the breakwater converter installed at Civitavecchia Harbour (measures are in meter).

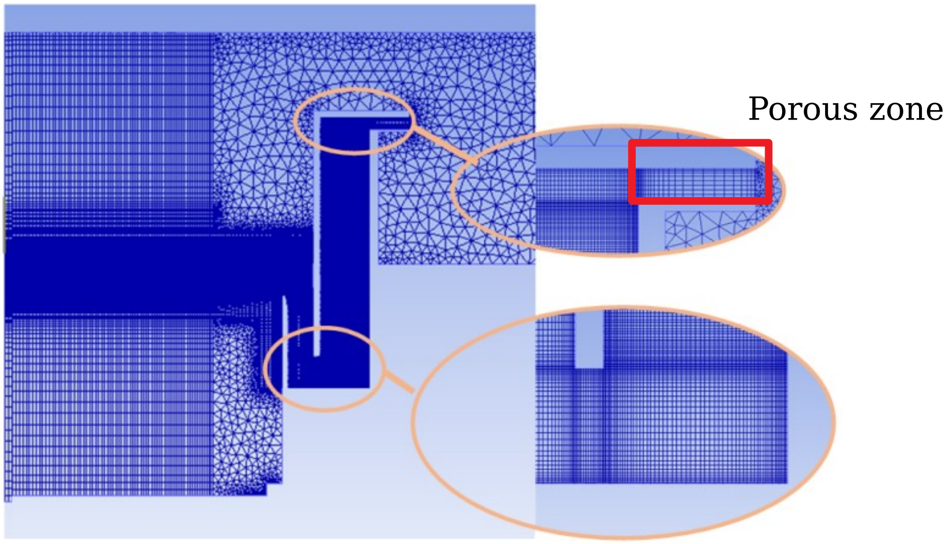

Fig. 7.1-4 The spatial discretization of the computational domain.

Starting from the water at rest, the wave generation process has been simulated assigning a sinusoidal motion to the left wall of the wave flume, by means of a User Defined Function (UDF). The maximum displacement of the piston type wave-maker has been calculated in accordance with the method used in the simulation of the scaled REWEC1 breakwater (section 4.8).

The part of the computational domain indicated by a red rectangle in Figure 7.1-4, has been set as “porous zone” in order to model the pressure difference between the chamber and the external ambient due to the oscillating flow.

7.2 Results: deep insight into the flow field and evaluation of energy losses and power output

The numerical model used in the simulation of the REWEC1 devices has been applied to the case of a full scale REWEC3 plan. It has been carried out a numerical simulation assigning a sinusoidal motion to the left wall of the wave flume described in Fig. 7.1-1, in order to reproduce a wave train with height H= 3.5 m and period T = 8s. The wave motion reproduced the see sea state 7 in Table 7.1-1. According to Hughes [Hughes S.A., 1993], the free surface displacement produced in a wave flume by a piston-type wave-maker starting from rest and moving sinusoidally for a given period of time t, can be expressed as:

$$\eta(x,t)=\frac{2}{\pi}\int_0^\infty \frac{\tanh kd}{k}\cos kx\left[\int_0^t U_0(\tau)\cos\sigma(t-\tau)\,d\tau\right]dk \qquad (7.2\text{-}1)$$

where U_0 is the horizontal velocity of the wave board, and $\sigma^2 = g\ k\ \tanh(kd)$, where $k = 2\pi/\lambda$, being λ the length of the flume, and finally d is the flume depth.

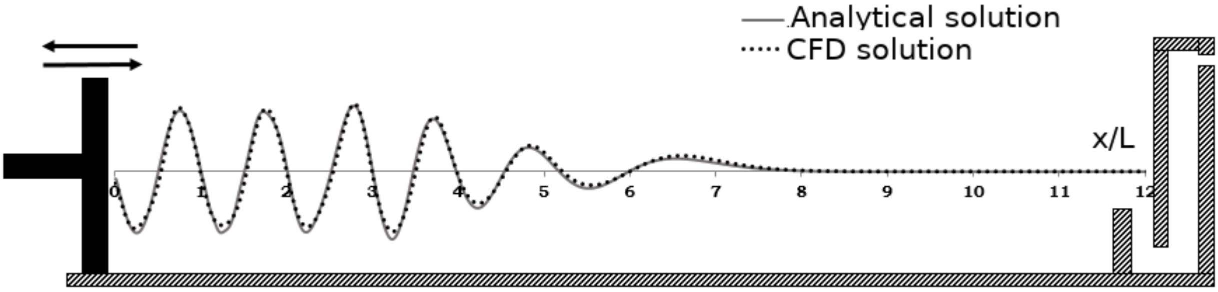

Fig. 7.2-1 Free surface displacement as function of relative distance x/L, where L represents the wavelength. Comparison between analytical solution (continuous line) and the numerical solution (dotted line) carried out by CFD simulation (H =3.5m, T=8s).

To test the wave generation and propagation in the flume, the values of η(y,t) registered during the CFD simulation have been compared with the analytical ones. Figure 7.2-1 shows the instantaneous free surface elevation along the flume, at a fixed time instant after the beginning of paddle motion. For comparison, the analytical solution (Eq. 7.2-1) is shown too. As we can see, there are a good agreement between the two data.

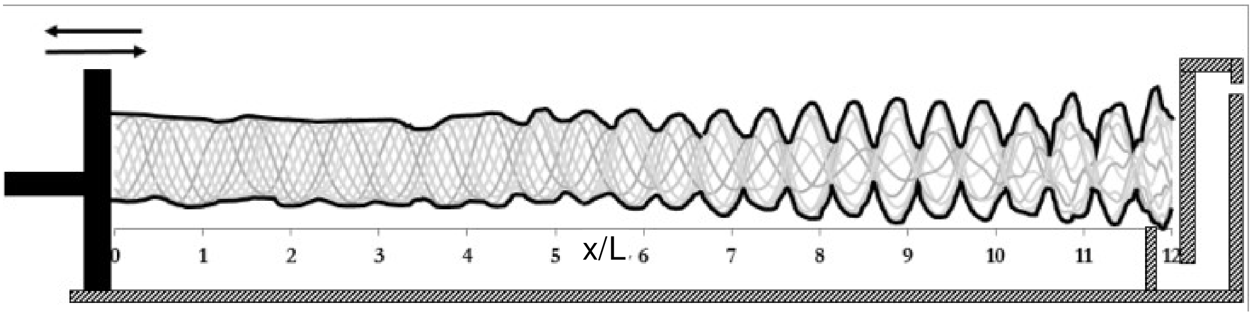

Fig. 7.2-2 Overlapping of several snapshots of the flume surface during a wave period as function of x/L. In marked line is represented the envelope of the quasi-standing field.

The wave field in front of the absorber breakwater is produced by the interaction between the incoming waves and the pulsating discharge through the plant. Figure 7.2-2 shows the overlapping of several snapshots of the surface waves in the flume in which each frame is taken every 1/20*T*, during a wave period. As we can see, the flow field in front of the REWEC3 breakwater is quite different from the standing wave field in front of a vertical reflecting wall.

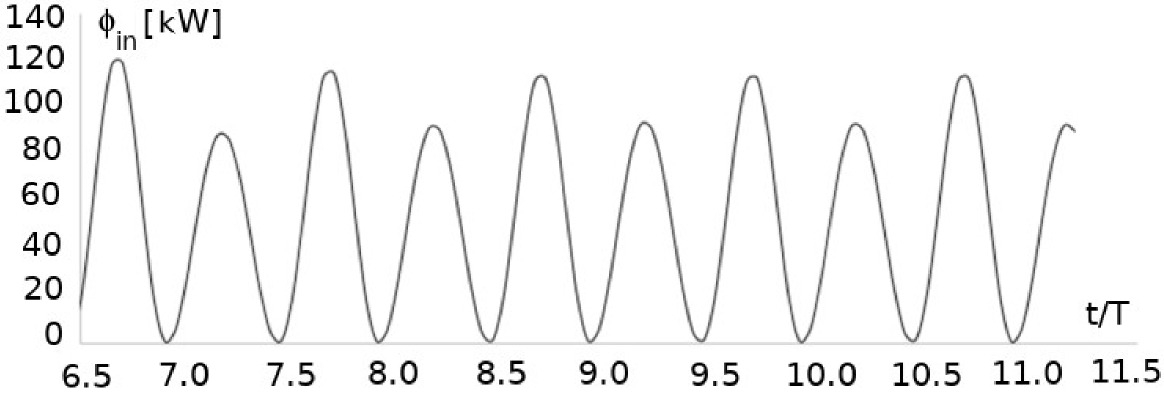

Fig. 7.2-3 The energy flux of the incident waves measured at a fixed vertical section along the wave flume.

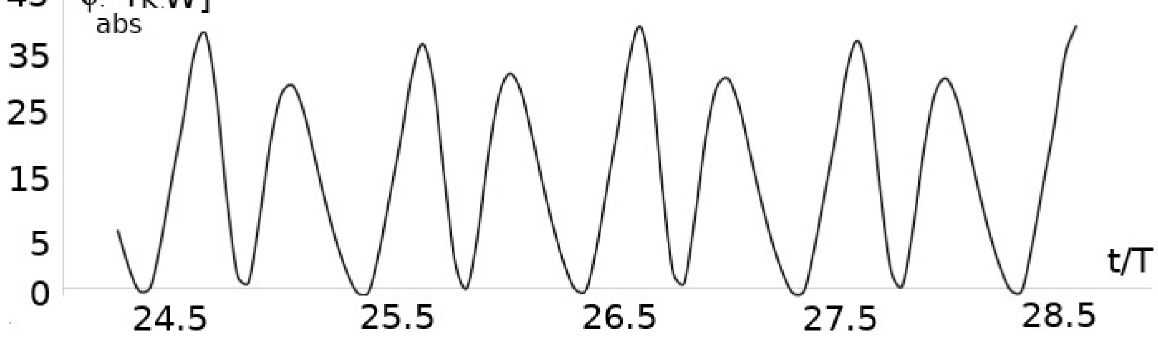

Fig. 7.2-4 The energy flux crossing the outer opening of the vertical duct of the U-OWC breakwater.

The “quasi-standing” wave field is characterized by the presence of “quasi-nodes”, which are points where the amplitude of η is at its minimum but different from zero. Moreover, when the incident wave train has impacted the absorber-breakwater, the wave amplitude at the breakwater wall is smaller than in front of a vertical reflecting wall. Indeed, the amplification factor (= wave amplitude at the REWEC3 breakwater wall / 2H) is 0.85.

In order to verify the share of the incident wave flux absorbed by the U-OWC, we calculated the energy flux in different sections along the wave flume. Figure 7.2-3 shows the instantaneous energy flux of the incident waves, ϕ_{in}, evaluated at two wavelength far from the wave-maker. The mean energy flux of the incoming waves train (i.e. the waves generate by the wave-maker) is approximatively equal to 52.1 kW/m.

The instantaneous energy flux absorbed by the plant, ϕ_{abs}, measured at the outer opening of the vertical duct, is shown in Fig. 7.2-4. The time average energy flux absorbed by the plant is about 16.9 kW/m that is about 32% of the incoming wave energy flux. Such plant performance depends on the resonance conditions. A useful index to check how close to resonance the plant is working is the resonant coefficient R (see [Boccotti, 2012]). It is calculated starting from the phase difference between the water discharge Q and the fluctuating wave pressure at the outer opening of the plant, Δp, shown in Fig. 7.2-5. Values of R less than zero mean that the wave period is higher than the eigenperiod, whereas values grater than zero mean that the wave period is less than the eigenperiod. Values close to 0 mean that the plant is close to resonance. For this sea state the resonant coefficient is -0.25.

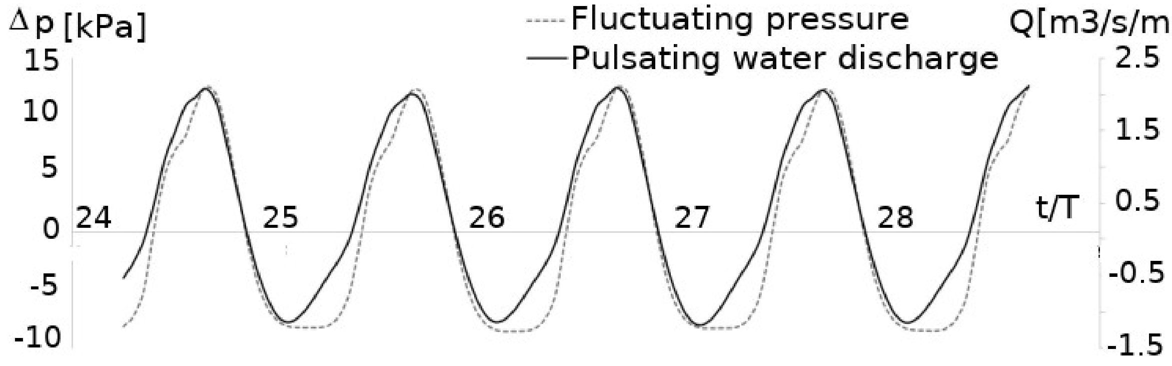

Fig. 7.2-5 Pressure fluctuation p at the outer opening and discharge Q in the plant, as a function of t/T. [The Q is positive if water enters the plant.].

Referring to the scheme of Fig. 7.2-6, the mean energy flux crossing the horizontal sections (A-A) and (B-B) was calculated, in order to evaluate the energy flux lost in the water flow. As we can see in Fig. 7.2-7 the instantaneous energy flux on section B-B assumes more negative values than the energy flux on the section A-A and then the mean energy flux is about 30% lower than the mean energy flux on the section A-A. In average, this decrease is due to the minor losses and the continuous losses in the vertical duct and in the chamber. In order to validate the numerical experiment, we carried out some preliminary checks on the flow field inside the chamber.

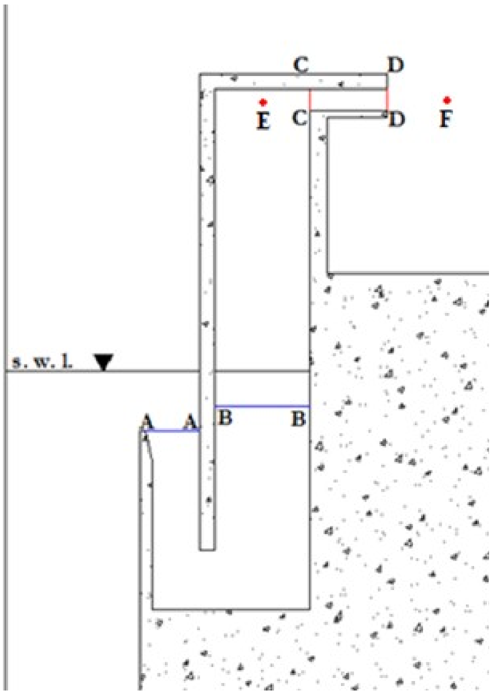

Fig. 7.2-6 Reference scheme of the horizontal sections (A-A, B-B), vertical sections (C-C, D-D) and points where pressure has been measured (E,F).

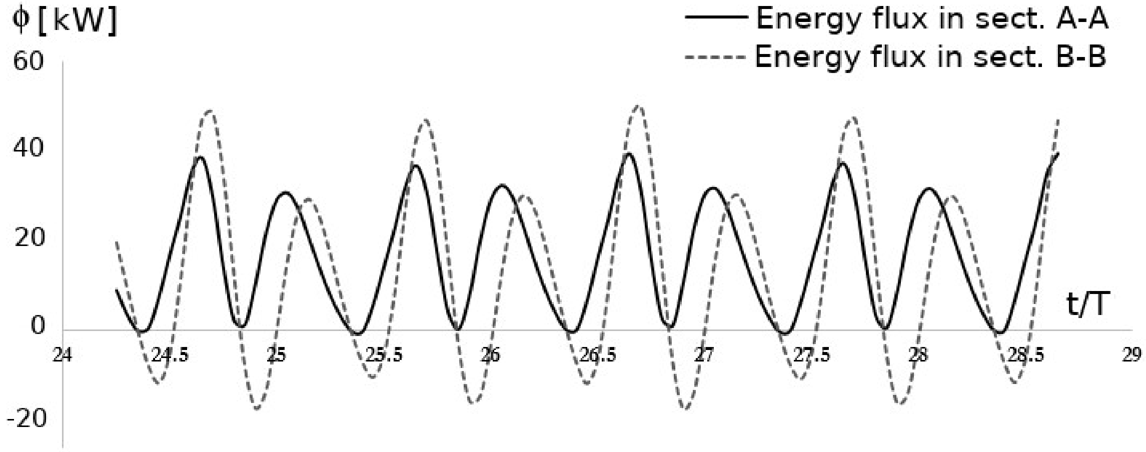

Fig. 7.2-7 The energy flux measured in the horizontal sections (A-A) and (B-B), shown in Fig. 7.2-6.

Fig. 7.2-9 shows the water volumetric flow rates measured at the outer opening of the vertical duct (section A-A in Fig. 7.2-6) and inside the chamber (section B-B in fig. 7.2-6) just below the air-water interface. As we expect, the two volumetric flow rates coincide for almost each instant of time, as the water flow is incompressible. Some negligible differences result when the flow rates are negative, representing the occurrence of outflow from the device. In fact in this case, the volumetric flow rate recorded at section A-A may be affected by the vortex on the vertical duct outer opening (Fig. 7.2-10 and Fig. 7.2-11). A check has been also done for the mass flow rate across the porous medium (equivalent to the air turbine) in Fig. 7.2-9.

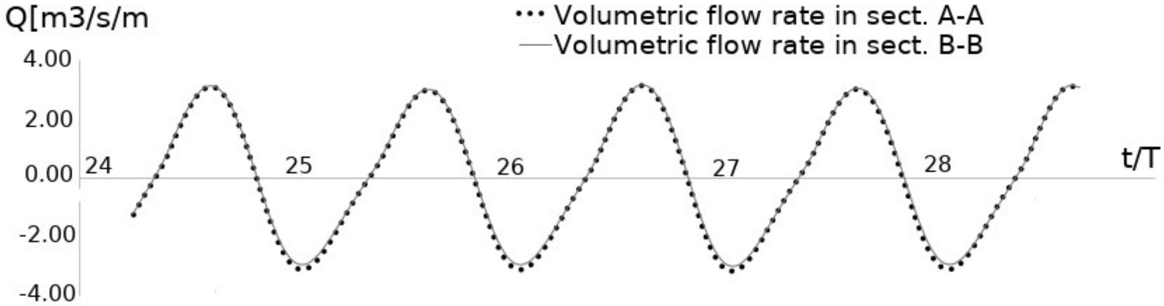

Fig. 7.2-8 Comparison between the volumetric flow rate measured in sections (A-A) and (B-B), shown in Fig. 6.2-6.

CFD simulation allows to perform a detailed analysis of the streamlines within the U-OWC device. Figures 7.2-10 and 7.2-11 show the streamlines at the occurrence of maximum water inflow and maximum outflow from the device, respectively. In Fig. 7.2-10 and 7.2-11, the free water surfaces inside the device chamber and inside the wave thank are represented by the thick blue line.

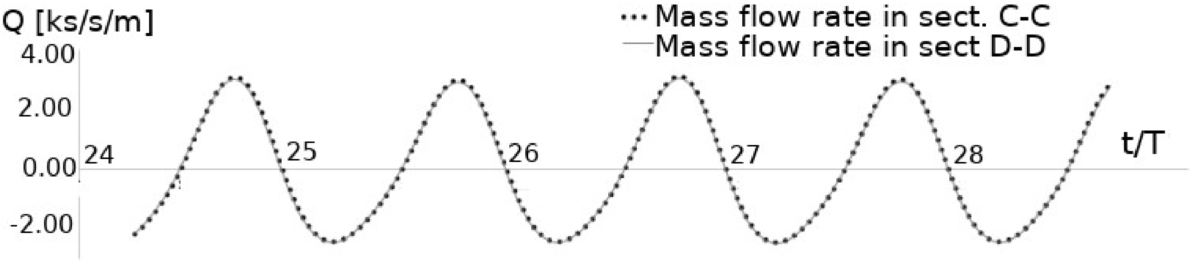

Fig. 7.2-9 Comparison between the mass flow rate measured in sections (C-C) and (D-D), shown in Fig. 7.2-6.

As we can see in 7.2-10, vortexes are generated near the vertical duct mouth, near the lower opening of the chamber and near the roof of the chamber. These vortexes cause energy dissipation inside the device, reducing the amount of energy suitable for the turbine conversion. Also in Fig. 7.2-11 we can see the presence of vortexes, which in this case are in larger number and bigger. During the simulation, both values of pressure inside the chamber and in the atmosphere have been registered. The measurement have been carried out in point E and F (Fig. 6.2-6), in order that the pressure drop $\Delta p = p_E - p_F$ represents the pressure drop of the air flowing through the porous media.

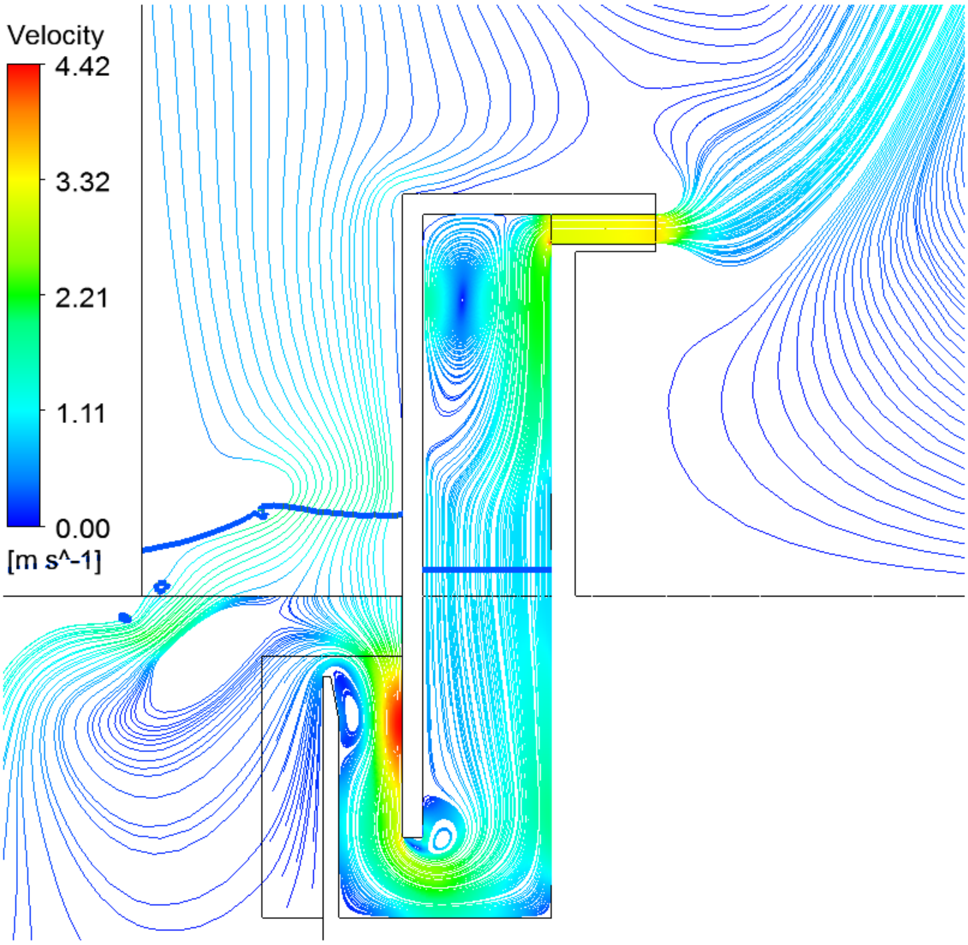

Fig. 7.2-10 Streamlines inside and near the U-OWC device registered at the occurrence of maximum water inflow into the device, a), and at the occurrence of maximum water out-flow, b).

Fig. 7.2-12 shows the values of Δp in the time domain. In the porous media the viscous losses (representing the pressure drop across the Wells turbine) prevail over the inertial ones which represent minor and continuous losses in the turbine air duct). This is clearly highlighted in Fig. 7.2-13 that shows a linear relationship between the pressure drop, Δp, and the velocity, v_p, inside the porous medium. The value of the linear proportionality coefficient between Δp and v_p arising from the simulation and showed in Fig. 7.2-13, is the same as that assumed as an input in the porous media model (see eq. 4.3-11), (which is equal to R_v multiplied for μ_a and Δl).

The product of Δp by the volumetric flow Q in the porous media is the instantaneous energy rate ϕ_{pm} (Fig. 7.2-14) dissipated per time unit through the porous medium. On the basis of the presented “equivalent model” to the actual air duct hosting the Wells turbine, ϕ_{pm} represents the pneumatic power available for the air turbine per meter of width of the U-OWC. Therefore, from ϕ_{pm} and neglecting minor and continuous losses in the air duct, the pneumatic power P_p available for a single turbine can be obtained by multiplying the value of ϕ_{pm} by the width of the air chamber which the turbine is connected to.

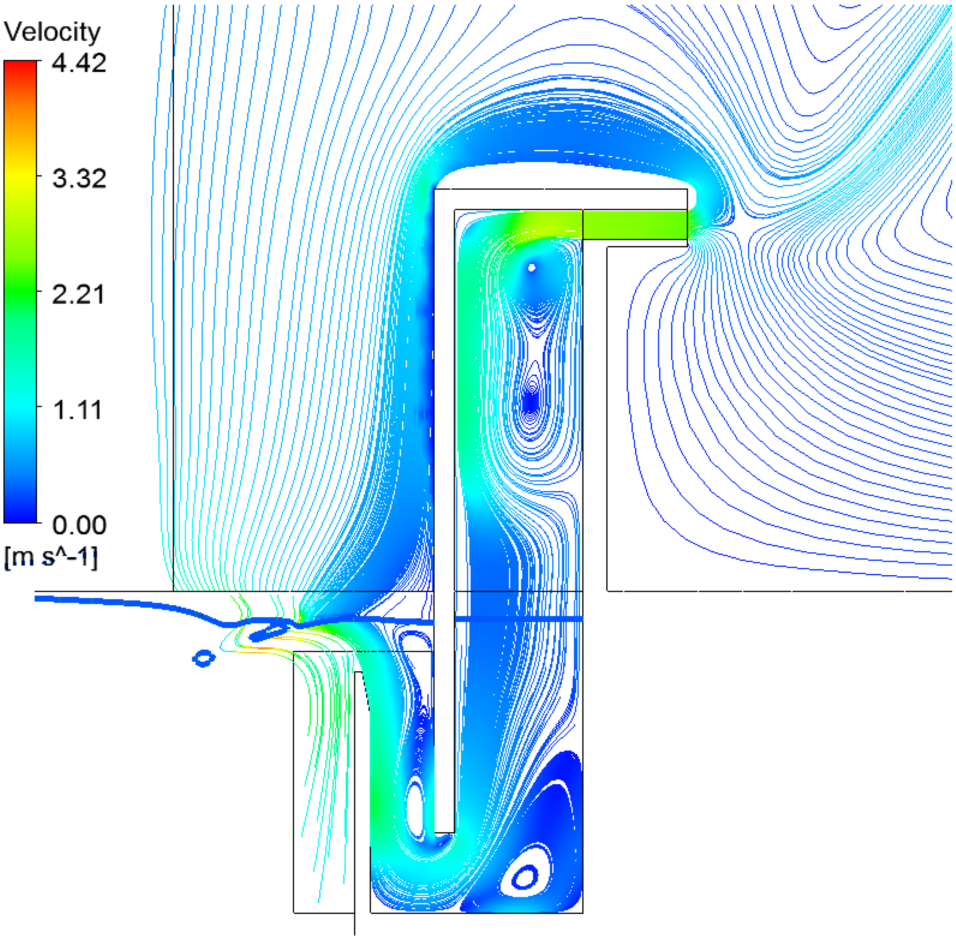

Fig. 7.2-11 Streamlines inside and near the U-OWC device registered at the occurrence of maximum water inflow into the device, a), and at the occurrence of maximum water outflow, b).

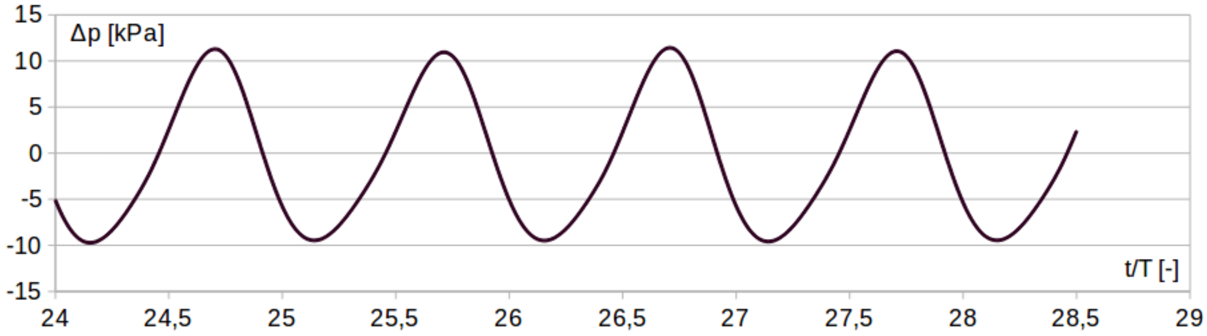

Fig. 7.2-12 Pressure drop through the porous medium.

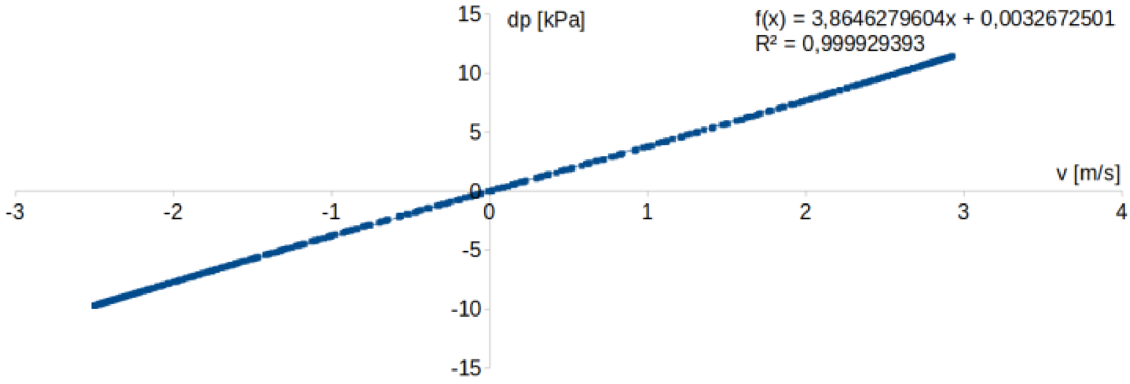

Fig. 7.2-13 Pressure drop through the porous medium as a function of the air velocity

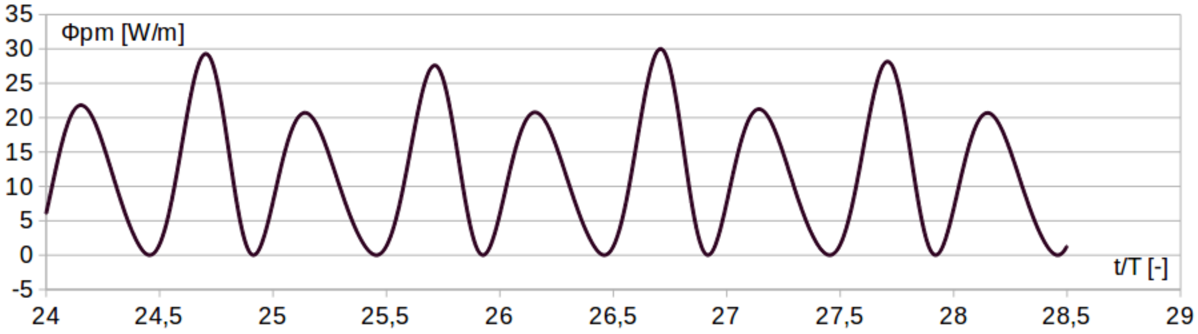

Fig. 7.2-14 The rate of energy dissipated inside the porous medium

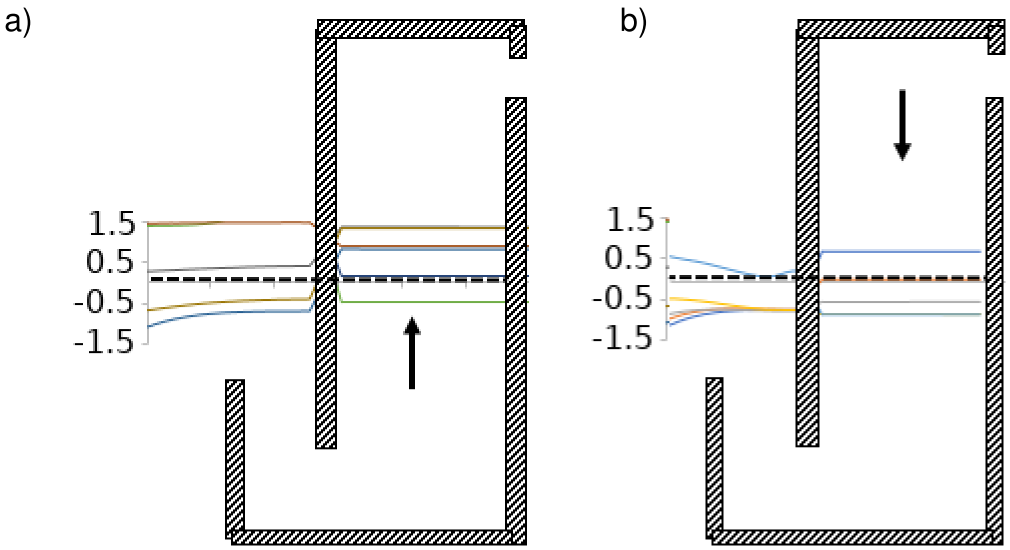

Fig. 7.2-15 Free water surface level inside and outside the chamber at different time instants. Dotted line is the mean water level at rest.

The peak values of ϕ_{pm} observed during outflow are higher than those observed during inflow (see Figures 7.2-9 and 7.2-12). The mean value of ϕ_{pm} is equal to 11.94 kW. Figure

19 shows the free water surface inside the device chamber at different time instants. In particular, Figure 7.2-15a refers to the water outflow phase, while Figure 7.2-15b refers to the inflow phase. As we can see, the surface is always horizontal, regardless of the time instant. This result supports the use of 1D analytical models for estimating U-OWC performances [Boccotti, 2012].

Figures 7.2-15a and b also show that oscillations in the room are not symmetrical in respect to the rest condition. In fact, the maximum raising of the free water level is 1.43 m compared to the rest level, whereas the maximum lowering is just 0.5 m.

7.3 Discussion: possible improvements

The simulation results show that the porous medium zone has produced the same pressure losses of the equivalent Wells turbine, then the implementation of the porous medium result effectiveness for the simulation of PTO systems in REWEC devices

Also in this case, it could be analysed the accuracy of the proposed 2D model by compare the results with the ones arising from the simulation of a three-dimensional device. Because of the large number of cells composing the numerical domain, in the case of the simulation of a three-dimensional case High Performance Calculation (HPC) is needed due to the computational effort required.

Finally, an analysis of the performances of REWEC3 breakwaters outside their design wave, i.e. outside the resonant conditions could be carried out. It could provide “performance maps” of REWECs in all sea states, to understand the sea energy production capability of such concepts in all sea states.

8. Suggestions for further works: analysis of floating wave energy devices

As a future work, the CFD modelling can be applied to the simulation of floating objects under waves. In particular, REWEC devices can be integrated into the floating platform of Floating Off-shore Wind Turbines (FOWT). This solution can give two advantages: the production of energy either from both wind and waves, or only from one if only one of the two is available; the smoothing of the oscillation of the FOWT platform, improving the incident flow to the air turbine.

During the research period at the School of Water, Energy and Environment (SWEE) of the Cranfield University, a simplified 2D model has been tested for the simulation of a floating box under waves. The CFD model has been validated against: experimental and numerical (potential theory) results [Koo W.C. and Kim M.H., 2004] and previous CFD results [Luo Y. et al., 2014]. The numerical domain had the same geometry of the 2D schematics reported in Fig. 8-1. The incident wave characterised by two parameters, ξ=0.25 and λ=6.2831, (see [Koo W.C. and Kim M.H., 2004] has been simulated.

Fig 8-2 shows the main settings of the computational domain. The edge on the left has been set as a moving wall, in order to generate the wave motion by means of a UDF (see section 4.8).

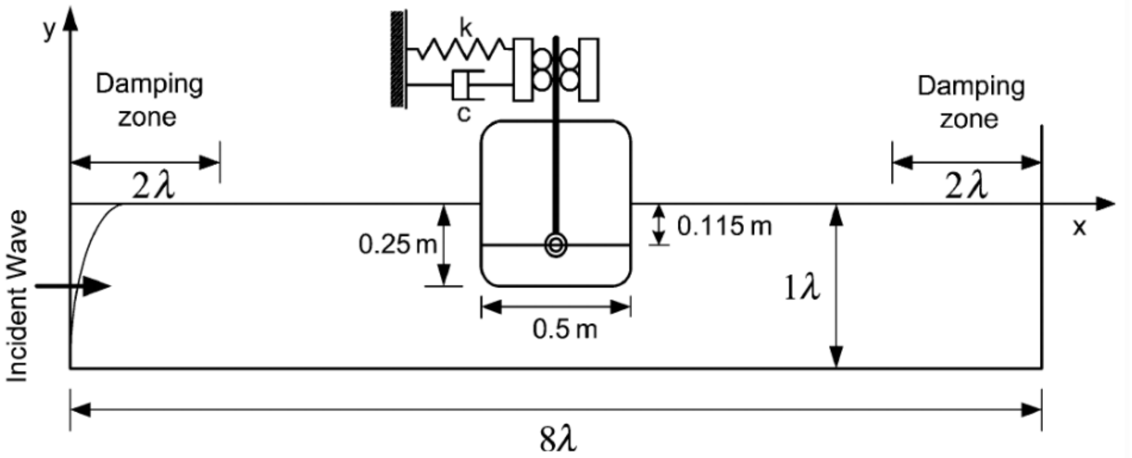

Fig. 8-1: Schematics of the experimental rig reproduced in the CFD simulations

The upper edge has been set as pressure outlet (gauge pressure = 0, with respect to the operative pressure equal to the atmospheric pressure). The edge on the right, corresponding to the opening of the numerical domain, has been set as pressure outlet. An open channel boundary condition has also been set here, in order to impose that during the simulation the water level on this edge remain equal to the still water level. Actually, in the aim of reducing waves reflection on the ending edge of the domain, the part of the domain adjacent to the right edge has been set as a numerical dissipation zone, activating the numerical beach option. The linear damping resistance was 10 [1/s] and the quadratic damping resistance was 10 [1/m]. The other edges, including the floating body ones and the bedside, have been set as no slip walls.

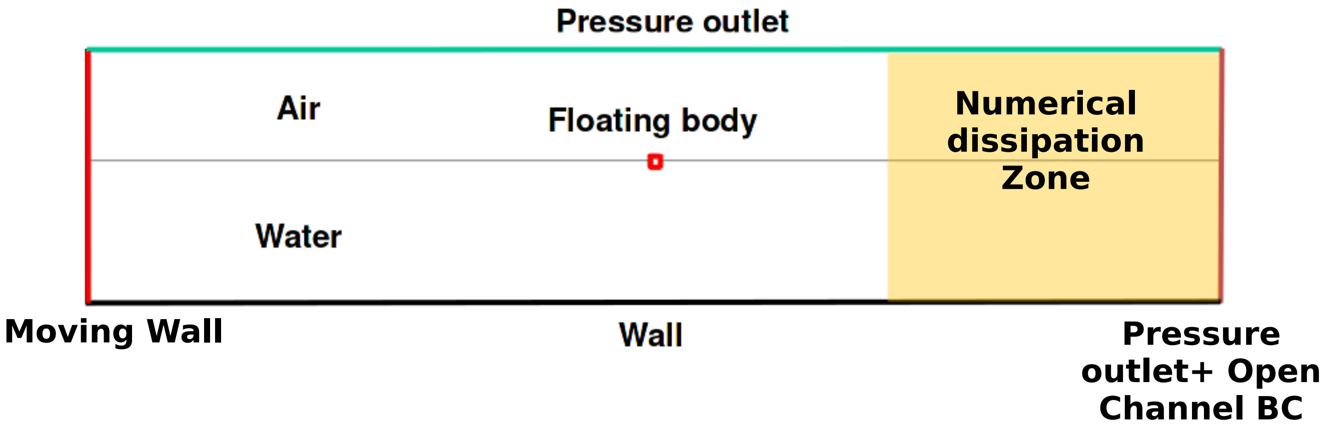

Fig. 8-2: The numerical domain

Two meshes have been developed, in order to analyse the grid dependency. The fine mesh had 156,000 cells (see an enlargement in Fig 8-3), whilst the coarse mesh 68,000 cells (see an enlargement in Fig 8-4).

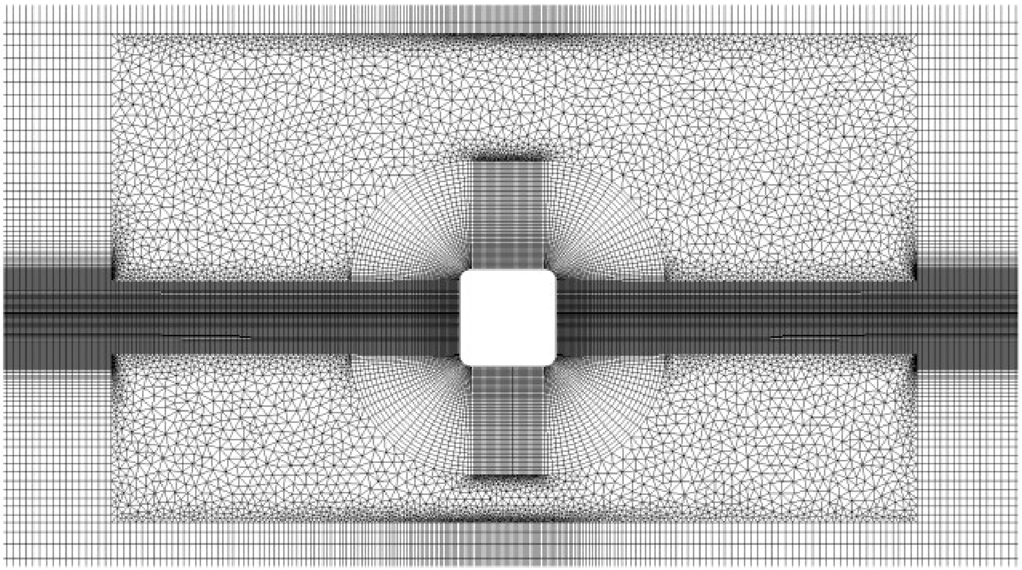

Fig. 8-3: Enlargement of the fine-mesh (156,000 cells)

Regarding the CFD settings, unsteady compressible RANS equations have been calculated including turbulence by means of the k-ω turbulence model. The Eulerian VOF Model has been used for taking into account the two-phase (water/air) interaction. Pressure and velocity fields have been calculated using the Semi Implicit Pressure-Linked Equations (SIMPLE) algorithm. Regarding the spatial discretization schemes, the Geo-Reconstruct scheme has been used for the Volume Fraction equation, the PREssure STaggering Options

(PRESTO!) scheme for the pressure, and the 2nd order upwind for the momentum. The time step of the simulation was one thousandth of the waves period.

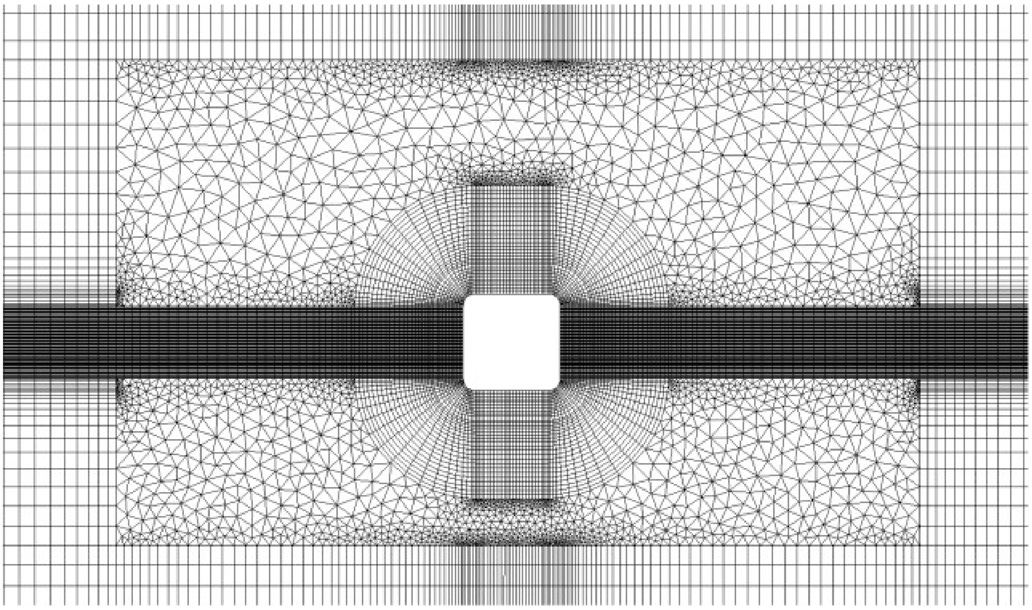

Fig. 8-4: Enlargement of the coarse mesh (68,000 cells)

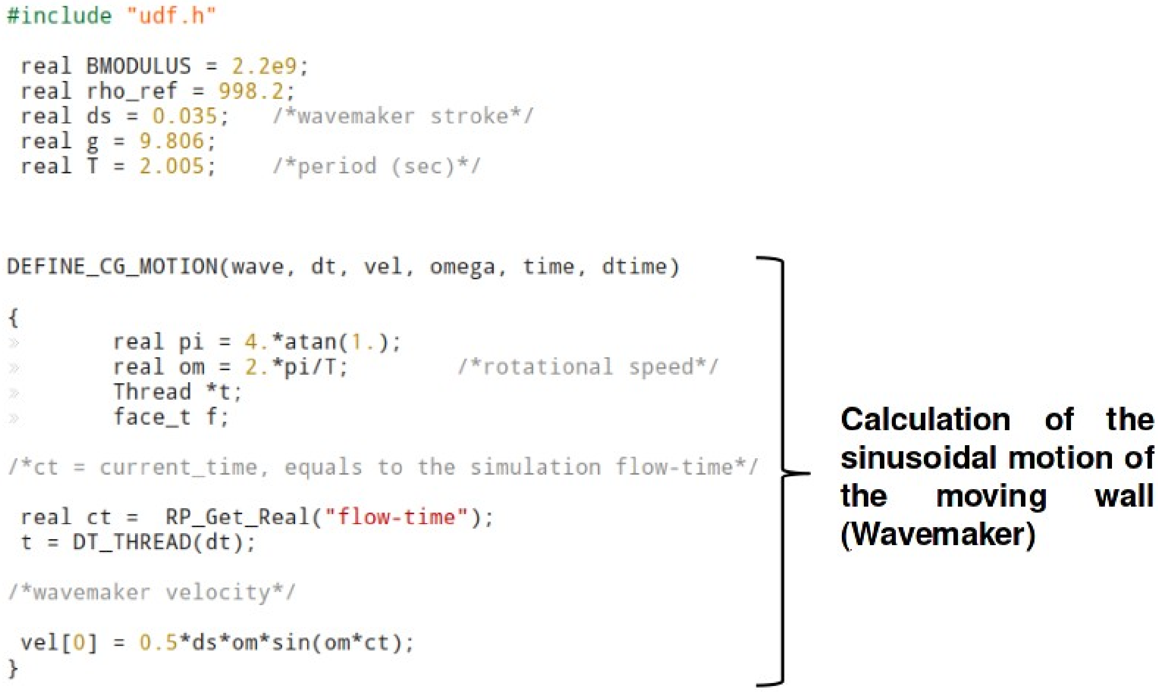

```
#include "udf.h"

 real BMODULUS = 2.2e9;
 real rho_ref = 998.2;
 real ds = 0.035;   /*wavemaker stroke*/
 real g = 9.806;
 real T = 2.005;    /*period (sec)*/


DEFINE_CG_MOTION(wave, dt, vel, omega, time, dtime)

{
»       real pi = 4.*atan(1.);
»       real om = 2.*pi/T;          /*rotational speed*/
»       Thread *t;
»       face_t f;

/*ct = current_time, equals to the simulation flow-time*/

 real ct =  RP_Get_Real("flow-time");
 t = DT_THREAD(dt);

/*wavemaker velocity*/

 vel[0] = 0.5*ds*om*sin(om*ct);
}
```

Calculation of the sinusoidal motion of the moving wall (Wavemaker)

Fig. 8-5: UDF: calculation of the motion of the moving wall

The Six DOF model, available in the Fluent solver, has been used for the calculation of the floating body motion from the pressure forces on the body. The Implicit Update of the mesh (each time step) has been used for improving the solution stability. As reported in Fig 8-5 and Fig. 8-6, UDF has been used for four different purposes: calculation of the sinusoidal motion of the moving wall (Wave-maker), calculation of the water density, calculation of the water speed of sound, calculation of the floating body motion.

Considering the simulations results, the comparison between the free water level coordinates resulting from the fine mesh and from the coarse one showed a little difference of the generated waves heights (coarse mesh waves heights were smaller then fine mesh ones), as reported in Fig. 8-7. Actually, the structured part that contains the free water level is the same for both meshes, then it results only a little difference between the waves heights. In accordance with the fact that the incident wave heights were smaller, also the heights of the floating box oscillations result smaller in the case of the coarse mesh, as shown in Fig. 8-8.

The CFD model has been validated by compare the values of the ratio between the box oscillation height, H_b, and the incident wave height, H_i, to the ones reported in literature ([Koo W.C. and Kim M.H., 2004] and [Luo Y. et al., 2014]). Both values of the heights have been calculated as the average of the ones registered in the last three periods of the simulation. In both cases of the fine and the coarse mesh, it has resulted a good agreement between the simulation results and the previous CFD, numerical and analytical results, as reported in Table 8-1.

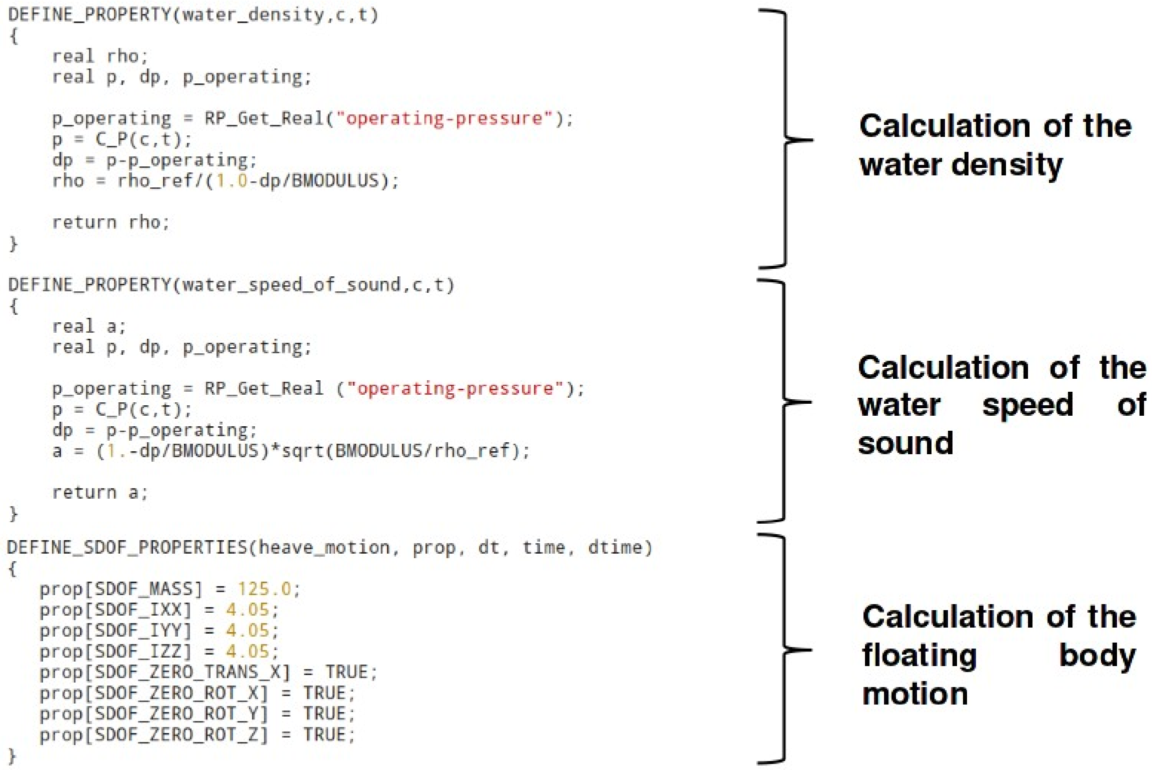

```
DEFINE_PROPERTY(water_density,c,t)
{
    real rho;
    real p, dp, p_operating;

    p_operating = RP_Get_Real("operating-pressure");
    p = C_P(c,t);
    dp = p-p_operating;
    rho = rho_ref/(1.0-dp/BMODULUS);

    return rho;
}
DEFINE_PROPERTY(water_speed_of_sound,c,t)
{
    real a;
    real p, dp, p_operating;

    p_operating = RP_Get_Real ("operating-pressure");
    p = C_P(c,t);
    dp = p-p_operating;
    a = (1.-dp/BMODULUS)*sqrt(BMODULUS/rho_ref);

    return a;
}
DEFINE_SDOF_PROPERTIES(heave_motion, prop, dt, time, dtime)
{
   prop[SDOF_MASS] = 125.0;
   prop[SDOF_IXX] = 4.05;
   prop[SDOF_IYY] = 4.05;
   prop[SDOF_IZZ] = 4.05;
   prop[SDOF_ZERO_TRANS_X] = TRUE;
   prop[SDOF_ZERO_ROT_X] = TRUE;
   prop[SDOF_ZERO_ROT_Y] = TRUE;
   prop[SDOF_ZERO_ROT_Z] = TRUE;
}
```

Fig. 8-6: UDF: calculation of the water density, of the water speed of sound and of the body motion

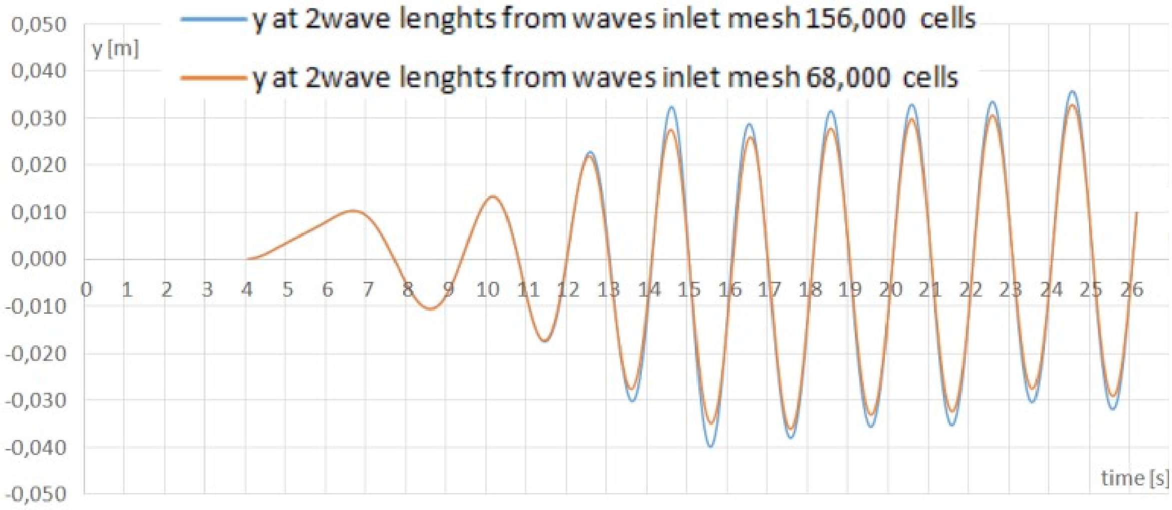

Fig. 8-7: Comparison between the the incident waves registered during the simulation of the fine mesh and of the coarse one.

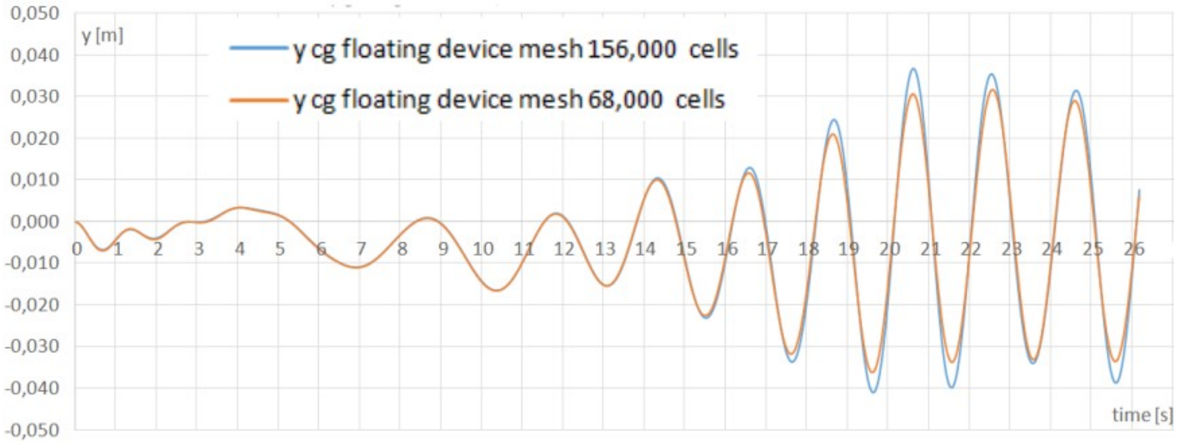

Fig. 8-8: Comparison between the values of the oscillations of the box centre of gravity (cg) registered during the simulation of the fine mesh and of the coarse one

Table 8-1 Values of the ratio H_b/H_i

	H_b/H_i
Fine mesh	1.085
Coarse mesh	1.056
Luo et al. (CFD)	1.038
Koo and Kim (Potential theory)	1.088
Analytic	1.104

Simulations have been carried out by means of the HPC sever GRID, available at the Cranfield University, using 32 processors used. In the case of the fine mesh, the average time to perform a time step has been of 19.7 s, whilst in the case of the coarse mesh of 10.2 s.

This preliminarily work can be improved simulating a more complicated geometry instead of a rectangular box, for example a floating REWEC device.

9. Main achievements and conclusions

An original CFD approach has been proposed for the analysis of the fluid-dynamics behaviour of both REWEC1 and REWEC3 breakwaters. A 2D CFD model has been applied to the simulation of the waves interaction with a scaled REWEC1 breakwater, placed into a numerical wave tank. Wave breaking occurred after the waves impacted the device, dissipating energy and reducing the amount of transmitted wave energy downstream the device; therefore the REWEC1 breakwater proves to be a good system for protecting coast as well as for energy absorption.

The value of the absorption coefficient resulted low, in accordance with the lack of energy dissipated inside the REWEC1 (no turbine or other dissipative device were present). In order to reduce the energy dissipation into the device, the analysis of the dynamics of the water flow inside the caisson proved the importance of design refinements of the upper and lower opening of the duct in respect to the simplified geometry of the considered numerical domain. Another significant aspect arising from the flow-dynamics analysis has been that the water flow into the duct is directed for almost the whole length of the duct along the y-axis, in accordance with the 1D hypothesis in the analytical model.

Considering these promising results, the numerical domain adopted in this analysis will be reproduced for an experimental analysis, which will allow a further verification of the absorption capability of the REWEC1. Moreover, it has been proposed and tested a numerical technique able to be used for a further development: the evaluation of the absorption coefficient of a REWEC1 which encloses an energy absorption device.

In this work, in order to evaluate the capability of the CFD unsteady simulations to reproduce the unsteady flow conditions of OWC systems, a scaled experimental device has been considered, which is able to generate oscillations in a broad range of frequencies. Furthermore, an analytical model is proposed, which give fairly good results, in particular when the system registers small oscillations.

Focusing on the verification of the ability of REWEC1 to operate under resonance conditions, an experimental REWEC1 device has been simulated by means of the presented CFD model. The CFD simulations showed a good agreement with experiments, within the examined frequency range. Time plots of pressure level in the bottoming caisson, reproducing the REWEC1 device, were well reproduced and also the peak frequency has been well captured. In particular it has been shown that it is necessary to perform the simulations including a turbulence model (in this case the standard k-ω model).

Finally, as shown by the comparison with the experimental tests, the use of the proposed CFD model, which implements the standard k-ω turbulence model, can be considered a good alternative to the set up of an experimental rig.

The proposed CFD model has been also applied on the analysis of the interaction between a REWEC3 device and incident waves, for what concerns both the external wave field and the air and water flow inside the device. First, the generation of a periodic wave train within a numerical wave tank has been carried out, and the mechanics of generated waves have been accurately checked by comparison with literature and analytical results. The wave period of the simulated waves is greater than the eigenperiod of the REWEC3, being the resonant coefficient R is equal to -0.25 (R=0 means resonance). Therefore, the energy absorption has been about 32% of the incoming wave energy flux.

The analysis of the streamlines inside the device highlighted the need to improve the design of both the vertical duct upper opening and the U-duct to limit fluid dynamics losses. Indeed, about 30% of the absorbed wave energy is wasted in losses in water flow while 70% is available as pneumatic power for the turbine.

Finally, the porous medium model adopted as “equivalent model” of the air turbine in 2D CFD simulations worked successfully. It has been verified that the equivalent linear viscous losses in the porous medium, related to the turbine operation, are greater than continuous and minor head losses.

The 2-D CFD model adopted in this work permits to set up 1-D numerical model suitable to match the plant characteristics and the PTO system with the local wave climate of the plant. Once fixed main parameters, the 2D CFD proves to be a useful tool to improve the plant performance by optimizing the plant geometry and fine tuning it with waves.

Acknowledgements

For the development of this thesis the author would like to thank:

- Dipartimento di Meccanica, Matematica e Management (DMMM) of Politecnico di Bari: my supervisors Prof S. M. Camporeale and Prof. M. Torresi, all the colleagues met.
- Dipartimento di Ingegneria Civile e Ambientale (DICEAM) of Università Mediterranea di Reggio Calabria: Prof. F. Filianoti and Dr. Luana Gurnari.
- School of Water, Energy and Environment (SWEE) of Cranfield University: Prof. Maurizio Collu and Prof. Taka Nishino.

Bibliography

Aqua-RET, 2017, Tidal Stream - European Resource Map. Available at: www.aquaret.com/indexcd1b.htmloption=com_content&view=article&id=112&Itemid=255&lang=en.

Arena F., Fiamma V., Laface V., Malara G., Romolo A. and Strati F.M., 2015, Monitoring of the U-OWC under contruction in Civitavecchia (Rome, Italy), Proceedings of the 11th European Wave and Tidal Energy Conference (EWTEC), 6-11 September 2015, Nantes, France

Barstow S., Mørk G., Mollison D. and Cruz J., 2008, The Wave Energy Resource. In: Cruz J. (eds) Ocean Wave Energy. Green Energy and Technology (Virtual Series). Springer, Berlin, Heidelberg

BNEF, 2015, Levelised Cost of Electricity Update for the second half of 2015

Boake C.B., Whittaker T.J.T., Folley M. and Ellen, H., 2002, "Overview and Initial Operational Experience of the LIMPET Wave Energy Plant", Proceedings of the International Offshore and Polar Engineering Conference, pp. 586.

Boccotti P., 1998, Caisson for absorbing wave energy, PCT and US Patent No. 6,450,732 B1.

Boccotti P., 2012, "Design of breakwater for conversion of wave energy into electrical energy", *Ocean Engineering,* vol. 51, pp. 106-118

Boehlert G.W. and Andrew B.G., 2010, " Environmental and ecological effects of ocean renewable energy development: a current synthesis.", Oceanography, 23, no. 2, pp.: 68-81. http://www.jstor.org/stable/24860713.

BP plc, 2017, BP Statistical Review of World Energy,, London (UK), June 2017

Camporeale S.M. and Filianoti P.G.F., 2008, Energy conversion of OWC devices with additional vertical ducts, Proceedings of the 27th International Conference on Offshore Mechanics and Arctic Engineering, OMAE 2008 Estoril, Volume 6, Pages 739-750, Portugal, 15-20 June 2008

Camporeale S.M., Filianoti P.G.F., 2008, *Energy conversion of OWC devices with additional vertical ducts*, 27th International Conference on Offshore Mechanics and Artic Engineering, OMAE 2008, Berlin, Germany, 9-13 June 2008, code 76693

Camporeale S.M., Torresi M., Pascazio G. and Fortunato B., 2003, A 3D unsteady analysis of a Wells turbine in a sea wave energy conversion device, Proceeding of ASME Turbo Expo, Atlanta, Georgia, USA

Carcas M.C., 2003, "The OPD Pelamis WEC: Current status and onward programme (2002)", *International Journal of Ambient Energy,* vol. 24, no. 1, pp. 21-28.

CEC, 1996, Wave Energy Project Results: The Exploitation of Tidal Marine Currents. - DGXII - Report EUR16683EN, Commission of the European Communities, Brussels, Belgium.

Charlier R.H., and Justus J.R., 1993, Ocean Energies: Environmental, Economic and Technological Aspects of Alternative Power Sources., Amsterdam, The Netherlands: Elsevier Oceanography Series.

Chatzigiannakou M.A., Dolguntseva I. and Leijon M., 2017, Offshore Deployments of Wave Energy Converters by Seabased Industry AB, Journal of Marine Science and Engineering 2017, 5(2), 15; doi:10.3390/jmse5020015

Christou M., Swan C., Gudmestad O.T., 2008, ”The interaction of surface water waves with submerged breakwaters”, Coastal Engineering 55, pp. 945–958

Cleveland C.J., 2014, Handbook of Energy. In C. J. Cleveland & C. Morris, eds. Handbook of Energy. MA, USA: Elsevier Science, pp. 323–332

Coastal Response Research Center (CRRC), 2010, Technical Readiness of Ocean Thermal Energy Conversion (OTEC), University of New Hampshire, Durham, NH, 27 pp and appendices.

Cornett A.M., 2008, A Global Wave Energy Resource Assessment. Proceedings of ISOPE 8, p.9.

Curran R., Stewart T. P, and Whittaker T. J. T., 1997, “Design Synthesis of Oscillating Water Column Wave Energy Converters: Performance Matching,” Proc. Inst. Mech. Eng., Part A, 211, pp. 489–505.

de Sousa Prado M.G., Gardner F., Damen M. and Polinder H., 2006, "Modelling and test results of the Archimedes wave swing", *Proceedings of the Institution of Mechanical Engineers, Part A: Journal of Power and Energy,* vol. 220, no. 8, pp. 855-868.

Dean R.G. and Dalrymple R.A., 1991, “Water wave mechanics for engineers and scientists”, Prentice Hall, Inc. Reprinted Singapore: World Scientific Publishing Co., pp. 170-178.

Deaton M.L. and Winebrake J.J., 2000, Greenhouse Gases and Global Warming. In: Dynamic Modeling of Environmental Systems. Modeling Dynamic Systems. Springer, New York, NY

Dhanasekaran T.S. and Govardhan M., 2005, Computational analysis of performance and flow investigation on Wells turbine for wave energy conversion, Renewable Energy, Vol. 30, pp. 2129-2147

Didier E., Paixao Conde J.M. and Teixeira, P.R.F., 2011, Numerical simulation of an oscillating water column wave energy convertor with and without damping, in: Proc., International Conference on Computational Methods in Marine Engineering

DiFresco L., Traverso A., 2014, “Energy conversion of orbital motions in gravitational waves: Simulation and test of the Seaspoon wave energy converter”, Energy Conversion and Management, Vol. 86, pp. 1164-1172.

Drew B., Plummer A.R., Sahinkaya M.N., 2016, A review of wave energy converter technology, Proceedings of the Institution of Mechanical Engineers, Part A: Journal of Power and Energy, Vol 223, Issue 8, pp. 887 – 902

European Union, 2009, Official Journal of the European Union, Directive 2009/28/EC of the European Parliament and of the Council of 23, L. 140/16, April 2009

European Union, 2016, Official Journal of the European Union, Proposal for a DIRECTIVE OF THE EUROPEAN PARLIAMENT AND OF THE COUNCIL on the promotion of the use of energy from renewable sources (recast), COM/2016/0767 final/2 - 2016/0382 (COD)

Falcão A., 2001, “The shoreline OWC wave power plant at the Azores”, Proceeding of the 4th European Wave and Tidal Energy Conference, Aalborg, Denmark, EWTEC

Falcão A.F.O. and Henriques J.C.C., 2016, "Oscillating-water-column wave energy converters and air turbines: A review", Renewable Energy, vol. 85, pp. 1391-1424

Falcão A.F.O., Cândido J.J., Justino P.A.P. and Henriques J.C.C., 2012, "Hydrodynamics of the IPS buoy wave energy converter including the effect of non-uniform acceleration tube cross section", *Renewable Energy,* vol. 41, pp. 105-114.

Filianoti P, Camporeale S.M., 2009, “In field measurement on a small scale OWC device”, Proceeding of the 8th European Wave and Tidal Energy Conference, Uppsala, Sweden, EWTEC

Genic S., Arandjelovic I., Kolendic P., Jaric M., Budimir N., Genic V., 2011, A review of explicit approximations of Colebrook’s equation, FME Transactions; Vol. 39: pp. 67–71

Goda Y. and Suzuki Y., 1976, “Estimation of incident and reflected waves in random waves experiments”, in Proc. Conference on Coastal Engineering, Honolulu, Hawaii, No. 15, p.828

Gomes R.P.F., Henriques J.C.C., Gato L.M.C. and Falcão A.F.O., 2015, Testing of a small-scale model of a heaving floating OWC in a wave channel and comparison with numerical results, Renewable Energy Offshore

Gunn K., Stock-Williams C., 2012, “Quantifying the global wave power resource”, Renewable Energy

Harlow F.H. and Amsden A.A., 1975, "Numerical calculation of multiphase fluid flow", *Journal of Computational Physics,* vol. 17, no. 1, pp. 19-52.

Harries D., Mchenry M., Jennings P. and Thomas C., 2006, "Hydro, tidal and wave energy in Australia", *International Journal of Environmental Studies,* vol. 63, no. 6, pp. 803-814.

Heath T., 2009, “The construction, commissioning and operation of the LIMPET wave energy collector”, Wavegen, retrived 2009-08-04

Holmes D.G. and Connell S.D., 1989, Solution of the 2D Navier-Stokes Equations on Unstructured Adaptive Grids. Presented at the AIAA 9th Computational Fluid Dynamics Conference, June 1989.

Huang L.H. and Chao H.I., 1992, ”Reflection and transmission of water wave by porous breakwater”, Journal of Water way, Port, Coastal and Ocean Engineering 118(5), 437–452

Hughes S.A., 1993, “Physical Models and Laboratory Techniques in Coastal Engineering”, Advanced Series on Ocean Engineering, Vol. 7. World Scientific, London, 568 pp.

IEA 2016, World Energy Outlook 2016, International Energy Agency, OECD Publication Service, OECD, Paris, www.IEA.org

Kamath A., Bish H. and Arntsen O.A., 2015, Numerical investigations of the hydrodynamics of an oscillating water column device, Ocean Engineering, Volume 102, 13 April 2015, Pages 40-50

Kempener R. and Neumann F., 2014, “Tidal Energy: Technology Brief” Abu Dhabi

Kempener R. and Neumann F., 2014, Ocean thermal energy conversion, Technology Brief, International Renewable Energy Agency (IRENA), www.irena.org

Kerr D., 2007, Marine Energy, Philosophical Transactions: Mathematical, Physical and Engineering Sciences, 365(1853, Energy for the Future), pp.pp. 971–992.

Kittitanasuan W., and Goda Y., 1994, “Analysis of nonlinear coefficients of reflection and transmission of waves propagating over a rectangular step”, Costal Engineering, pp.1241-1254

Kofoed J.P., Frigaard P., Friis-Madsen E. and Sørensen H.C., 2006, "Prototype testing of the wave energy converter wave dragon", *Renewable Energy,* vol. 31, no. 2, pp. 181-189.

Koo, W.C., Kim M.H., 2004, “Freely floating-body simulation by a 2D fully nonlinear wave tank”, Ocean Engineering, 31, pp. 2011-2046

Lewis A., Estefen S., Huckerby J., Musial W., Pontes T. and Torres-Martinez J., 2011, Ocean Energy. In IPCC Special Report on Renewable Energy Sources and Climate Change Mitigation [O. Edenhofer, R. Pichs-Madruga, Y. Sokona, K. Seyboth, P. Matschoss, S. Kadner, T. Zwickel, P. Eickemeier, G. Hansen, S. Schlömer, C. von Stechow (eds)], Cambridge University Press, Cambridge, United Kingdom and New York, NY, USA.

Lopez I., Pereiras B., Castro F. and Iglesias G., 2014, Optimisation of turbine-induced damping for an OWC wave energy converter using a RANS-VOF numerical model. Applied Energy 127, 105–114.

Lopez I., Andreu J., Ceballos S., Martinez De Alegria I. and Kortabarria I., 2013. Review of wave energy technologies and the necessary power-equipment. *Renewable and Sustainable Energy Reviews,* **27**, pp. 413-434.

Losada I.J., Silva R. and Losada M.A., 1996, “Interaction of non-breaking directional random waves with submerged breakwaters”, Coastal Engineering 28, pp. 249–266

Luo Y., Wang Z., Peng G., Xiao Y., Zhai L., Liu X. and Zhang Q., 2014, “Numerical simulation of a heave-only floating OWC (oscillating water column) device”, Energy, 76, pp. 799-806.

Masuda Y, Miyazaki Y, Yamada O, et al., 1981, Wave power generator assembly. US Patent No. 4405866.

McCallum P., Venugopal V., Forehand D. and Sykes R., 2014, "On the performance of an array of floating wave energy converters for different water depths", *Proceedings of the International Conference on Offshore Mechanics and Arctic Engineering - OMAE.*

Mofor L., Goldsmith J. and Jones F., 2014, OCEAN ENERGY: Technology Readiness, Patents, Deployment Status and Outlook, Paris

Morgan Y.D. and Testik F.Y., 2011, “Wave reflection by submerged vertical and semicircular breakwaters,” Ocean Engineering, vol. 39, p. 1269-1276

Nihous G.C., 2010, Mapping available Ocean Thermal Energy Conversion resources around the main Hawaiian Islands with state-of-the-art tools, Journal of Renewable and Sustainable Energy, 2(4)

Ning D., Wang R., Zou Q. and Teng B., 2016, An experimental investigation of hydrodynamics of a fixed OWC Wave Energy Converter, Applied Energy, Vol. 168, pp. 636-648

O'Dea J.F. and Newman J.N., 2007, “Numerical Studies of. Directional Wavemaker Performance,” Proc. 28th American. Towing Tank Conf., Ann Arbor, MI, 9-10 August

OES (Ocean Energy Systems), 2016, Annual Report Ocean Energy Systems 2015

P. Boccotti, 2012, Design of breakwater for conversion of wave energy into electrical energy, Ocean Engineering, Volume 51, 1 September 2012, Pages 106-118

Pelc R. and Fujita R.M., 2002, Renewable energy from the ocean, Marine Policy, 26, pp.471–479.

Raghunathan S., 1995, “The Wells Air Turbine for Wave Energy Conversion,” Prog. Aerosp. Sci., 31, pp. 335–386

Ram K.R., Ahmed M.R., Zullah M.A. and Lee Y., 2016, Experimental studies on the flow characteristics in an inclined bend free OWC device, Journal of Ocean Engineering and Science, Vol. 1, pp. 77-83

Reboli T., Roncallo F., Santamaria V.A., Canepa E., Traverso A., 2017, “The Seaspoon Wave Energy Converter: performance characterization of different blade geometries”, The Oceans’17 MTS/IEEE conference, Aberdeen, Scotland (UK).

Salter S.H., 1993, "Changing the 1981 spine-based ducks", *IEE Conference Publication*, pp. 121.

Shehata A.S., Saqr K.M., Shehadeh M., Xiao Q. and Day A.H., 2014, Entropy Generation due to Viscous Dissipation around a Wells Turbine Blade: A Preliminary Numerical Study, Energy Procedia, Vol. 50, pp. 808-816

Stamos D.G., Hajj M.R. and Telionis D.P., 2002, “Performance of the semi-cylindrical and rectangular submerged breakwaters”, Ocean Engineering 30, 813–828

Subramaniam S., 2013, "Lagrangian-Eulerian methods for multiphase flows", *Progress in Energy and Combustion Science,* vol. 39, no. 2-3, pp. 215-245.

Takahashi S., Nakada H., Ohneda H. and Shikamori M., 1992, *Wave power conversion by a prototype wave power extracting caisson in Sakata port*; 23th *ICCE*, Venice, pp.3440-3453

Tjugen K. J., 1993, “TAPCHAN Ocean Energy Project”, proceedings of European Wave Energy Symposium, Edinburgh

Torresi M., Camporeale S. M., Pascazio G. and Fortunato B., 2004, “Fluid Dynamic Analysis of a Low Solidity Wells Turbine”, 59° Congresso ATI, Genova, Italy

Torresi M., Camporeale S.M. and Pascazio G., 2007, “Experimental and numerical investigation of the performance of a Wells turbine prototype”, proceeding of the 7th European Wave and Tidal Energy Conference, Porto, Portugal, EWTEC

Torresi M., Camporeale S.M. and Pascazio G., 2007, *Performance of a small prototype of a high solidity Wells turbine*, Proceedings of the 7th European Conference of Turbomachinery: Fluid Dynamics and Thermodynamics, ETC 2007, code 111031, Athens, Greece, 5-9 March 2007

Torresi M., Camporeale S.M. and Pascazio G., 2009, *Detailed CFD analysis of the steady flow in Wells turbine under incipient and deep stall conditions*, Journal of Fluid Engineering, vol. 131, issue 7, Jun. 2009

Torresi M., Camporeale S.M., Strippoli P.D. and Pascazio G., 2008, Accurate Numerical Simulation of a High Solidity Wells Turbine, Renewable Energy, Vol. 33, pp. 735–747

Twu S.W. and Chieu C.C., 2000, “A highly wave dissipation offshore breakwater”, Ocean Engineering 27, 315–330

Uihlein A. and Magagna D., 2016, Wave and tidal current energy: A review of the current state of research beyond technology, Renewable and Sustainable Energy Reviews, Volume 58, 2016, Pages 1070-1081, ISSN 1364-0321

United Nations, 2016, *Paris Agreement*. Paris: United Nations, pp.1-27.

Usachev I.N., 2008, The outlook for world tidal power development. International Journal on Hydropower and Dams, 15(5), pp.100–105.

Van der Meer, Jentsje W., Briganti R., Zanuttigh B., 2005, “Wave transmission and reflection at low-crested structures: design formulae, oblique wave attack,and spectral change”, Coastal Engineering 52, 915–929

Whittaker T,. and Folley M., 2012, "Nearshore oscillating wave surge converters and the development of Oyster", *Philosophical Transactions of the Royal Society A: Mathematical, Physical and Engineering Sciences,* vol. 370, no. 1959, pp. 345-364.

Whittaker T. and Folley M., 2001, Nearshore oscillating wave surge converters and the development of Oyster, Philosofical transaction of the royal society, Published 19 December 2011, DOI: 10.1098/rsta.2011.0152

Whittaker T.J.T., Beattie W., Raghunathan S., Thompson A., Stewar, T. and Curran R., 1997, "The Islay wave power project: An engineering perspective", *Proceedings of the Institution of Civil Engineers: Water and Maritime Engineering,* vol. 124, no. 3, pp. 189-201.

World Energy Council, 2016, Marine Energy (World Energy Resources 2016), DOI: 10.13140/RG.2.2.24836.73607, October 2016

Youngs D.L., 1982, Time-Dependent Multi-Material Flow with Large Fluid Distortion. In K.W. Morton and M.J. Baines, editors, *Numerical Methods for Fluid Dynamics*. Academic Press